

DESIGN AND IMPLEMENTATION OF AN EXTENSIVE TEST FACILITY
FOR THERMOELECTRIC MATERIALS AND DEVICES

Design and Implementation of an Extensive Test Facility for
Thermoelectric Materials and Devices

By

MICHAEL CINO, B.Eng. & Society

A Thesis

Submitted to the School of Graduate Studies
in Partial Fulfillment of the Requirements for the Degree
Master of Applied Science

McMaster University
© Copyright Michael Cino, September 2014

MASTERS OF APPLIED SCIENCE (2014)

McMaster University

(Engineering Physics)

Hamilton, Ontario

TITLE: Design and Implementation of an
Extensive Test Facility for
Thermoelectric Materials and Devices

AUTHOR: Michael Cino, B.Eng. & Society
(McMaster University)

SUPERVISOR: Dr. J.S. Preston

NUMBER OF PAGES: xxiii, 136

Abstract

A test system was commissioned to characterize commercial thermoelectric modules to be used in the Pizza Oven Waste Energy Recovery (POWER) system for Pizza Pizza restaurants. The objective of this testing was to obtain and classify the thermoelectric material parameters of the Bi_2Te_3 within commercial thermoelectric generator (TEG) modules. These parameters consisted of the Seebeck coefficient, the thermal conductivity and the electrical resistivity. Together they provide the normalized figure of merit for the thermoelectric material which is a performance indicator for energy efficiency at a given operating temperature. From this research, a two phase methodology was developed that was able to extract the desired values from these modules. Material quality and device composition was first assessed with tools such as SEM and EDS. During this phase, dimensional and elemental data was gathered and a finite element model was constructed to ensure the validity of the primary selected test method for this research which was the Harman technique. The results obtained with this method were all three of the aforementioned thermoelectric parameters as well as a direct measurement of the figure of merit. Thermal and electrical losses for the TEG1B-12610-5.1 module were characterized from room temperature to 200°C using this process. It was determined that the thermal losses were more dominant and could be approximated using a function of T^4 to within 1% of their calculated values. This process can be applied to any model of TEG to forecast these losses. To assist with future research, a secondary test method known as the Parallel Thermal Conductance technique was researched and a proposed model of it was designed for use in temperatures up to 300°C. Due to the relatively short test time of the

Harman Technique, it was also used to effectively bin incoming groups of TEGs used in the POWER system so that they could be placed strategically in different areas of heat flow based on their measured performance. An increase of 13.2% was observed in the electrical output of the system after the binning had occurred.

Acknowledgements

I would first and foremost like to express the utmost gratitude to my supervisor and mentor, Dr. John Preston, for giving me such a tremendous opportunity to work with him on this project. His guidance, wisdom, and understanding were all vital to the successful completion of this thesis. I would like to express equal gratitude to Dr. Jim Cotton, whose experience and leadership gave me the tools to become a confident independent researcher.

I also wish to thank the following individuals for their contributions:

- Jim Garrett, for his continuous input and collaboration in the final design of my test system. He is an invaluable resource and I would not have made it to this point without him.
- Hossam, Donal, Corbin, Raf, Jeff, Yakoob and the members of the Mech Eng team who provided me with a fresh perspective in problem-solving and some great camaraderie.
- Gabe, Kris, Steven, Tahereh, Vicky, and the members of the Preston group for their engaging discussions and helpful ideas.
- My friends, Daniel, Rachael, Harrison, Paul, Anthony, Jeff, and everyone who helped stimulate the other side of my brain when I needed it most.
- The lady in my life, Sara, for having tremendous patience for putting up with my late nights in the lab and the long hours it took to complete this thesis.
- My entire family, especially my sister, my Aunt Em, Aunt Carm, and Uncle Mike, for being positive role models to look up to, and also my grandparents for coming to this country and proving that it does not only take an engineer to make something from nothing.

Finally, I would like to thank my mom whose unconditional love has been the cornerstone of my success. She has nurtured my need to never stop learning ever since I was a young boy, and taught me the importance of kindness and generosity. This is for you, mom.

Contents

Abstract	iii
Acknowledgements	v
List of Tables	ix
List of Figures	x
Nomenclature	xv
Relevant Physical Constants	xxiii
1. Introduction	1
1.1 Scope of Work	1
2. Background	2
2.1 Thermoelectric Phenomena	2
2.1.1 Seebeck Effect	2
2.1.2 Peltier Effect	4
2.1.3 Thomson Effect	5
2.1.4 Kelvin Relationships	5
2.2 Thermoelectric Materials	6
2.2.1 Semiconductor Theory	6
2.2.2 Ohmic Junctions	17
2.2.3 Thermoelectric Transport Coefficients	20
2.2.4 Figure of Merit	20
2.3 Thermoelectric Modules	23
2.3.1 Modes of Operation	23
2.3.2 Power Considerations	23
2.3.3 Areas of Improvement	26
3. Test System Design	28
3.1 Selected Test Methods	28

3.1.1 Harman Technique	28
3.1.2 Parallel Thermal Conductance Technique	34
3.3 Software Overview	36
3.3.1 Functional Requirements	36
3.3.2 Description of Code	37
3.4 Hardware Overview	38
3.4.1 Electronics	38
3.4.2 Physical Interface	47
3.5 Loss Minimization	58
3.5.1 Harman Technique	58
3.5.2 Parallel Thermal Conductance	68
4. ANSYS Modelling	70
4.1 Harman Technique Model	70
4.2 Parallel Thermal Conductance Model	78
5. Test Results	82
5.1 Harman Technique	82
5.1.1 Module Testing	82
5.1.2 Comparison to Model	84
5.2 PTC Simulation Results	86
6. Case Study: Binning Technique for Waste Heat Recovery System	88
6.1 Description of Technique	88
6.2 Sample Results	92
6.3 System Efficiency Improvement	93
7. Conclusion	94
7.1 Future Work	96
8. References	98
APPENDIX A: Measurement Uncertainty	102
<i>Voltage Uncertainty</i>	102
<i>Current Uncertainty</i>	105

<i>Temperature Uncertainty</i>	105
<i>Dimensional Uncertainty</i>	109
<i>Radiative Loss Uncertainty</i>	110
<i>Thermoelectric Property Uncertainty</i>	112
APPENDIX B: Harman Technique LabView Code	116
APPENDIX C: PTC Technique LabView Code	123
APPENDIX D: Harman Technique PCB Layout	125
APPENDIX E: Heater Material Data	126
APPENDIX F: Heater Boundary Conditions for ANSYS Simulation	127
APPENDIX G: Thermal Loss Quantities	128
APPENDIX H: Sample View Factor Calculations	129
APPENDIX I: TEG Unit Cell Dimensions	135
APPENDIX J: TEG Unit Cell Material Data	136

List of Tables

Table 1: Dimensions of heater components and total heater wire length.	53
---	----

List of Figures

Figure 1: Illustration of the Seebeck effect; a voltage is generated between terminals 3 and 4 based on the temperature difference at junctions 1 and 2.....	2
Figure 2: A thermocouple composed of (top) a material with a negative Seebeck coefficient and (bottom) one with a positive Seebeck coefficient. The two legs are joined electrically in series with the help of a third conductor material and thermally in parallel. A voltage is generated on the right [4].	3
Figure 3: Illustration of the Peltier effect. A voltage supply is used to drive a current through terminals 3 and 4 to create a temperature difference at junctions 1 and 2.	4
Figure 4: Electron energy levels versus interatomic separation in a crystal of $N=10$ atoms, as recreated from [5].	7
Figure 5: (a) Formation of energy bands in a crystal after the distribution of atoms reaches a stable configuration in (b). (b) Electron energy levels versus interatomic separation for a bulk crystalline material. This diagram is also adapted from [5].	8
Figure 6: Simplified band diagrams for an insulator, intrinsic semiconductor and a metal at 0K. Redrawn and adapted from [6].....	9
Figure 7: The Fermi-Dirac Distribution for a material at three different temperatures, as recreated from [6].....	11
Figure 8: Simplified band diagrams of an intrinsic, n-type and p-type semiconductor at room temperature.	13
Figure 9: Fermi-Dirac distribution of Intrinsic, n-type and p-type semiconductors at temperature $T>0K$ as recreated from [6].	16
Figure 10: Ohmic junction formation (a) before bonding (b) at the point of bonding p-metal-n (c) after equilibrium has been reached.....	18
Figure 11: (Top) Thermocouple under the influence of the Seebeck effect and (Bottom) corresponding band diagram.....	19

Figure 12: Normalized ZT as a function of temperature for different thermoelectric materials, recreated from [11]. TAGS are a group of alloyed materials that contain a combination of Te, Ag, Ge and Sb. Examples include AgSbTe_2 as well as GeTe [12].....	21
Figure 13: Dependence of electrical conductivity, Seebeck coefficient, power factor, and thermal conductivity on concentration of free carriers as recreated from [3].	22
Figure 14: Cross-section of a thermoelectric module.	23
Figure 15: Open-Circuit TEG schematic.	24
Figure 16: TEG output with a load resistor.....	24
Figure 17: Voltage outputs of a thermoelectric device under the influence of the Peltier effect.	29
Figure 18: Illustration of the applied input and measured output during a Harman test.	31
Figure 19: PTC sample holder (a) without sample and (b) with sample attached.	34
Figure 20: Harman Technique Functional Block Diagram	37
Figure 21: PTC Functional Block Diagram	38
Figure 22: RTD Constant Current Drive Circuit.	41
Figure 23: Illustration of a Type T Differential Thermocouple.	43
Figure 24: H-bridge subsection of auxiliary circuit.....	44
Figure 25: Schematic of Auxiliary Circuit. (A) H-bridge sub-circuit. (B) Temperature sensor interface. (C) Circuit power. (D) DAQ interface. (E) Power supply interface.	45
Figure 26: Cross-sectional view of the Harman Technique test system with sample TEG and temperature sensors included.	48

Figure 27: Isometric view of the Harman Technique test system without sample TEG and temperature sensors.....	48
Figure 28: Cross-sectional view of the PTC Technique test system.....	49
Figure 29: Isometric view of the PTC test system.	49
Figure 30: (a) Isometric view and (b) exploded view of heater constructed for use in the Harman test system.	50
Figure 31: Heater wire configuration with emphasis on straight components.	51
Figure 32: Sample arc length segment of heater wire.	52
Figure 33: Heater surface temperature (a) without copper surface and (b) with copper surface.....	55
Figure 34: Heater surface heat flux (a) without copper surface and (b) with copper surface.....	56
Figure 35: Top surface heat distribution of heater with and without copper plate.	58
Figure 36: Example of the current applied during the Harman technique in (a) forward bias and (b) reverse bias. The associated temperatures that form at the outer surfaces are a result of the direction of the current.	60
Figure 37: Calculated values for C_L vs. Heater Temperature.....	64
Figure 38: V_C vs. average temperature.	67
Figure 39: R_C vs. average temperature.....	67
Figure 40: SEM image of a TEG thermocouple. Compositional information determined by EDS.	71
Figure 41: Recreation of dimensional measurement process using <i>ImageJ</i> . Each yellow line is manually drawn by the user and its length is compared to the scale given in the image. Sample photographs are of a (a) p-type leg and (b) the Al contact layer.	72

Figure 42: Length, width and cross-sectional area designations for (a) p-type element and (b) n-type element.....	73
Figure 43: SolidWorks assembly of TEG Unit Cell with material designations for each layer.....	74
Figure 44: Theoretical depiction of TEG module comprised of unit cells.	75
Figure 45: (a) Forward bias electrical and thermal boundary conditions. (b) Thermal response to applied current.	76
Figure 46: (a) Reverse bias electrical and thermal boundary conditions. (b) Thermal response to applied current.	77
Figure 47: SolidWorks assembly of PTC system with sample attached.	79
Figure 48: (a) Heater input for PTC holder simulation. (b) Generated temperature difference across the post from heater to heat sink.....	80
Figure 49: (a) Heater input for PTC holder + sample simulation. (b) Generated temperature difference across the post and the sample.....	81
Figure 50: Seebeck coefficient as a function of temperature.....	82
Figure 51: Electrical resistivity as a function of temperature.	82
Figure 52: Measured thermal conductivity and estimated thermal conductivity using C_L as a function of temperature.....	83
Figure 53: Measured ZT and Estimated ZT using C_L as a function of temperature.	83
Figure 54: The effects of ignoring thermal and electrical losses in ZT measurements.....	84
Figure 55: Thermal conductivity vs. heater temperature. The results simulated from the PTC technique are compared with the actual values obtained from the Harman Technique.....	86
Figure 56: Comparison of (a) ZTs and (b) maximum power output measured for a row of TEGs before and after binning.	92

Figure 57: Pre-binning and Post-binning I-V curves for the total output of 40 TEGs.....	93
---	----

Nomenclature

Symbol/ Acronym	Description	Applicable Units
$\dot{Q}_{Al_2O_3B}$	Radiative heat loss from bottom Al_2O_3 contact layer	[W]
$\dot{Q}_{Al_2O_3T}$	Radiative heat loss from top Al_2O_3 contact layer	[W]
\dot{Q}_{Al}	Radiative heat loss from Al contact layer	[W]
\dot{Q}_C	Rate of heat flow into cold side	[W]
\dot{Q}_{Cu}	Radiative heat loss from Cu contact layer	[W]
\dot{Q}_H	Rate of heat flow into hot side	[W]
\dot{Q}_{NiB}	Radiative heat loss from bottom Ni contact layers	[W]
\dot{Q}_{NiT}	Radiative heat loss from top Ni contact layers	[W]
\dot{Q}_{Rad}	Sum of radiative heat losses	[W]
\dot{Q}_{Sn}	Radiative heat loss from Sn contact layer	[W]
\dot{Q}_{Zn}	Radiative heat loss from Zn contact layer	[W]
\dot{Q}_{conv}	Convective heat	[W]
\dot{Q}_{in}	Input power to heater for PTC technique	[W]
\dot{Q}_n	Radiative heat loss from n-type material	[W]

\dot{Q}_p	Radiative heat loss from p-type material	[W]
\dot{Q}_{rad}	Radiative heat	[W]
\dot{Q}_{Π}	Heat generated by the Peltier effect	[W]
\dot{Q}_κ	Heat conducted through sample	[W]
A_{sCu}	Exposed surface area of Cu in a TEG	[m ²]
J_{Qx}	Heat current density (one-dimensional)	[W/m ²]
J_x	Current density (one-dimensional)	[A/m ²]
\dot{Q}	Rate of heat flow	[W]
T_{aCu}	Local average surface temperature of Cu in a TEG	[K], [°C]
m_e^*	Effective mass of electrons	[kg]
m_h^*	Effective mass of holes	[kg]
A, A_s, A_p, A_n	Cross-sectional area of sample under test	[m ²]
C_i	i^{th} order coefficient of thermocouple polynomial	[K/V], [°C/V]
C_L	Heat loss correction factor during a Harman test	
D_a	Sum of temperature differences observed during a Harman test	[K], [°C]
d_{gap}	Distance between grooves in heater substrate	[cm]
d_{groove}	Thickness of groove in heater substrate	[cm]

DTC	<i>Differential Thermocouple</i>	
d_{wire}	<i>Diameter of heater wire</i>	<i>[cm]</i>
E	<i>Energy</i>	<i>[J], [eV]</i>
E_C	<i>Conduction band edge</i>	<i>[J], [eV]</i>
E_F	<i>Fermi level</i>	<i>[J], [eV]</i>
E_{Fi}	<i>Intrinsic Fermi level</i>	<i>[J], [eV]</i>
E_{Fn}	<i>n-type Fermi level</i>	<i>[J], [eV]</i>
E_{Fp}	<i>p-type Fermi level</i>	<i>[J], [eV]</i>
E_g	<i>Semiconductor band gap</i>	<i>[J], [eV]</i>
E_V	<i>Valence band edge</i>	<i>[J], [eV]</i>
h	<i>Convective heat transfer coefficient</i>	<i>$[W \cdot m^{-2} \cdot K^{-1}]$</i>
I	<i>Current</i>	<i>[A]</i>
I_{RTD}	<i>Test current through RTD</i>	<i>[A]</i>
K_H	<i>Thermal conductance of sample holder during PTC technique</i>	<i>[W/K]</i>
K_{H+S}	<i>Combined thermal conductance of the holder and sample during the PTC technique</i>	<i>[W/K]</i>
K_S	<i>Thermal conductance of sample during PTC technique</i>	<i>[W/K]</i>
L	<i>Sample length coincident with current flow</i>	<i>[m]</i>

L_{arc}	Arc length segment of heater wire	[cm]
$L_{contact}$	Contact length segment of heater wire	[cm]
$L_{straight}$	Straight length segment of heater wire	[cm]
L_{total}	Total length of heater wire used in a heater	[cm]
n	Concentration of electrons in a semiconductor	[cm] ³
N	Number of thermocouples or elements in a TEG module	
N_{arc}	Number of wire arcs in a heater	
$N_{grooves}$	Number of grooves within heater substrate	
n_i	Intrinsic carrier concentration	[cm] ³
p	Concentration of holes in a semiconductor	[cm] ³
P	Power	[W]
PCB	Printed circuit board	
P_{max}	Maximum power	[W]
PTC	Parallel Thermal Conductance	
R_c	TEG electrical contact resistance	[Ω]
R_{Load}	Load resistance	[Ω]
R_T	Temperature dependent resistance of RTD	[Ω]

R_T	Resistance at temperature T	$[\Omega]$
RTD	Resistive Temperature Device	
R_{TEG}	Resistance of TEG module	$[\Omega]$
T	Temperature	$[K], [^{\circ}C]$
T_0	Reference temperature	$[K], [^{\circ}C]$
T_A	Total average temperature encountered during a Harman test	$[K], [^{\circ}C]$
T_a	Average temperature of a sample in forward bias during a Harman test	$[K], [^{\circ}C]$
T_a'	Average temperature of a sample in reverse bias during a Harman test	$[K], [^{\circ}C]$
T_{amb}	Ambient temperature	$[K], [^{\circ}C]$
T_{ave}	Average temperature between hot side and cold side of thermoelectric device	$[K], [^{\circ}C]$
T_c	Cold side temperature	$[K], [^{\circ}C]$
T_c	Cold side temperature measured on the forward bias polarization during a Harman test	$[K], [^{\circ}C]$
T_c'	Cold side temperature measured on the reverse bias polarization during a Harman test	$[K], [^{\circ}C]$
TEC	Thermoelectric cooler	
TEG	Thermoelectric Generator	
T_H	Hot side temperature measured on the forward bias polarization during a	$[K], [^{\circ}C]$

Harman test

T_H'	Hot side temperature measured on the reverse bias polarization during a Harman test	[K], [°C]
T_s	Temperature of outer surface	[K], [°C]
V	Voltage	[V]
V_+, V_-	Positive and negative output voltage measurement terminals on RTD	[V]
V_c	TEG contact voltage	[V]
V_b V_{i+}, V_{i-}	Steady-state thermoelectric voltage component of Harman technique	[V]
V_{ia}	Average resistive voltage between V_{i+} and V_{i-}	[V]
V_o V_{o+}, V_{o-}	Seebeck voltage component during the Harman technique	[V]
V_{oa}	Average resistive voltage between V_{o+} and V_{o-}	[V]
V_{oc}	Open-circuit voltage	[V]
V_{out}	Output voltage	[V]
V_r V_{r+}, V_{r-}	Resistive voltage component during the Harman technique	[V]
V_{ra}	Average resistive voltage between V_{r+} and V_{r-}	[V]
W	Heater wire arc diameter	[cm]
ZT	Normalized figure of merit	

α	Seebeck coefficient	[V/K],[V/°C]
α_{couple}	Seebeck coefficient of thermocouple consisting of positive and negative Seebeck materials	[V/K], [V/°C]
β	Thomson coefficient	[V/K], [V/°C]
γ	Offset coefficient used for the approximation of C_L	
ΔT	Temperature difference between hot side and cold side; $T_H - T_c$	[K], [°C]
ΔT_1	Temperature difference measured across the PTC holder	[K], [°C]
ΔT_2	Temperature difference measured across the PTC holder + sample	[K], [°C]
ε	Emissivity	
η	TEG power efficiency	
κ	Thermal conductivity	[W·m ⁻¹ ·K ¹]
κ_e	Electronic component of thermal conductivity	[W·m ⁻¹ ·K ¹]
κ_L	Lattice component of thermal conductivity	[W·m ⁻¹ ·K ¹]
κ_S	Thermal conductivity of sample during the PTC technique	[W·m ⁻¹ ·K ¹]
λ	Temperature coefficient of resistivity	
μ	Proportional coefficient used for the approximation of C_L	[K] ⁴

Π	<i>Peltier coefficient</i>	$[V]$
ρ	<i>Electrical resistivity</i>	$[\Omega \cdot m]$
ρ_0	<i>Electrical resistivity at reference temperature T_0</i>	$[\Omega \cdot m]$
ρ_T	<i>Electrical resistivity at temperature T</i>	$[\Omega \cdot m]$
σ	<i>Electrical conductivity</i>	$[\Omega \cdot m]^{-1}$

Relevant Physical Constants

Symbol	Name	Value
σ_B	Stefan-Boltzmann Constant	$5.6704 \cdot 10^{-8} \text{ [W} \cdot \text{m}^{-2} \cdot \text{K}^{-4}]$
k_B	Boltzmann Constant	$1.3806 \cdot 10^{-23} \text{ [m}^2 \cdot \text{kg} \cdot \text{s}^{-2} \cdot \text{K}^{-1}]$

1. Introduction

In recent years a specific emphasis has been put towards the pursuit of renewable energy systems. It has become an issue of paramount importance that the scientific community investigate alternative methods of energy production that do not result in excessive levels of pollution brought about by the burning fossil fuels. The current research in renewable energy sources extends over a broad range of mechanisms including solar, wind, and nuclear power generation. However one such technology stands out above the rest with its ability to not only generate new power, but also to recover energy from waste heat which composes about 57% of the total energy production in the United States alone [1]. This technology is of course, thermoelectrics.

1.1 Scope of Work

The material investigated in this project is bismuth telluride (Bi_2Te_3). Its thermoelectric properties are optimal from 25°C to 250°C. Materials characterization has been approached in two phases: (1) Materials Quality Testing and, (2) Figure of Merit Factor Determination.

Phase 1 included subjecting various Bi_2Te_3 samples from different sources to X-Ray Diffraction (XRD) and Scanning Electron Microscopy (SEM) testing. The sources included a solid ingot, a powder, and the individual TEG p and n elements found in commercial TEGs. This testing confirmed the degree of crystallinity, crystal structure, and elemental composition of the p-type and n-type samples. All of this information provided a qualitative foundation that aided to model and explain the thermoelectric performance of these materials in Phase 2.

Phase 2 testing involved building a test facility that would be able to characterize both thermoelectric modules and materials over the previously mentioned temperature range. The facility was also used to implement a binning technique to organize and rank the output performance of a batch of commercial thermoelectric generators (TEGs) to be used in a waste heat recovery system. The characteristics of interest determined by the test facility were the normalized thermoelectric figure of merit, ZT , and its associated parameters. These consist of the Seebeck coefficient, electrical resistivity, and thermal conductivity, all plotted versus operating temperature. The test methods explored in this phase of research were the Harman Technique and the Parallel Thermal Conductance (PTC) Technique. The Harman test facility was designed and tested on commercially available TEG modules and the PTC apparatus was modelled and characterized to completion however no experimental data was taken with it.

2. Background

2.1 Thermoelectric Phenomena

2.1.1 Seebeck Effect

A thermocouple is composed of two dissimilar metals joined together at two junctions. When these junctions are placed across a temperature difference, they generate a thermal EMF as observed in Figure 1. This is the Seebeck effect, discovered by Thomas Seebeck in 1821, and is the basis for thermoelectric power generation as well as for thermocouple temperature sensors [2].

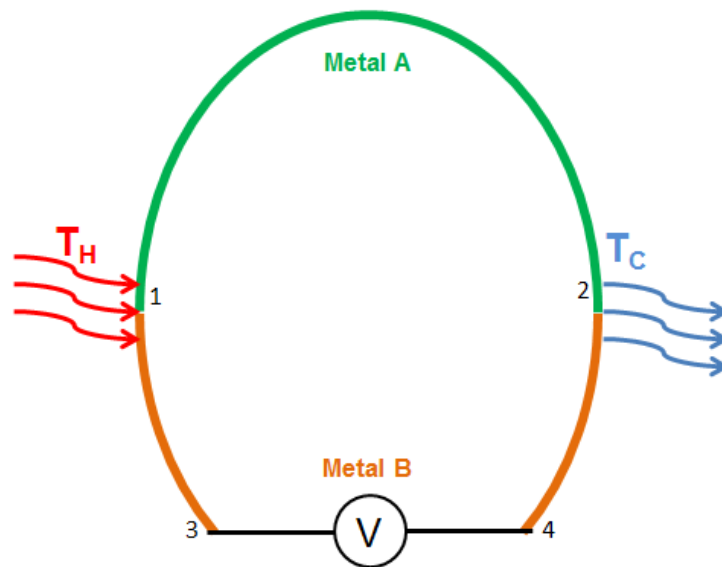


Figure 1: Illustration of the Seebeck effect; a voltage is generated between terminals 3 and 4 based on the temperature difference at junctions 1 and 2.

In the above diagram, junctions 1 and 2 are heated and cooled, respectively, and a voltage difference is generated across terminals 3 and 4. In a given electrically conductive material, the magnitude of the voltage created is linearly proportional to the applied temperature difference. This

coefficient of proportionality varies from material to material and is called the Seebeck coefficient, α , as observed in equation (2.1) [3].

$$\alpha = \frac{V}{\Delta T} \quad (2.1)$$

Materials which contain a negative α facilitate electron flow from the hot side to the cold side. Conversely, a positive α implies that electrons move from cold to hot. Therefore when one of each of these materials are combined in a thermocouple and applied a ΔT , then current flow is in one direction and a potential can be measured at both terminals. This is shown in Figure 2.

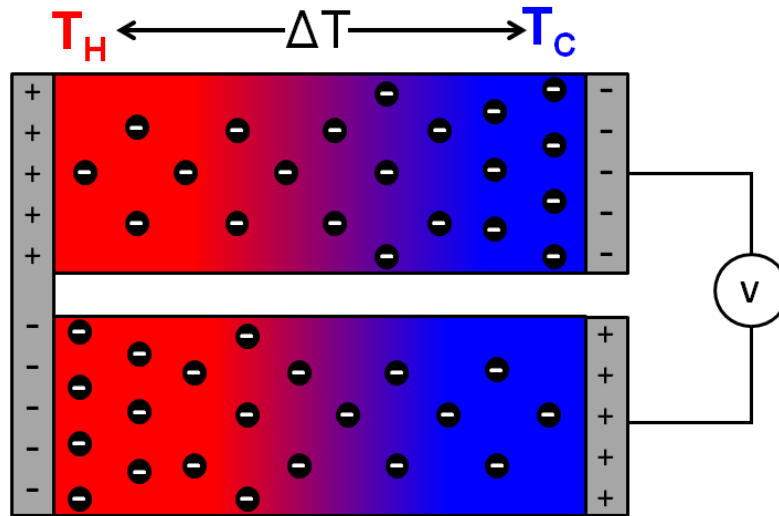


Figure 2: A thermocouple composed of (top) a material with a negative Seebeck coefficient and (bottom) one with a positive Seebeck coefficient. The two legs are joined electrically in series with the help of a third conductor material and thermally in parallel. A voltage is generated on the right [4].

For the combination of metals shown in Figure 1, the total Seebeck coefficient for the couple is equal to the difference between those of the constituent materials [3]. This is represented in the equation below.

$$\alpha_{ab} = \alpha_a - \alpha_b \quad (2.2)$$

2.1.2 Peltier Effect

The Peltier effect is simply the reverse of the Seebeck effect. Figure 3 depicts the familiar two-metal system, only with an external current supply attached across terminals 3 and 4. This allows the circulation of a current through the thermocouple, with the absorption of thermal energy at junction 1 and the release of thermal energy at junction 2.

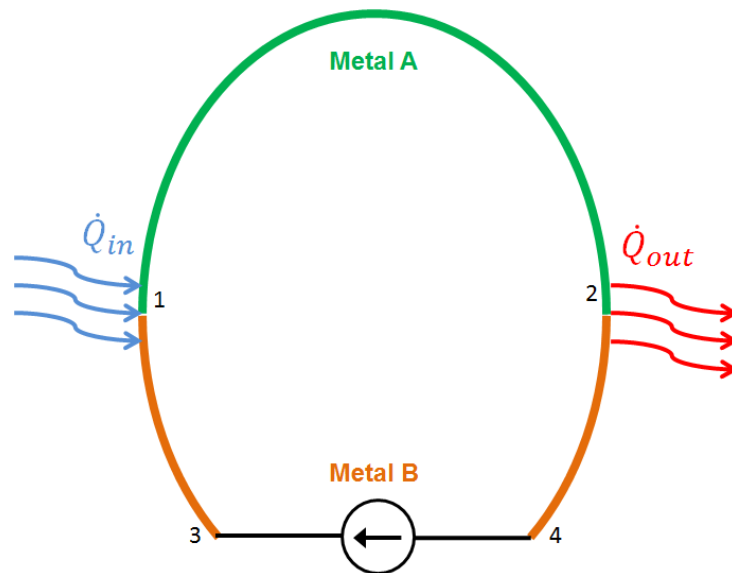


Figure 3: Illustration of the Peltier effect. A voltage supply is used to drive a current through terminals 3 and 4 to create a temperature difference at junctions 1 and 2.

The rate of cooling is given by \dot{Q}_{in} , whereas the rate of heating is given by \dot{Q}_{out} , where this amount is known as the Peltier heat. These two quantities are not exactly equivalent due to an additional heat loss from Joule heating. The magnitude of this rate is proportional to the current passed through the couple, and again this ratio is material specific. This

ratio is the couple's Peltier coefficient, Π_{ab} , and is defined in equation (2.3) [3].

$$\Pi_{ab} = \frac{\dot{Q}_{out}}{I} \quad (2.3)$$

2.1.3 Thomson Effect

The Thomson effect is observable in the following manner. A conductor that is subjected to a temperature difference and is applied a current will produce a reversible heat flow that is dependent on the direction of that current. The amount of heat generated is dependent on the Thomson coefficient, β , and like the previously mentioned phenomena, is both material and temperature dependent. The heat flow generated by the Thomson effect is defined by equation (2.4).

$$\dot{Q} = \beta I \Delta T \quad (2.4)$$

The Thomson effect is mainly considered in applications where a large temperature gradient is applied. Within this gradient, the introduction of Thomson heat flow can affect the localized thermoelectric material properties of a device at discretized temperature ranges. Therefore knowledge of the Thomson coefficient is mainly useful when testing a device in-situ during a system installation. It can be used to determine the two previously mentioned coefficients with the help of the Kelvin relationships, and vice versa [3].

2.1.4 Kelvin Relationships

The Seebeck, Peltier and Thomson coefficients are related by the Kelvin relationships given below. These are valid for all thermoelectric

materials [3]. Specifically, they reference a junction of two thermoelectric materials labelled a and b .

$$\alpha_{ab} = \frac{\Pi_{ab}}{T} \quad (2.5)$$

$$\frac{d\alpha_{ab}}{dT} = \frac{\beta_a - \beta_b}{T} \quad (2.6)$$

2.2 Thermoelectric Materials

2.2.1 Semiconductor Theory

The electrons orbiting an atom are confined spatially to atomic orbitals. The electron energy states occupy discrete levels. The location of these levels shift during the formation of a crystal where large numbers of identical atoms or molecules come together and the spacing between neighbouring atoms forces the orbitals to shift and redistribute themselves. An example for a crystal of 10 atoms is given in the following figure.

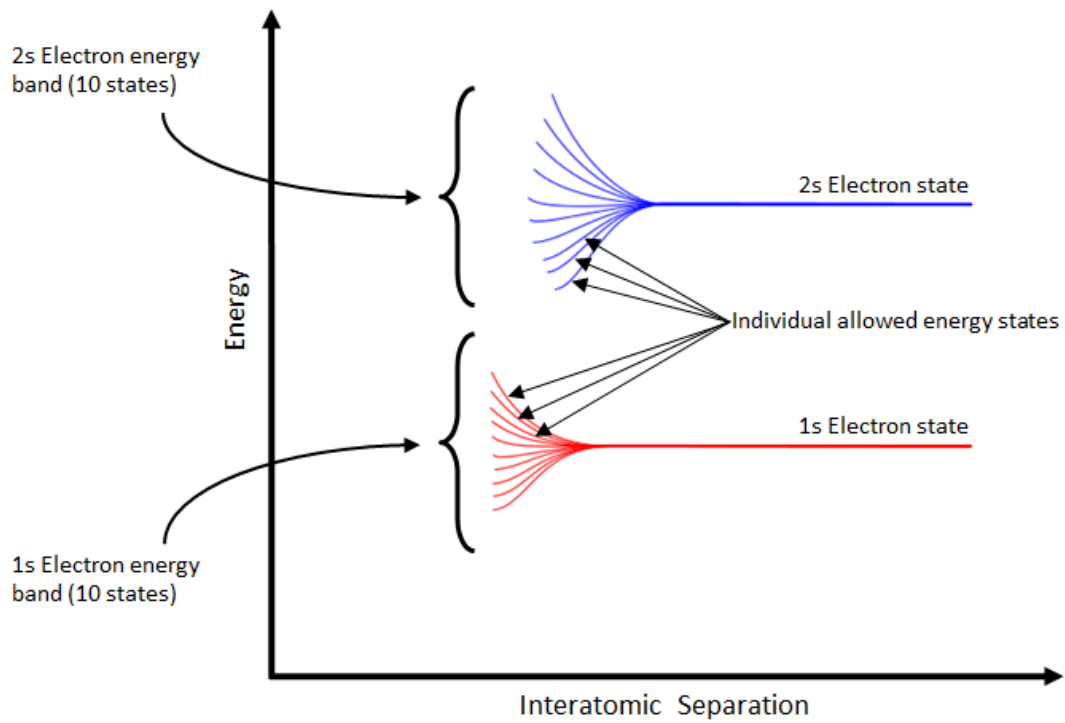


Figure 4: Electron energy levels versus interatomic separation in a crystal of $N=10$ atoms, as recreated from [5].

As more atoms are added to the crystal, they become increasingly confined causing the spread in their electron states to become more continuous and form energy bands. The locations and sizes of these bands define the degree of electrical conductivity of the material. This phenomenon is illustrated in Figure 5.

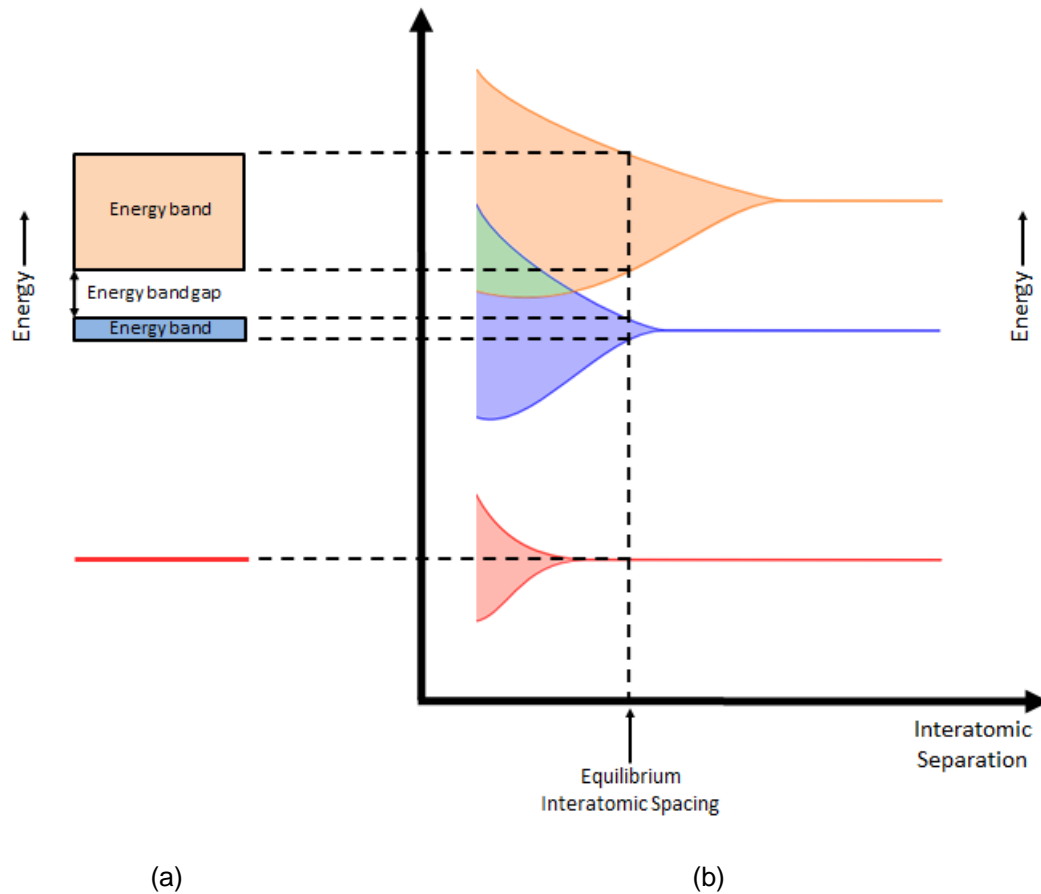


Figure 5: (a) Formation of energy bands in a crystal after the distribution of atoms reaches a stable configuration in (b). (b) Electron energy levels versus interatomic separation for a bulk crystalline material. This diagram is also adapted from [5].

There are three classes of electrical conductivity. These are metals, semiconductors and insulators. At the quantum mechanical level, each differs by the amount of energy required to move electrons from the valence band to the conduction band, and thus facilitate current flow. The three categories are represented pictorially in Figure 6.

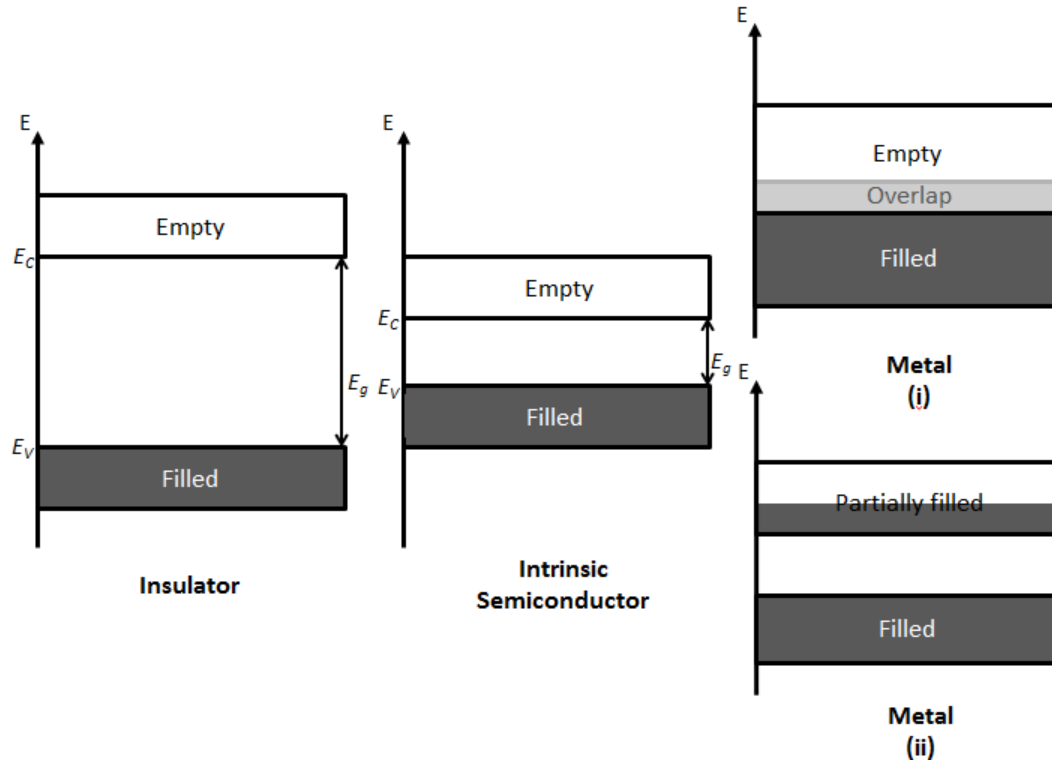


Figure 6: Simplified band diagrams for an insulator, intrinsic semiconductor and a metal at 0K. Redrawn and adapted from [6].

E_c is the conduction band edge and E_v is the valence band edge. The region between the bands denoted by E_g is called the band gap, where no energy states can exist [4].

$$E_g = E_c - E_v \quad (2.7)$$

An electron can be elevated to the conduction band by absorbing quantized energy that is equal to or greater than E_g . This energy can come in the form of photons or phonons. Insulators have the largest band gap and statistically their carriers seldom leave the valence band due to the large amount of energy required to do so. This makes them impractical for electrical conduction. However since the band gap is smaller in semiconductors, a nominal rise in ambient temperature can simply meet

the energy requirements to thermally excite carriers and promote them to the unoccupied states in the valence band. To gain a numerical perspective, a typical insulator such as diamond as band gap equal to 5 eV while silicon, a semiconductor, has a band gap of only 1.1 eV. Metals can occur in one of two different band structures depending on their orbital configuration. They do not have distinctly separate valence and conduction bands and therefore have no band gap. Metals can have overlapping empty and filled bands or a filled and partially filled band structure where carriers are able to move freely with minimal energy requirements.

The statistics of current flow are described by the Fermi-Dirac distribution which is given by equation (2.8).

$$f(E) = \frac{1}{1 + e^{\frac{E-E_F}{k_B T}}} \quad (2.8)$$

This function gives the probability of an electron occupying a state of energy E within a material at temperature T . The Fermi level, E_F , is of mathematical significance as it is a reference energy level that aids in the calculation of the electronic performance within a semiconductor. Evaluating equation (2.8) at $E = E_F$ for any temperature $T > 0$ K yields:

$$f(E_F) = \frac{1}{1 + e^{\frac{E_F-E_F}{k_B T}}} = \frac{1}{1 + e^0} = \frac{1}{2}$$

This implies that energy states at the Fermi level contain a 50% probability of electron occupancy. Considering again equation (2.8) at different fixed temperatures and evaluating for all values of $E > 0$, three plots of the Fermi-Dirac distribution function for a semiconductor are depicted in Figure 7, each at a different temperature.

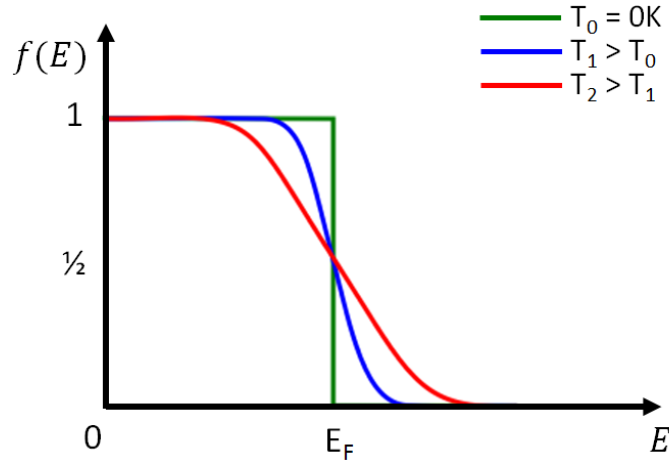


Figure 7: The Fermi-Dirac Distribution for a material at three different temperatures, as recreated from [6].

At $T = 0\text{K}$ the distribution resembles a step function situated at the Fermi level, indicated by the green curve above. This is explained by solving for $E < E_F$ and for $E > E_F$ respectively:

$$f(E < E_F) = \frac{1}{1 + e^{-\infty}} = \frac{1}{1 + 0} = 1$$

$$f(E > E_F) = \frac{1}{1 + e^{\infty}} = \frac{1}{1 + \infty} = 0$$

The electrons are in their lowest possible energy configuration with all energy states up to E_F being filled, while those above remain empty. As temperature increases, thermal energy is added to the system and a probability of occupancy for states above E_F begins to appear. Electrons now have sufficient energy to move into the conduction band and the shape of the distribution function changes, as depicted by the blue and red curves in Figure 7. The semiconductor band shown in Figure 6 is that of an intrinsic semiconductor, meaning that the number of electrons in the material is exactly equal to the number of holes. More so, for every

electron in the valence band there exists a vacant state in the conduction band that is able to receive that electron once the energy requirements are met.

Semiconductors are selected for use in thermoelectric applications because of their relatively small band gap and the ability to tune the occupation of the band gap itself. This is accomplished by adding *dopants* to the intrinsic semiconductor during its growth. A dopant is an impurity atom that replaces another atom in the crystal lattice of a material, changing its physical properties. It is an atom from neighbouring group on the periodic table to those of the host lattice which contains one more or one less electron in its outer shell. Doped semiconductors are called *extrinsic* semiconductors. An atom that provides an extra electron is called a *donor* whereas one that receives an electron is called an *acceptor*. The addition of a concentration of donors will make the host material n-type due to electrons acting as the majority carrier while the addition of acceptors will make it p-type. In the case of n-type materials, donors insert an energy level within the band gap that is close to the conduction band edge, so that extra electrons can be injected into the conduction band with minimal energy requirements. Similarly, an acceptor provides an energy level close to the valence band edge in a p-type material where it can receive electrons easily from the valence band and in turn populate it with excess holes. The new states introduced within the band gap in each of these cases change the probabilities of occupancy associated with the Fermi-Dirac distribution function. This shifts the location of intrinsic Fermi level either toward the conduction band edge or valence band edge, for n-type and p-type materials respectively. Figure 8 shows the intrinsic case again along with the extrinsic p-type and n-type band structures and the locations of their Fermi energies.

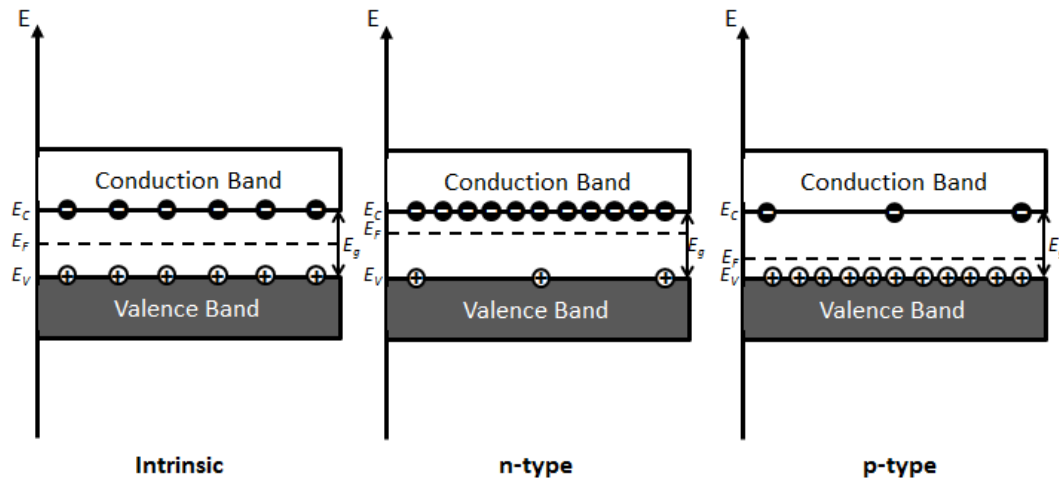


Figure 8: Simplified band diagrams of an intrinsic, n-type and p-type semiconductor at room temperature.

It is observable above that the Fermi level is located in different regions of the band gap depending on the carrier distribution of the semiconductor. The probability of an electron occupying a state that is ΔE above E_F is equal to $(E_F + \Delta E)$, which is also equal to the probability that a state located ΔE below E_F is unoccupied $[1 - (E_F + \Delta E)]$. This probability is dependent on the actual presence of such energy states. If a state does not exist at a given energy level, then the probability would automatically be zero. As previously mentioned, the concentration of electrons n is equal to the number of holes p in an intrinsic semiconductor. For every state that carries an electron in the band structure there is a corresponding vacancy that can accept that electron. Therefore the Fermi level is directly in the middle between the conduction and valence bands. Adding impurities to an intrinsic semiconductor increases the concentration of one type of carrier, electrons or holes, and this causes E_F to shift. For n-type doping, $n > p$ and the number of available states above and below the Fermi level are disproportionate. To compensate for the increased number of occupied states in the conduction band E_F increases

to remain the $\frac{1}{2}$ probability reference point. Conversely, p-type doping adds a number of holes to the valence band with $p > n$ and E_F decreases again to compensate. The effect of doping on Fermi-Dirac statistics is reiterated in Figure 9.

With the qualitative understanding of carrier transport in semiconductors complete, a brief quantitative discussion will now ensue. The carrier concentration of intrinsic semiconductors, n_i , at any temperature $T > 0K$ is represented by equation (2.9) [4], [6].

$$n = p = n_i = 2 \left(\frac{2\pi k_B T}{h^2} \right)^{\frac{3}{2}} (m_e^* m_h^*)^{3/4} e^{-\frac{E_g}{2k_B T}} \quad (2.9)$$

The quantities m_e^* and m_h^* are the *effective masses* of electrons and holes, respectively, and are further explained in reference [7]. The intrinsic Fermi level is therefore calculated by the following equation:

$$E_{Fi} = \frac{E_g}{2} + \frac{3}{4} k_B T \ln \left(\frac{m_h^*}{m_e^*} \right) \quad (2.10)$$

Equation (2.10) would seem to suggest that the intrinsic Fermi level is not in the middle of the band based on the second term. However this term becomes negligible at ambient temperature and $E_{Fi} \approx \frac{E_g}{2}$. After the addition of a concentration of donors N_D or acceptors N_A to the intrinsic case the n-type and p-type Fermi levels are offset by the following respective relations:

$$E_{Fn} = E_{Fi} + k_B T \ln \left(\frac{N_D}{n_i} \right) \quad (2.11)$$

$$E_{Fp} = E_{Fi} + k_B T \ln \left(\frac{N_A}{n_i} \right) \quad (2.12)$$

The n-type and p-type Fermi level shifts provide the necessary energy differences to create ohmic thermocouple junctions that follow the thermoelectric effects outlined in section 2.1.

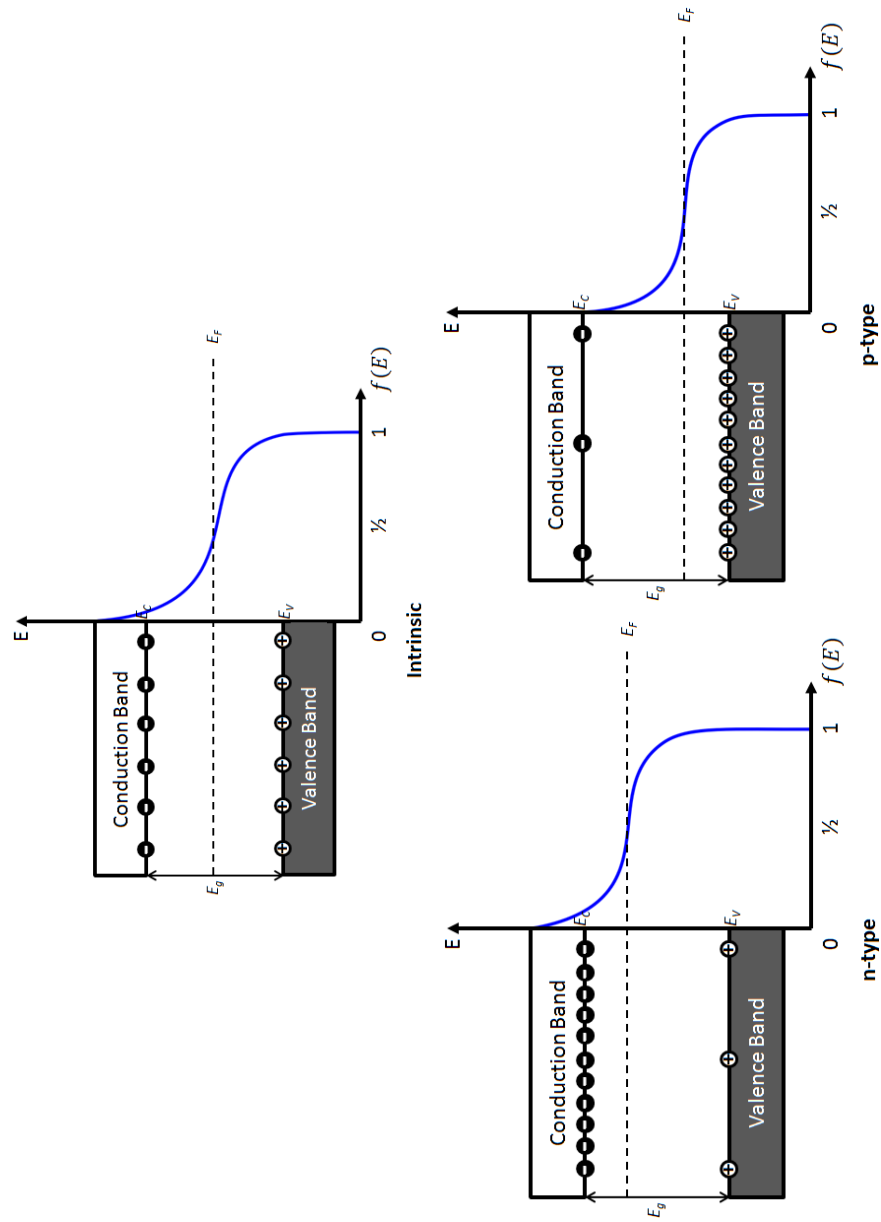
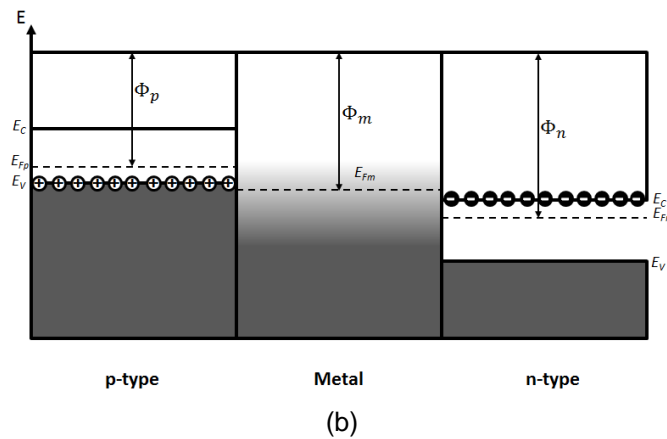
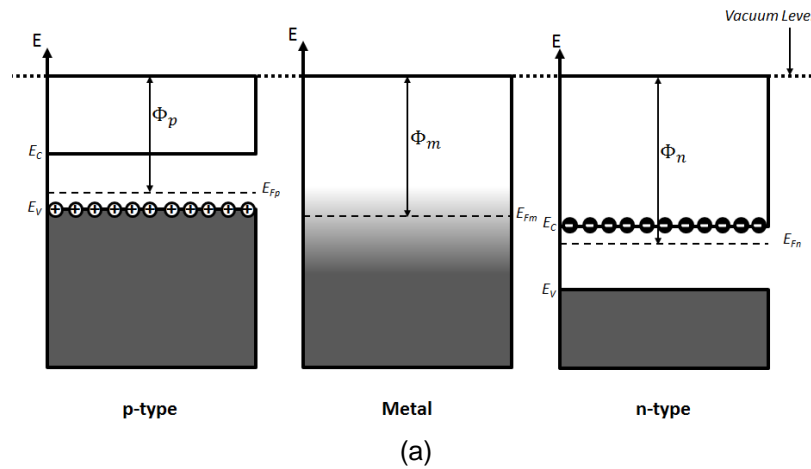


Figure 9: Fermi-Dirac distribution of Intrinsic, n-type and p-type semiconductors at temperature $T > 0K$ as recreated from [6].

2.2.2 Ohmic Junctions

Thermoelectric materials are placed into modules in the configuration *p-type – metal – n-type*. The intermediate metal layer forms an ohmic contact between the p and n segments which does not limit current flow. Upon attachment, the p-type and n-type Fermi levels respectively lower and rise to meet at the metal Fermi level. This causes a bending of the valence and conduction bands as observed in Figure 10 [7]–[9].



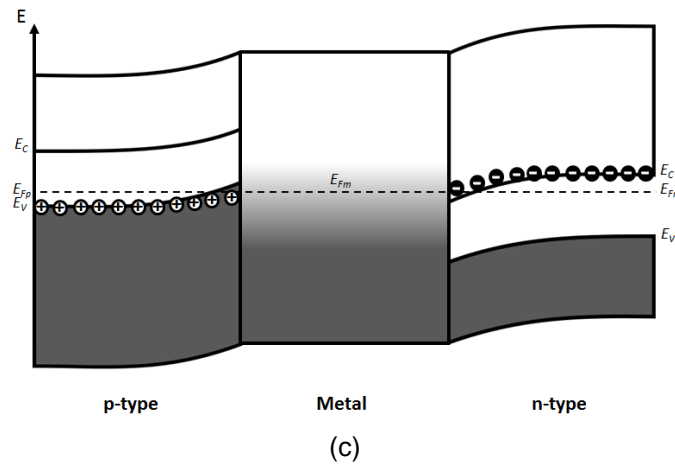


Figure 10: Ohmic junction formation (a) before bonding (b) at the point of bonding p-metal-n (c) after equilibrium has been reached.

The ability to form ohmic contacts between a metal and a semiconductor is based on the magnitudes of each of their work functions, Φ . The work function is a measure of the minimum amount of energy required to completely remove an electron from a given material in vacuum. For thermoelectric devices, it is necessary that the relative magnitudes of the work functions are $\Phi_p < \Phi_m < \Phi_n$ (Figure 10 (a)) [9]. The region at the metal-semiconductor interface where there is significant band bending is called the accumulation region of the contact. It is given this name because majority carriers in each of the semiconductors pile up at the boundary and await the absorption or release of energy to travel into or out of the adjacent material. A sample thermocouple from a thermoelectric generator is shown in Figure 11 with its band diagram under the influence of the Seebeck effect.

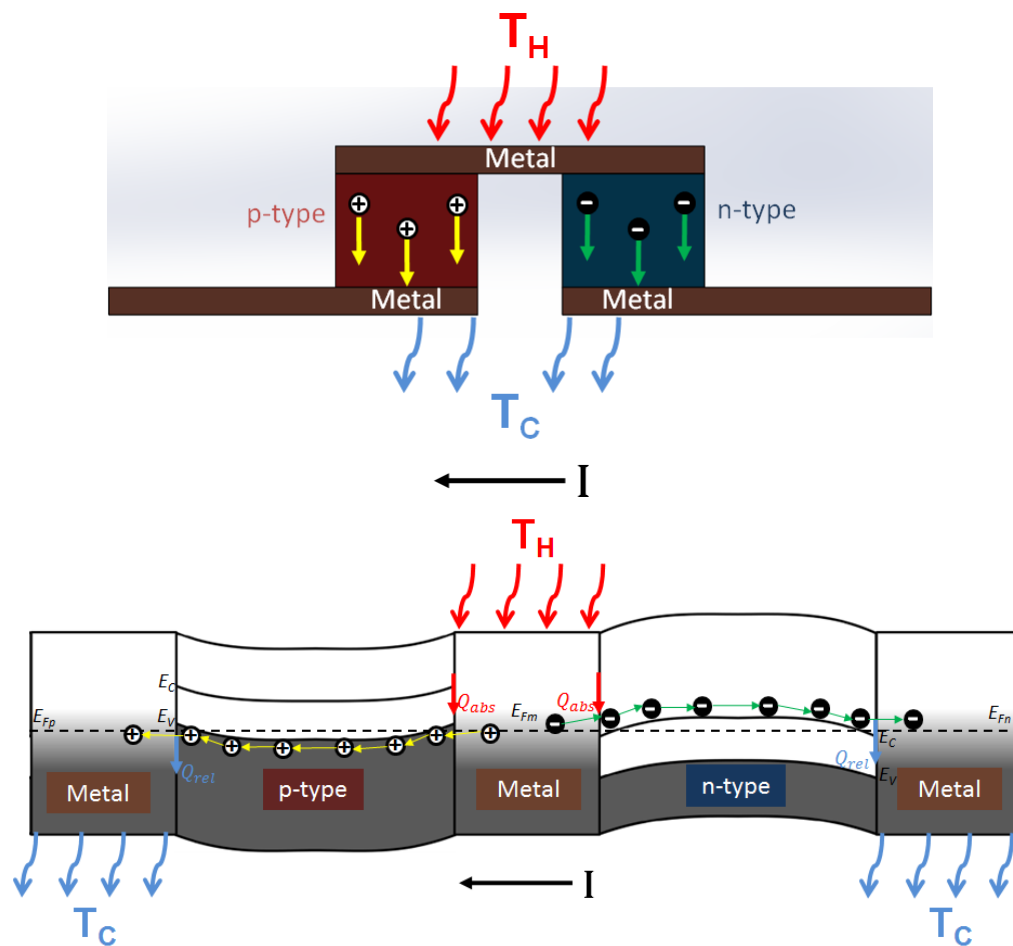


Figure 11: (Top) Thermocouple under the influence of the Seebeck effect and (Bottom) corresponding band diagram.

At the hot junction, phonons of energy Q are absorbed and increase the energy of the majority carriers. This causes them to drift towards the cold junction. Once they have travelled towards the cold junction, they release a phonon of energy Q and travel downwards into the metal. Current flow is in the indicated direction, I . This is the basic mechanism for all thermoelectric devices and is heavily dependent on the quality of materials used for each layer as well as the thermal and electrical contact conditions.

2.2.3 Thermoelectric Transport Coefficients

In addition to the Seebeck and Peltier coefficients in section 2.1, the carrier transport in thermoelectric materials is influenced by the electrical and thermal conductivities as well. The full list of transport equations derived in [10] is given below :

$$E_x = \rho J_x + \alpha \frac{dT}{dx} \quad (2.13)$$

$$J_{Qx} = \Pi J_x - \kappa_e \frac{dT}{dx} \quad (2.14)$$

$$q_x = -\kappa_L \left(\frac{dT}{dx} \right) \quad (2.15)$$

Equation (2.13) describes electrical current flow while both (2.14) and (2.15) define heat flow due to the electron and lattice components of the thermal conductivity. Further relationships for the electrical and thermal conductivities are given below which set the foundation for the definition thermoelectric performance parameter known as the Figure of Merit in the following section.

$$\sigma = \frac{1}{\rho} \quad (2.16)$$

$$\kappa = \kappa_e + \kappa_L \quad (2.17)$$

2.2.4 Figure of Merit

The three main material parameters necessary for the characterization of thermoelectric materials are the Seebeck coefficient, thermal conductivity, and electrical conductivity. Combined algebraically they yield the figure of merit, Z , for the device. This carries the units of K^{-1} . More commonly used however is the normalized figure of merit which is

the product of Z and the absolute operating temperature T of the material. The normalized figure of merit is represented in equation (2.18).

$$ZT = \frac{\alpha^2 \sigma}{\kappa} T = \frac{\alpha^2}{\rho \kappa} T = \frac{\alpha^2}{RK} T \quad (2.18)$$

A material with a ZT of 1 is typically viewed as a good thermoelectric [3]. Some common thermoelectrics are given in the diagram below.

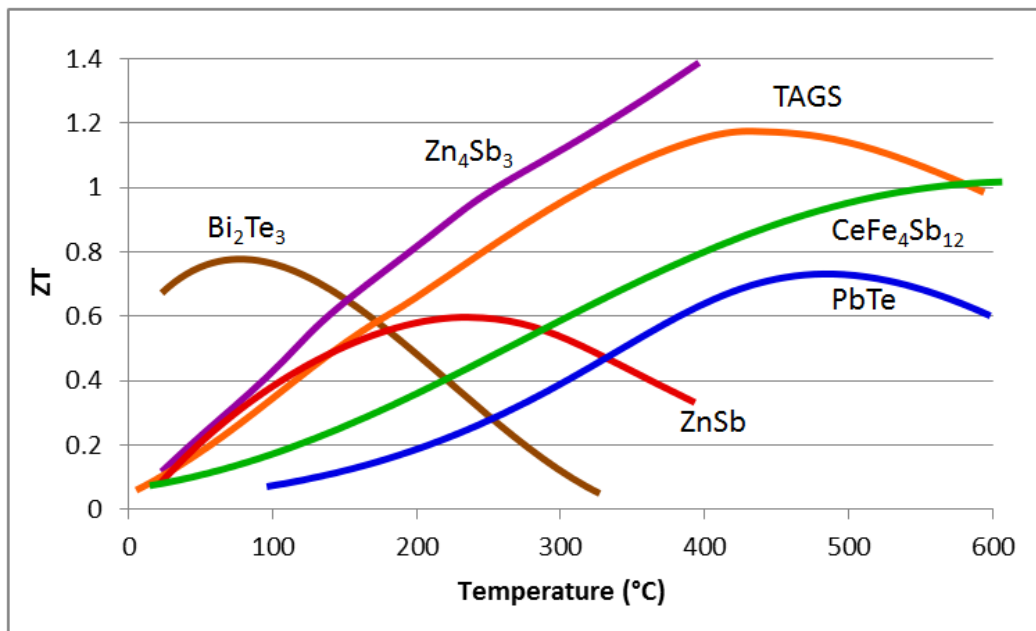


Figure 12: Normalized ZT as a function of temperature for different thermoelectric materials, recreated from [11]. TAGS are a group of alloyed materials that contain a combination of Te, Ag, Ge and Sb. Examples include AgSbTe_2 as well as GeTe [12].

The product of the square of the Seebeck coefficient and the electrical conductivity in the numerator is called the *power factor*. These are the two properties that are most influenced by the carrier concentration of the material and are the easiest to modify by doping. The thermal conductivity, although partly influenced by an electronic component, is governed mainly by its lattice component. Therefore

determining the optimal carrier concentrations in the material during the growth process will maximize the power factor and provide the greatest contribution to the improvement of ZT [12]. Figure 13 shows the effect of carrier concentration on the power factor and thermal conductivity with an estimated peak concentration around 10^{19} cm^{-3} , one that is easily attainable in semiconductors.

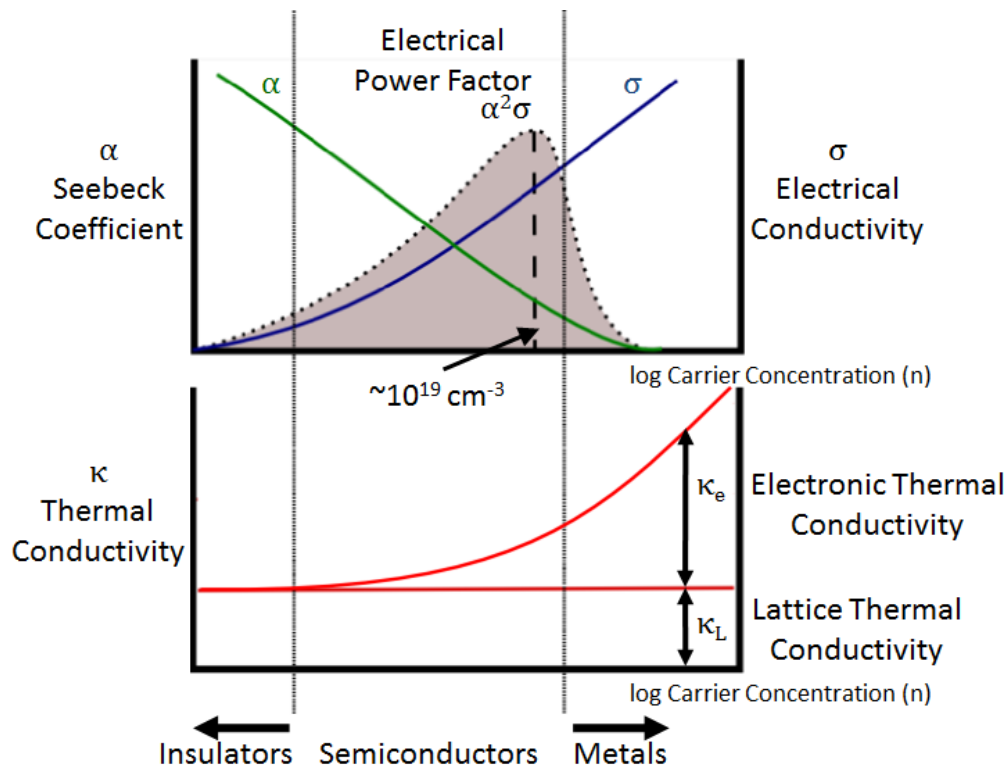


Figure 13: Dependence of electrical conductivity, Seebeck coefficient, power factor, and thermal conductivity on concentration of free carriers as recreated from [3].

This peak demonstrates the ultimate trade-off between having a large Seebeck coefficient whilst simultaneously keeping the electrical conductivity as high as possible. In actuality this peak is spread across the range of 10^{19} to 10^{21} cm^{-3} depending on the materials used for a specific temperature application, and is typical of heavily doped semiconductors [11].

2.3 Thermoelectric Modules

2.3.1 Modes of Operation

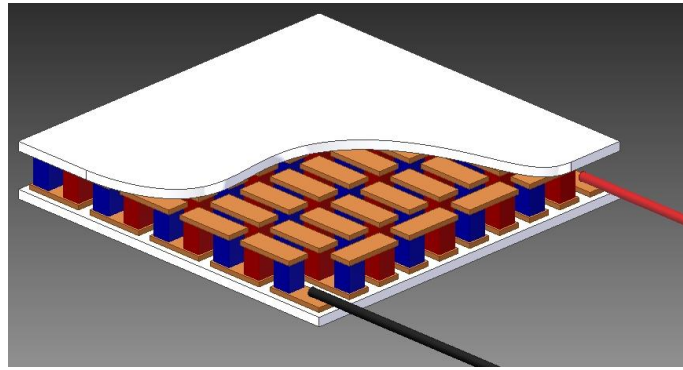


Figure 14: Cross-section of a thermoelectric module.

Thermoelectric modules consist of a number of thermocouples that are composed of the ohmic contact junctions described in section 2.2.2. The thermoelectric material most commonly used in their construction is doped Bi_2Te_3 and copper and zinc conductors are included as the intermediate metal layers. These junctions are connected electrically in series and thermally in parallel between two alumina plates for a uniform heat distribution at their cold and hot junctions. The series configuration allows a summation of the voltages created by all of the individual thermocouples at the output during power generation.

There are two types of thermoelectric modules. These are thermoelectric generators (TEGs), which utilize the Seebeck effect to generate an output voltage, and thermoelectric coolers (TECs) which operate under the Peltier effect to convert an input current into a temperature difference. The main focus of this thesis will be on TEG characterization.

2.3.2 Power Considerations

Consider the open-circuit model of a TEG is shown in Figure 15 [4].

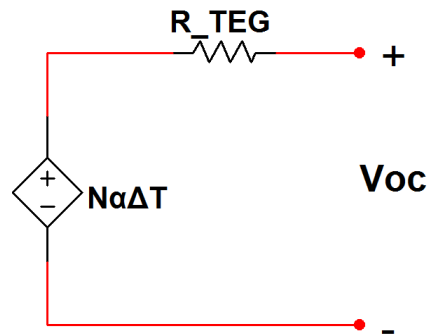


Figure 15: Open-Circuit TEG schematic.

In terms of circuit components, a TEG is simply a dependent voltage supply with an internal resistance R_{TEG} . The supply outputs the Seebeck voltage related to the ΔT applied across it. To generate power, however, it requires a load resistance as seen below:

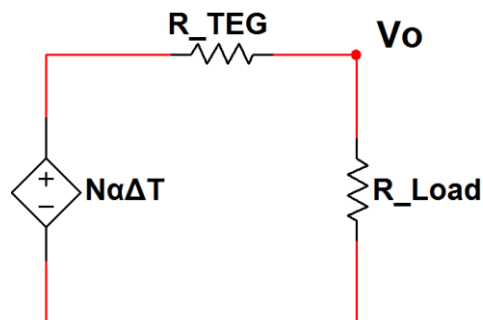


Figure 16: TEG output with a load resistor.

The voltage observed at the output, V_o , is a simple voltage divider calculation:

$$V_o = \frac{(N\alpha\Delta T)R_{Load}}{R_{TEG} + R_{Load}} \quad (2.19)$$

Where α is the average Seebeck coefficient between the p-type and n-type thermoelectric materials and N is the number of thermoelectric legs

within the module. The corresponding power across that load resistor is given by equation (2.20).

$$P = \frac{V_o^2}{R_{Load}} = \frac{(N\alpha\Delta T)^2 R_{Load}}{(R_{TEG} + R_{Load})^2} \quad (2.20)$$

It is clear that the maximum power occurs when the load resistance is equal to the TEG internal resistance. Therefore making this substitution to (2.20) yields a maximum output power of:

$$P_{max} = \frac{(N\alpha\Delta T)^2 R_{TEG}}{(R_{TEG} + R_{TEG})^2} = \frac{(N\alpha\Delta T)^2}{4R_{TEG}} \quad (2.21)$$

The thermal power applied to by the heat source and heat sink to the hot and cold sides, respectively, is given by the following equations [13].

$$\dot{Q}_H = N\alpha IT_H + K\Delta T - \frac{I^2 R_{TEG}}{2} \quad (2.22)$$

$$\dot{Q}_C = N\alpha IT_c + K\Delta T + \frac{I^2 R_{TEG}}{2} \quad (2.23)$$

The final term in each of the above equations is the effect of Joule heating, a resistive heat loss due to current flow through a material.

The efficiency of a TEG is determined by the ratio of output electrical power to input thermal power from the heat source. This is done by dividing (2.20) by (2.22) to provide [12]:

$$\eta = \frac{\frac{(N\alpha\Delta T)^2 R_{Load}}{(R_{TEG} + R_{Load})^2}}{N\alpha IT_H + K\Delta T - \frac{I^2 R_{TEG}}{2}} \quad (2.24)$$

The efficiency increases with increasing load resistance, but there is a trade off on the available output power. Typical modules operate currently with an efficiency of 3%, based on their thermoelectric properties as well as their manufacturing quality.

2.3.3 Areas of Improvement

The use of thermoelectric modules as TEGs did not occur until the last decade or so, as only TECs were commercially available. Conventionally, thermocouple elements in each configuration should contain vastly different geometries. In reference [3], expressions were derived that yield both the power output per unit area and the conversion efficiency of thermoelectric modules as functions of element length. The former expression was shown to maximize with shorter element lengths whereas the latter predicted a maximum at longer lengths. These correspond to TEC and TEG operational modes, respectively. Therefore TECs require short and broad elements for cooling while TEGs operate best with long and thin elements [3]. However most modules available today are simply repurposed TECs, and are being used for both modes of operation. This presents a logistical problem in that TEGs used in energy recovery are not manufactured in the optimal geometry to work most efficiently for energy generation.

The mass produced modules most commonly available contain polycrystalline elements of Bi_2Te_3 or similar materials that were grown using either the Bridgman or Zone Melting methods ideally. Both of these require a linear temperature gradient through which material is slowly drawn through at a fixed rate and cooled. In practice, many ingots grown commercially have varying sized grains throughout their stock – an indication of a nonlinear temperature gradient and inconsistent growth

rates. These grains thermally expand in different directions and form micro cracks in the ingot, and affect the dopant profile of the overall growth. The end result is a material that is not uniformly doped and varies in thermoelectric performance as a function of position in the ingot [3]. These materials are put into modules and are responsible for the high degree of variability in their performance. The binning technique in Chapter 6 provides a means of adapting to this spectrum of quality by rapidly testing a given batch of TEGs and selecting the best ones for use in a waste heat recovery system.

Movement to different geometries as well as more stable growth and manufacturing methods would definitely increase TEG performance capability in the future.

3. Test System Design

3.1 Selected Test Methods

A literature review of current, state-of-the-art characterization techniques indicated that there were many potential methods that could be used to extract the different thermoelectric parameters which compose the figure of merit. After thorough research, two methods were selected for implementation and these were the Harman Technique and the Parallel Thermal Conductance Technique.

3.1.1 Harman Technique

In 1958, T.C. Harman proved that the figure of merit of a thermoelectric material could be directly measured through the measurement of the Peltier effect after an AC current was applied to the sample [14]. The technique was later updated by Buist to use a bipolar DC current measurement and the use of data acquisition hardware for improved accuracy [15]. Finally, the work done by McCarty *et. al* implemented temperature compensation for improved loss minimization at higher temperatures. The development of the system in this thesis utilizes the latter two references with a focus on the work of Buist to enhance the operation of the test mechanism at room temperature for TEG modules.

The basic principle of this test is that the heat pumped via the Peltier effect is equal to the heat conducted through the sample at steady state operation. At this point, any associated losses will be neglected. With the help of equations (2.3), (2.5) and the fundamental equation for thermal conductance, the following relationship describes the basis for the Harman technique.

$$\alpha IT = K\Delta T \quad (3.1)$$

A schematic of the voltage outputs of a thermoelectric device that is subjected to a current is shown in Figure 17.

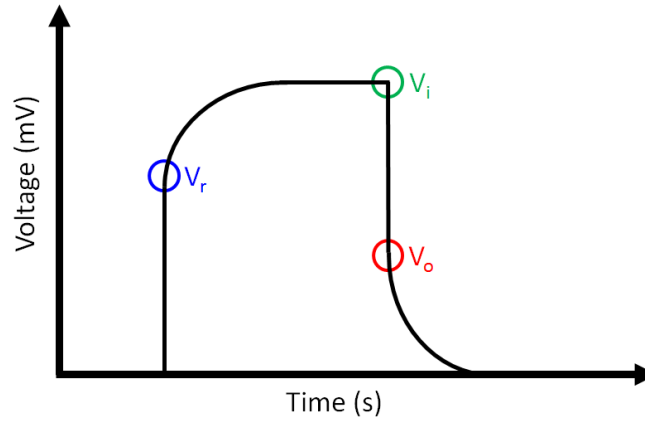


Figure 17: Voltage outputs of a thermoelectric device under the influence of the Peltier effect.

The steady-state thermoelectric voltage V_i is composed of the resistive voltage V_r and the Seebeck voltage V_o . They are combined algebraically in the following equation:

$$V_i = V_r + V_o \quad (3.2)$$

where

$$V_r = IR \quad (3.3)$$

$$V_o = \alpha\Delta T \quad (3.4)$$

Rearranging equation (3.1) to equal the Seebeck voltage in equation (3.4), the steady state thermoelectric voltage in (3.2) can be rewritten as:

$$V_i = IR + \frac{\alpha^2 IT}{K} \quad (3.5)$$

Finally with the help of equation (2.18) the normalized figure of merit ZT can be extracted from (3.5) to yield:

$$ZT = \frac{V_o}{V_i - V_o} \quad (3.6)$$

The flow of current through the device during the test will incur a resistive heat loss known as joule heating. The total amount of heat is lost to this phenomenon is equal to I^2R . For an isothermal sample, half of this heat is lost at one junction and half at the other. However since the applied current is forcing the sample to generate a temperature difference, it absorbs heat at the cold junction and rejects heat at the hot junction. Therefore the amount of joule heating at the cold junction is $+\frac{I^2R}{2}$ whereas the amount rejected is $-\frac{I^2R}{2}$ as per equations (2.22) and (2.23), respectively. This quantity of heat occurring at each junction raises the local temperature and creates an offset in the measured temperature difference across the sample. This in turn corresponds to an offset in the V_i and V_o values obtained during the experiment. To negate this effect, the current was applied in a bipolar manner [15]. This meant that the amount of Joule heat absorbed at one junction during the first current pulse would then be released from that junction during the second current pulse of opposite polarity. This created not only an electrical reversal, but a thermal reversal as well which switched hot side and cold side based on the direction of current flow. Now the offsets to the ΔT and voltages encountered during the test would be averaged out between the two measurements to yield the true values, free of the effects of Joule heating. A typical test has the input and output waveform observed in Figure 18.

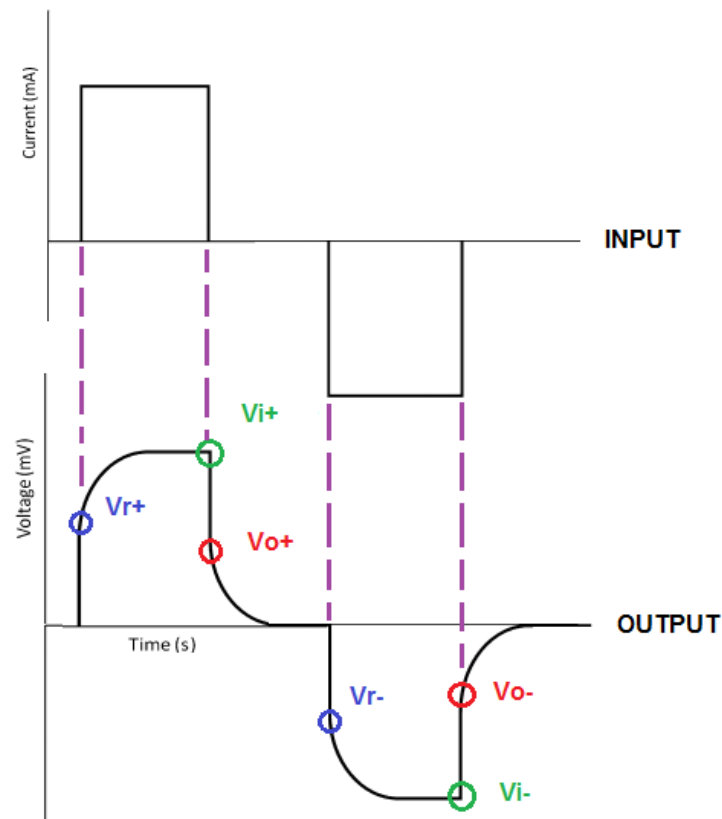


Figure 18: Illustration of the applied input and measured output during a Harman test.

The test current, I , used during the experiment is chosen to be between 1 to 4% of the current that produces the maximum temperature difference during Peltier operation, which is usually between 100 to 200mA [15], [16]. This test current is held at the same magnitude for both polarities such that the effects of heat loss and absorption on each side of the sample during thermal and electrical reversal can cancel out. After the first pulse was applied, a wait time was implemented to allow the sample to return to thermal equilibrium and the reverse current pulse was applied. The effects of varying the wait time interval between pulses at different temperatures were tested with no detectable change in the obtained ZT. The average

values of the resistive, thermoelectric and Seebeck voltages are determined according to equations (3.7) to (3.10).

$$V_{ra} = \frac{V_{r+} + V_{r-}}{2} \quad (3.7)$$

$$V_{ia} = \frac{V_{i+} + V_{i-}}{2} \quad (3.8)$$

$$V_{oa} = \frac{V_{o+} + V_{o-}}{2} \quad (3.9)$$

$$V_{ia} = V_{ra} + V_{oa} \quad (3.10)$$

The ZT obtained for the device or material under test is therefore equal to:

$$ZT = \frac{V_{oa}}{V_{ia} - V_{oa}} \quad (3.11)$$

In practice, equation (3.11) needs to be modified to account for both thermal and electrical losses. This change is expressed in section 3.5 along with a description of the origin of these losses. Experimentally, the resistive voltage is not considered in the calculation of ZT because of known transient voltage spikes associated with the switching electronics of the test system when the current pulses of Figure 18 are first applied. This can cause V_r to appear much larger than it actually is. Fortunately when the pulse is switched off, the same noise phenomenon is not present upon the detection of V_o and therefore V_r is simply calculated using equations (3.2) and (3.10), and then used to determine the resistance of the sample using equation (3.3).

The most beneficial aspect of the Harman technique is that ZT can be measured directly and is solely composed of two measureable voltages, V_o and V_i . In addition to the figure of merit, each of the quantities associated with it can be directly observed from measured data. The

Harman technique was only applied to thermoelectric modules in this thesis but could be used on individual materials as well as long as their geometries are accurately measured.

3.1.2 Parallel Thermal Conductance Technique

The most difficult thermoelectric parameter to measure effectively is thermal conductivity. This is due mainly to the associated heat losses with the test apparatus. The difficulty of this measurement is further enhanced when small samples are used. The Parallel Thermal Conductance (PTC) Technique developed by Zawilski *et al.* overcomes these obstacles with a customized subtraction method [17]. The layout of the PTC measurement apparatus is shown in Figure 19.

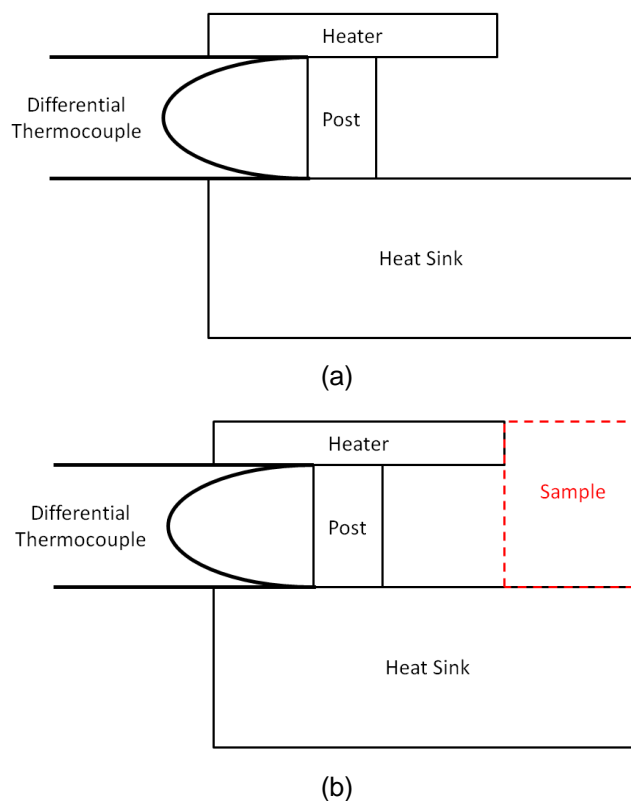


Figure 19: PTC sample holder (a) without sample and (b) with sample attached.

The heater, post, and heat sink are bonded to each other thermally in series. The two junctions of the differential thermocouple are embedded at each end of the post between the heater and heat sink to measure the

temperature difference between both points. The functionality of the differential thermocouple is discussed further in section 3.4.1.2. Neglecting any losses at the moment, power is applied to the heater and the thermal conductance of the sample holder is given by:

$$\dot{Q}_{in} = K_H \Delta T \quad (3.12)$$

The power is stepped in small increments such that the heater temperature stays relatively constant over a few data points. At each point, the system is left to stabilize until a constant ΔT is observed. A linear fit of P vs. ΔT is applied to the data points that correspond to a single heater temperature and the derivative of that function is equal to the thermal conductance of the sample holder. The power to the heater is increased until the next desired heater temperature is encountered and the process is repeated until the thermal conductance of the sample holder is characterized. The sample is then bonded with thermal paste to the holder as observed in Figure 19 (b). The thermal conductance of the entire system (holder + sample) is then measured by applying the same heater power from each previous data point until a new stable ΔT is observed that is different from the former measurement. The temperature difference will have decreased due to the additional heat path created by the sample, and a data set is created similar to that outlined in equation (3.12). The thermal conductance of the sample is obtained through subtraction of the original baseline measurement from the measurement that included the sample. This is illustrated in equation (3.13).

$$K_S = K_{H+S} - K_H \quad (3.13)$$

Knowledge of the length and cross sectional area of the sample can then yield its thermal conductivity:

$$\kappa_S = \frac{K_S L}{A} \quad (3.14)$$

The thermal conductivity is derived and plotted against operating temperature of the heater encountered at each data point for κ_S .

The original design of this test by Tritt *et al* was used to test the thermal conductivity of materials from 10 to 300K [17]. The material selected for the sample holder, particularly the post segment and bonding agents, could not withstand temperatures significantly higher than ambient. To accommodate the scope of this thesis, all construction materials for the sample holder were selected to withstand temperatures up to 300°C.

3.3 Software Overview

3.3.1 Functional Requirements

The program used to control the test hardware needed to be robust in order to ensure that multiple revisions could be made as the scope of the research became more narrowly defined. The ability to interface a myriad of electronic hardware with a pre-existing driver database was also a requirement. Finally, it was important to have access to the necessary support materials in order minimize the amount of time spent debugging code. For these reasons, the programming language LabView was selected to write the test program.

3.3.2 Description of Code

3.3.2.1 Harman Technique Code

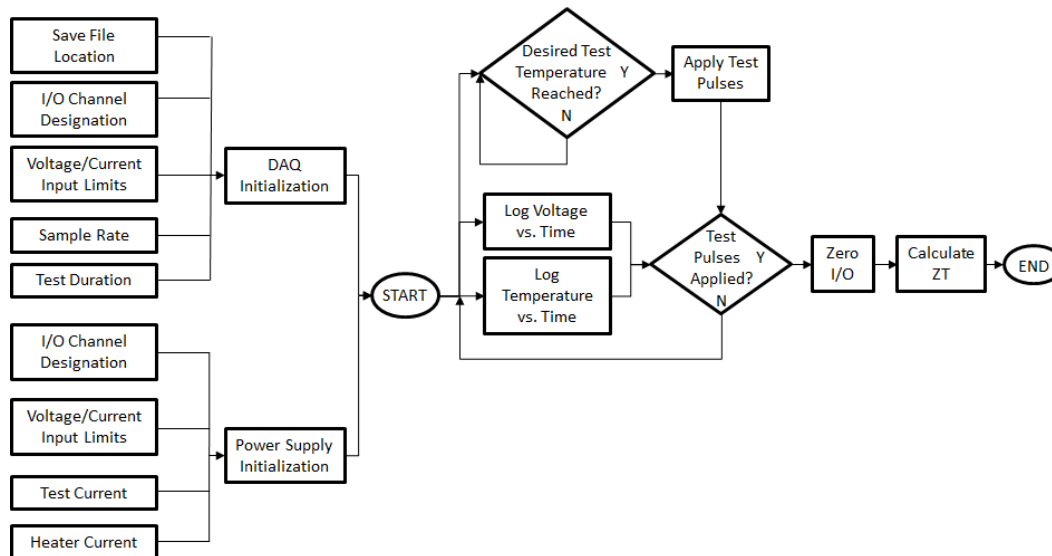


Figure 20: Harman Technique Functional Block Diagram

The LabView code is summarized in the functional diagram shown in Figure 20 above. The DAQ and power supply I/O channels and their limits are set only once and are saved for future test iterations. The test duration is set here as well. Once the test starts, the sample voltage and temperature are plotted with respect to time, along with the radiation guard and heater temperatures. When the desired heater temperature has been met and the sample temperature remains constant, the experimenter can select to apply the test pulses. After the second pulse, the test is complete and the inputs and outputs of the DAQ and power supply are set to zero. Finally the ZT is calculated using the values obtained during the test. The entire Harman Technique LabView code can be found in Appendix B.

3.3.2.2 PTC Code

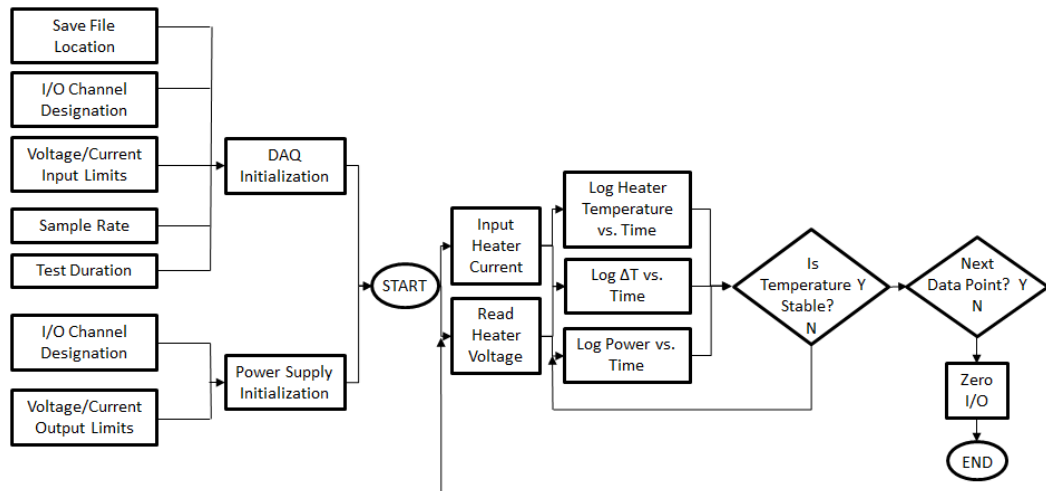


Figure 21: PTC Functional Block Diagram

Figure 21 shows the block diagram for the PTC code written in LabView. Like the Harman Technique code, the DAQ and power supply limits are initialized once, and the test begins after the experimenter has input the desired heater current. The heater voltage is simultaneously read, and thus the heater power, temperature, and sample temperature are displayed graphically as a function of time. Once the sample temperature is stable, the experimenter can choose to input another heater current to create a new data point, or simply end the test. The full LabView code can be found in Appendix C.

3.4 Hardware Overview

3.4.1 Electronics

3.4.1.1 Data Acquisition Unit (DAQ)

The four main criteria necessary for selecting a DAQ for this project were:

- i. The ability to resolve voltage transitions observed in thermocouples as small as $38\mu\text{V}/^\circ\text{C}$.
- ii. A sampling rate fast enough to detect the transient voltage change during the Harman Technique on the order of μs .
- iii. At least two analog output channels and six analog input channels to control and read the auxiliary electronics of the test system
- iv. The ability to control the DAQ using the LabView programming language.

The USB-6211 Data Acquisition Unit from National Instruments was selected for use in the test facility. It was chosen based on the factors listed above. It contains a 16-bit resolution analog-to-digital converter capable of resolving $31\mu\text{V}$ voltage steps, a sampling rate of 250 kHz, eight digital i/o channels, two analog output channels and eight differential analog input channels. It is also compatible with LabView. The full specifications for this DAQ can be found in the Device-Specific Information section of reference [18].

Buist mentioned in [15] that the use of a high speed, high resolution DAQ was necessary in order to accurately determine the transition from the steady state voltage to the Seebeck voltage observed in the Harman technique. The DAQ in the literature at the time of publication also had a 16-bit resolution, but had a sampling rate that yielded a wait time of a few milliseconds between data points. This long time interval made it difficult to pinpoint the exact switching moment during the measurement since the voltage would decay rather quickly after the input pulse was shut off. The true value of the Seebeck voltage was in turn unable to be captured in the raw data. This necessitated the use of a linear approximation to

extrapolate to the true Seebeck voltage based on the first few data points of the decay.

The USB-6211 utilizes an *aggregated* sampling rate of 250 kHz, meaning that its true sampling rate is equal to 250 kHz divided by the number of active analog input channels present in the experiment. The proposed test facility uses all eight analog input channels between the thermoelectric voltage and temperature measurements, which only allows for a maximum sample rate of 31.25 kHz per channel. This corresponds to a time between samples of 32 μ s, a number that is two orders of magnitude smaller than the wait time used in the literature. When the same linear approximation was implemented during the current testing, it provided a result that was equivalent to taking the first reading of the Seebeck voltage after the perceived switch point. This indicated that the sampling rate of this DAQ was able to accurately capture the switching time of the sample voltage during the test without the need for any further extrapolation.

3.4.1.2 Temperature Sensors

The range of temperatures encountered in testing spanned from 25°C to 200°C. As such, it was important to use devices that were optimized for use over these temperatures. Two types of temperature sensors were implemented in the test facility; platinum resistive temperature devices (RTDs) and type T thermocouples.

The RTD used was the TH100PT from ThorLabs and was selected for its effectiveness over the desired temperature range. Its resistance-temperature correlation polynomial is given by equation (3.15):

$$T = 3383.8095 - 0.0866 \cdot \sqrt{1.7585 \cdot 10^9 - 2.31 \cdot 10^6 \cdot R_T} \quad (3.15)$$

R_T is the resistance in Ω at a given temperature T in $^{\circ}\text{C}$ [19]. The resistance of the RTD was measured using a simultaneous voltage and current measurement across the device using the following circuit adapted from [20]:

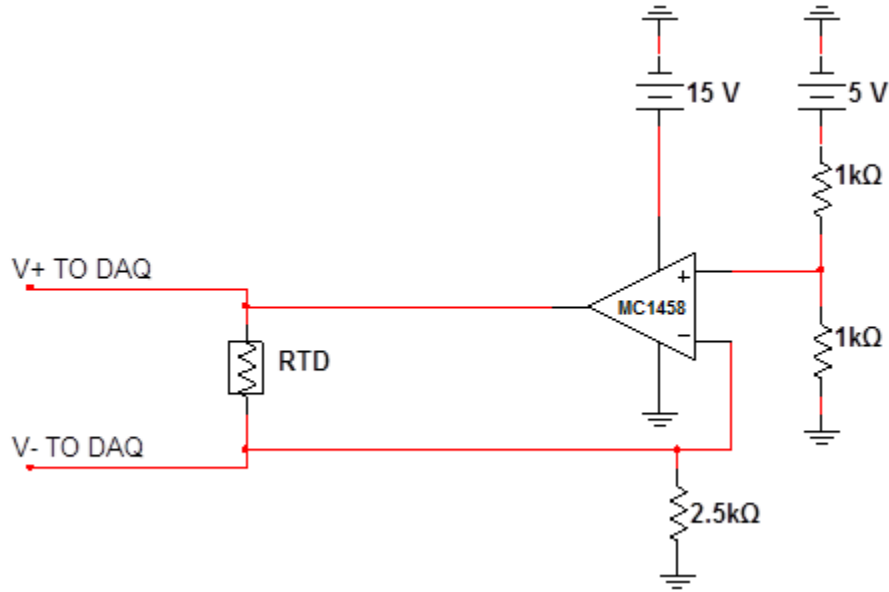


Figure 22: RTD Constant Current Drive Circuit.

The RTD is biased in Figure 22 by an operational amplifier which acts as a constant current source of 1mA. This level of current creates a negligible amount of joule heating within the RTD and does not offset the local temperature being detected [21]. The voltage drop across the RTD yields the resistance, R_T at the test temperature:

$$R_T = \frac{V_+ - V_-}{0.001A} = \frac{\Delta V_{RTD}}{0.001A} \quad (3.16)$$

Combining equations (3.15) and (3.16) provides a real-time temperature measurement that is able to adjust to random voltage and current fluctuations in the auxiliary components.

The thermocouples from Omega are type T and are 0.001” (0.025mm) in diameter. They were selected for their size and ability to withstand up to 350°C. Being so small, they added a minimal thermal mass to the Harman and PTC measurement systems that did not noticeably disrupt the path for heat flow. Typically, one junction is in contact with the surface under test and a second junction is created out of the same two metals and placed in an ice bath at 0°C. The difference in their output voltages is directly proportional to the temperature of the hot measurement junction. This relationship is observed in the following polynomial for type T thermocouples:

$$T = \sum_{i=0}^6 c_i V^i \quad (3.17)$$

where the coefficients c_0 to c_6 are reproduced in Appendix A from [22].

These thermocouples were modified for use in the Harman and PTC test facilities. Here, a differential thermocouple was needed to observe the temperature difference between two points and that thermocouple needed to be as small as possible. Differential thermocouples were created by arc welding the constantan wires of two individual thermocouples together, which allowed for an absolute measurement of the temperature difference between their two junctions. The T in equation (3.17) is replaced with a ΔT in the case of a differential thermocouple.

Figure 23 depicts a newly constructed differential thermocouple. The metal bead in the centre represents the point at which the arc welding occurred. The voltage output of this thermocouple is read between the two copper wire leads.

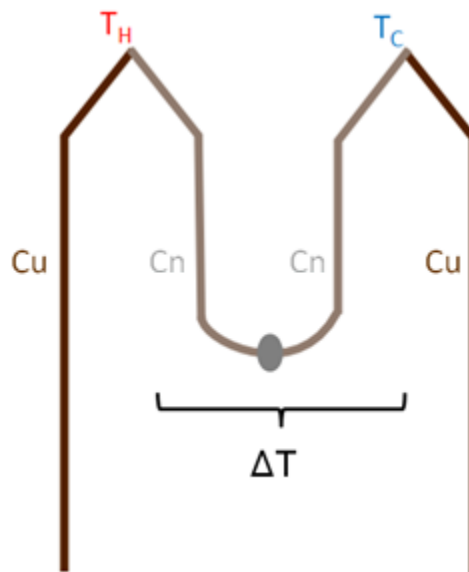


Figure 23: Illustration of a Type T Differential Thermocouple.

3.4.1.3 Power Supply

The BK Precision 9130 triple output supply was used to provide both the power to the heaters as well as the bipolar constant current pulse in the Harman Technique. Since there were at most three different voltage sources required during testing, a single unit supply was a suitable choice for both space and programming requirements. Two outputs are used to maintain the heaters at a desired temperature and can supply up to 30V and 3A. The third output is used only during the Harman Technique and is set to the desired test current limit of 150mA. The 9130 is controlled by a subroutine in the main LabView program and communicates with the PC via serial interface.

3.4.1.4 Auxiliary Circuit

The DAQ, power supply, and temperature sensors are all interfaced within an auxiliary circuit board which is depicted in Figure 25. The board is composed of five main subsections.

Part A is an h-bridge constructed from five npn MOSFETs which controls the direction and duration of the constant current pulse applied during the Harman technique.

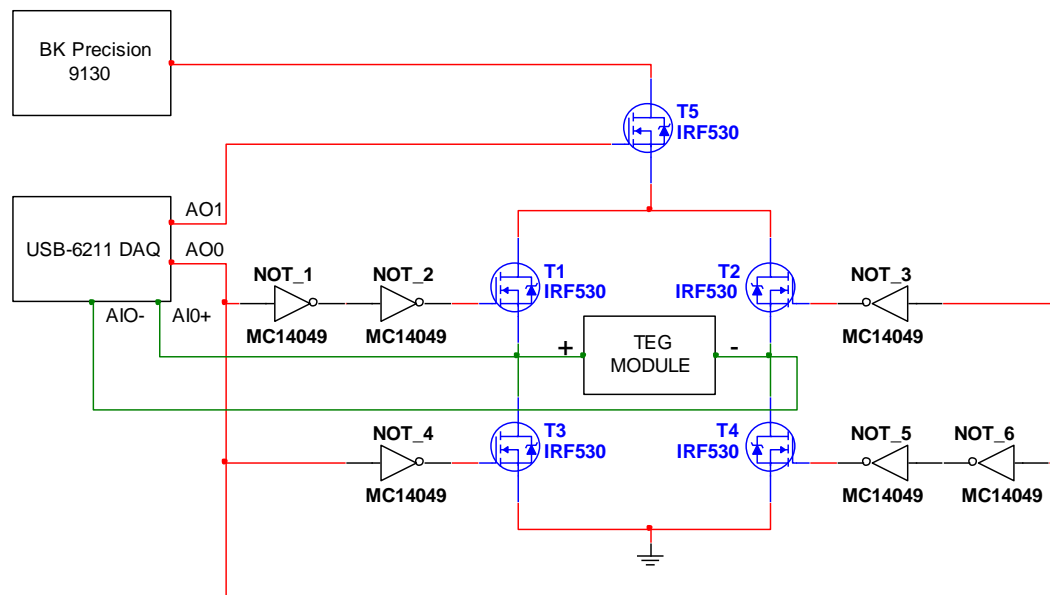


Figure 24: H-bridge subsection of auxiliary circuit.

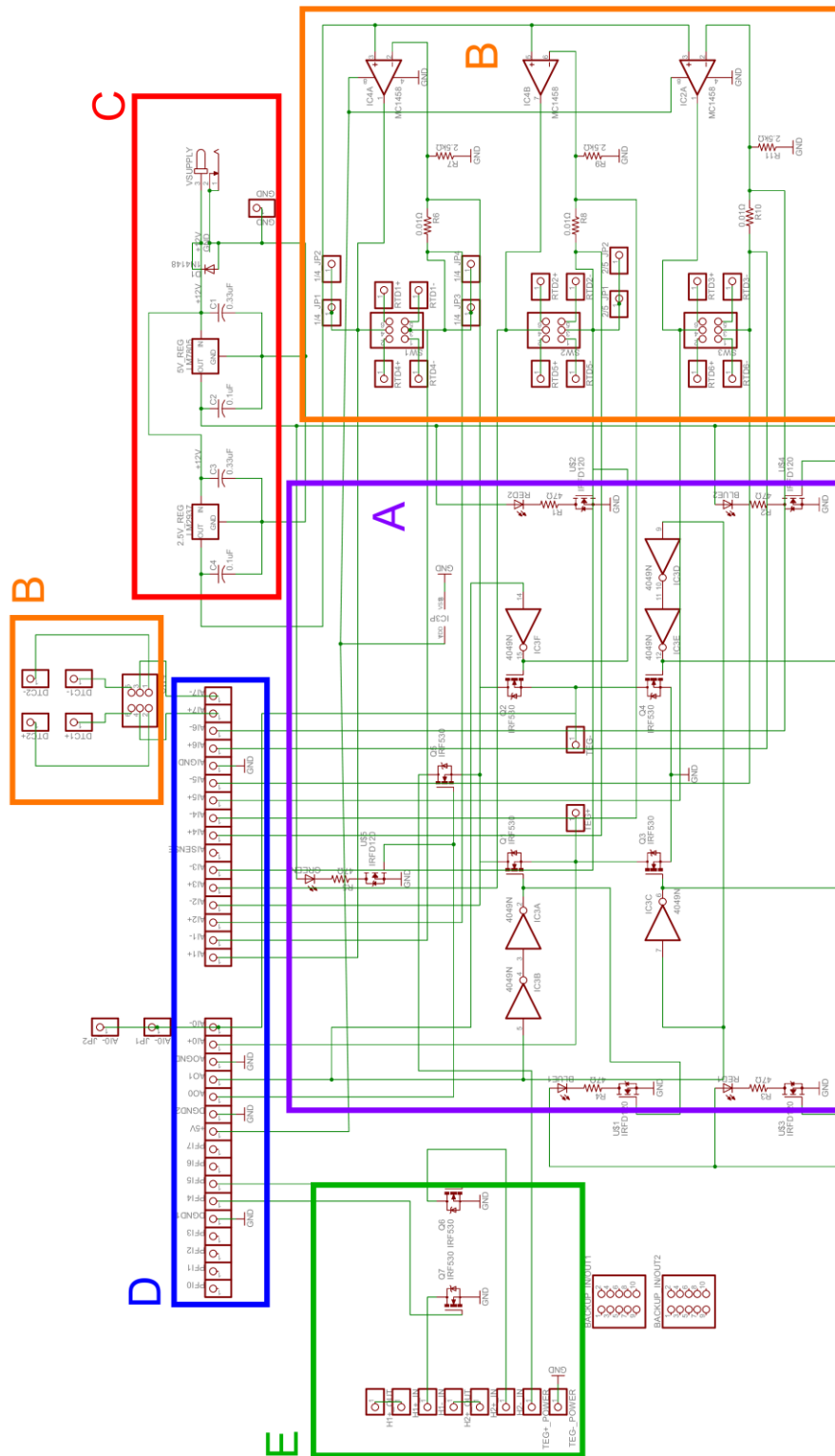


Figure 25: Schematic of Auxiliary Circuit. (A) H-bridge sub-circuit. (B) Temperature sensor interface. (C) Circuit power. (D) DAQ interface. (E) Power supply interface.

A more detailed view of the h-bridge subsection is shown in Figure 24. Here, the sample is connected between two parallel pairs of transistors. The output from pin AO0 on the DAQ indicates the direction of current flow through the sample with the assistance of six NOT gates found on the MC14049 hex inverter integrated circuit. If the output is logic high, then transistors T1 and T4 are turned on and facilitate current flow in the positive direction across the sample. Conversely, a logic low output from the same pin switches on transistors T2 and T3 and allows current to flow in the negative direction. Pin AO1 from the DAQ outputs a square wave pulse that switches on transistor T5 for a fixed length of time to allow current from the power supply to reach the remainder of the circuit. When T5 is no longer biased, there is no current being driven through the sample anymore. The remaining four transistors are left switched on in their most recent path configuration to allow the sample a path to ground in order to determine its Seebeck voltage. A second h-bridge is connected in parallel to this one which receives the same inputs. When two transistors are switched on within the main h-bridge, two analogous ones are also switched on in the secondary h-bridge and illuminate LEDs. These indicate to the experimenter the duration and direction of current flow through the sample.

Part B contains the temperature sensors and their related sub-circuits that were described previously in part 3.4.1.2. Each of these sub-circuits is able to accommodate two of its preferred sensor type, whether RTD or thermocouple, through the addition of a dual throw switch at the location where the sensor connects to the rest of the electronics. These switches are labelled in Figure 25.

Part C is the power supply for the circuit electronics. This supply is separate from the 9130 and is provided by a 12V DC adapter. From here,

a 2.5V and a 5V are enabled and are used as a reference voltage for the RTDs and as a supply for the directional LEDs, respectively.

Part D is simply a direct reproduction of the DAQ output pin configuration made on the auxiliary circuit. This allows for ease of assembly and troubleshooting.

Part E contains the connections for the 9130 that link to the heaters in both the Harman and PTC test systems. These connections have larger trace widths on the circuit due to their increased current throughput during operation of up to 3A.

The board layout for this circuit can be found in Appendix D.

3.4.2 Physical Interface

3.4.2.1 Test Facility

The test facility is a modular design that allows the switching between both the Harman Technique and the PTC Technique test systems. A single vacuum chamber has been outfitted with four support posts that contain two platforms to hold the heater, sample and radiation guard of the desired test. Figure 26 to Figure 29 show both the cross-sectional and isometric views of the vacuum chamber outfitted for the Harman Technique and the PTC Technique, respectively.

The platforms were constructed out of pyrophyllite, a machinable ceramic with a low thermal conductivity of approximately 1.5 W/m·K. This, coupled with stainless steel support posts, ensures that a minimal amount of heat will be conducted into the chamber walls and they will not be hot to touch. A groove is cut into the bottom platform to allow the sensor and heater wires to reach under the radiation guard. The guard is a 0.0625" thick copper sheet that has been folded and welded into an enclosure.

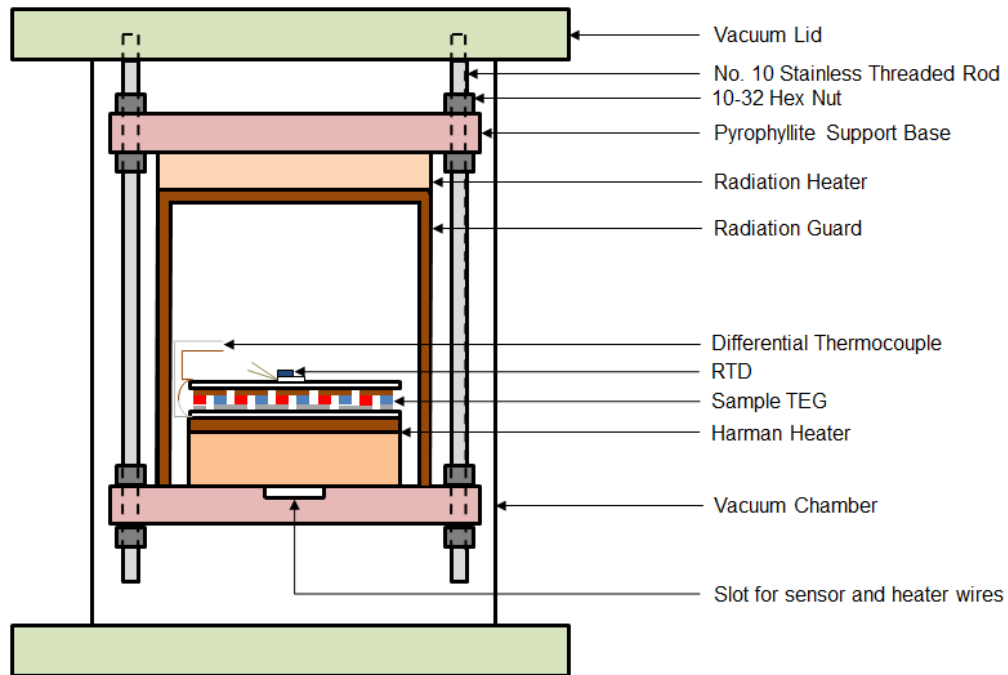


Figure 26: Cross-sectional view of the Harman Technique test system with sample TEG and temperature sensors included.

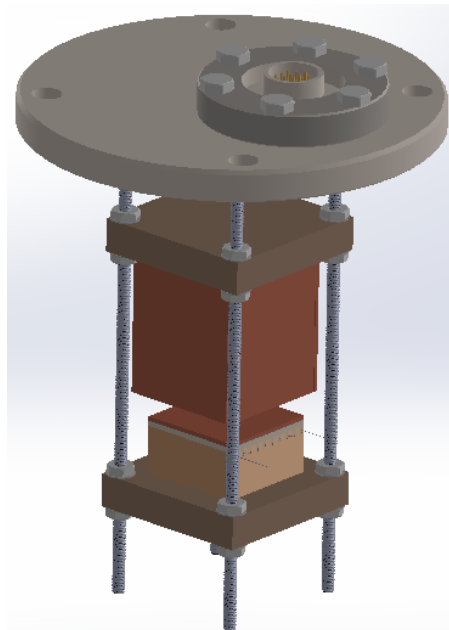


Figure 27: Isometric view of the Harman Technique test system without sample TEG and temperature sensors.

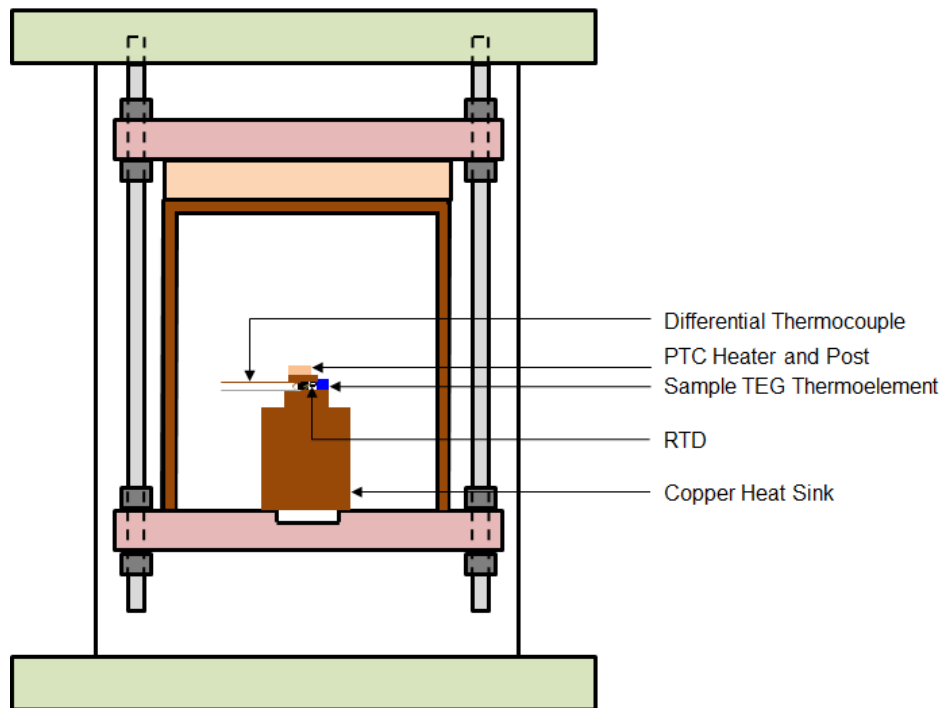


Figure 28: Cross-sectional view of the PTC Technique test system.

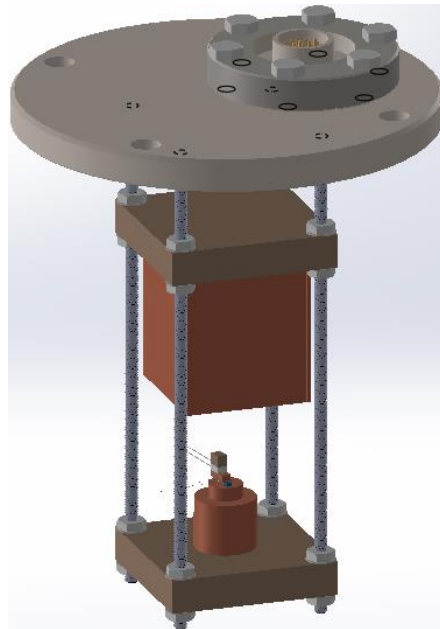


Figure 29: Isometric view of the PTC test system.

3.4.2.2 Custom Heaters

Testing at elevated temperatures was accomplished with the use of custom-built heaters designed specifically for the Harman and PTC test systems. These functioned using resistive heating and received currents of up to 3A to produce a range of temperatures from 50°C to 300°C.

3.4.2.2.1 Design and Construction

The main criterion for design of these heaters was to deliver a uniform heat flux to the sample during testing. For modules this ensured that all of the thermoelements were heated evenly so that a maximum voltage output could be measured. Figure 30 displays the CAD rendering of a custom heater used in the Harman test system in both its fully constructed and exploded views.

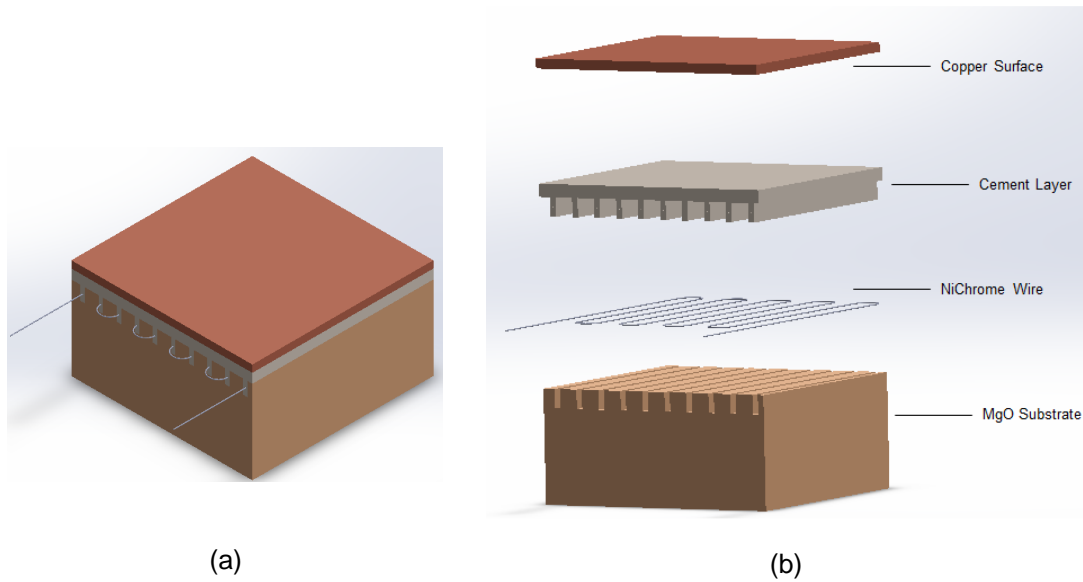


Figure 30: (a) Isometric view and (b) exploded view of heater constructed for use in the Harman test system.

The heater consists of four layers; a porous MgO substrate, 32 AWG NiChrome resistive heating wire, OMEGABond 600 thermal cement, and a 1.5875mm thick copper surface layer to create a uniform heat profile for the sample.

A piece of MgO was cut to the size of 40mm x 40mm x 12.5mm. Grooves were then cut 4mm deep into the top face and spaced evenly across the surface. The NiChrome wire was routed through the grooves and cut to allow 10mm length ends to extend from the heater for electrical contacts. The top surface was then coated with a 2mm thick layer of thermal cement, which served to both encapsulate the wire in the grooves and to bond the copper plate to the substrate.

The length of NiChrome wire used was determined in part by the geometry of the base. This length is assumed to be composed of both straight and semi-circle arc components, with the wire situated directly in the centre of each groove as illustrated in Figure 31.

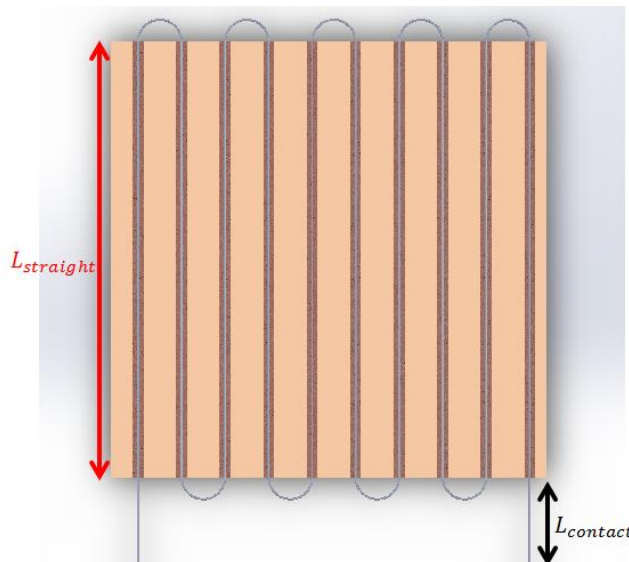


Figure 31: Heater wire configuration with emphasis on straight components.

This configuration allocated for the potential addition of extra wire due to offsets from cutting or variability in tightness of the winding of the wire through the grooves. The formula for calculating total wire length for a heater of any size is represented by equations (A.1) and (3.19) with their associated parameters displayed in Figure 32.

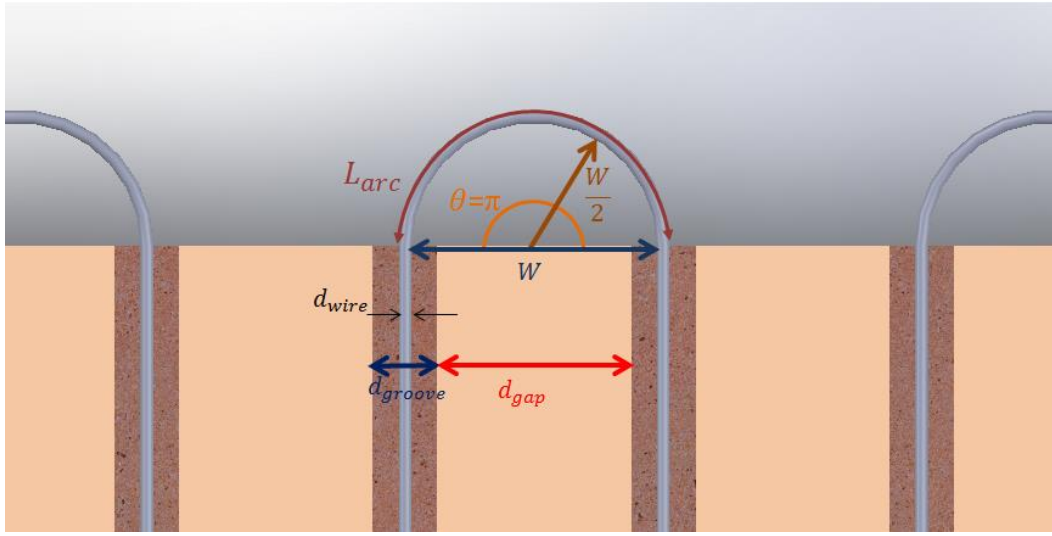


Figure 32: Sample arc length segment of heater wire.

$$L_{total} = N_{grooves} \cdot L_{straight} + 2 \cdot L_{contact} + N_{arc} \cdot L_{arc} \quad (3.18)$$

$$L_{arc} = \left(\frac{W}{2}\right) \pi = \left(\frac{d_{groove} - d_{wire} + d_{gap}}{2}\right) \pi \quad (3.19)$$

Equation (3.19) is simply the formula for arc-length, with the radius of the arc equal to the expression containing the wire, groove and gap thicknesses, and the angle θ equal to π rad. The heater constructed for the Harman Technique, observed in Figure 30, had the following specifications listed in Table 1.

Section	Value
$L_{straight}$	40mm
$L_{contact}$	10mm
d_{groove}	1mm
d_{wire}	0.202mm
d_{gap}	4mm
$N_{grooves}$	10
N_{arc}	9
L_{total}	488mm

Table 1: Dimensions of heater components and total heater wire length.

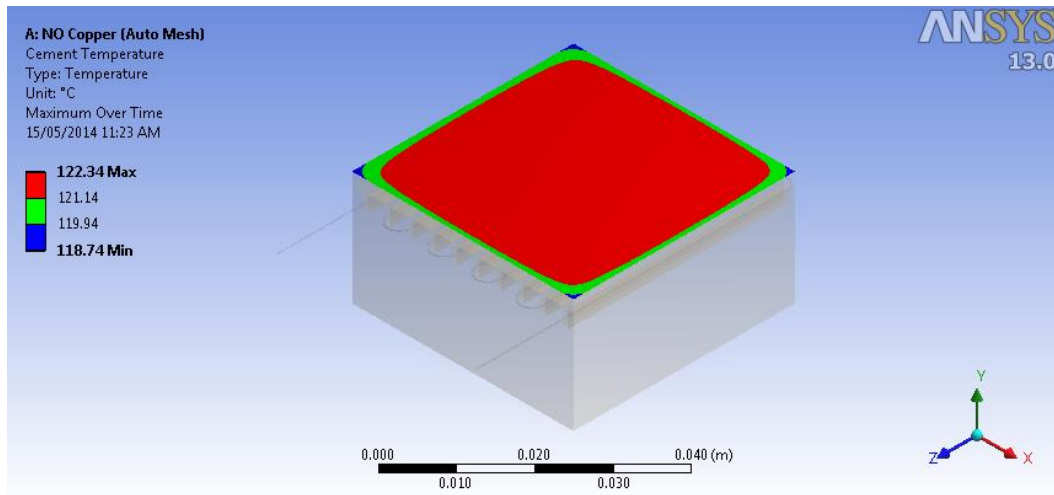
After calculating the wire length, its temperature vs. current characteristics were determined using industry data to verify that it would be able to heat past the upper limit temperature of 300°C with the output from the power supply.

3.4.2.2.2 Modelling

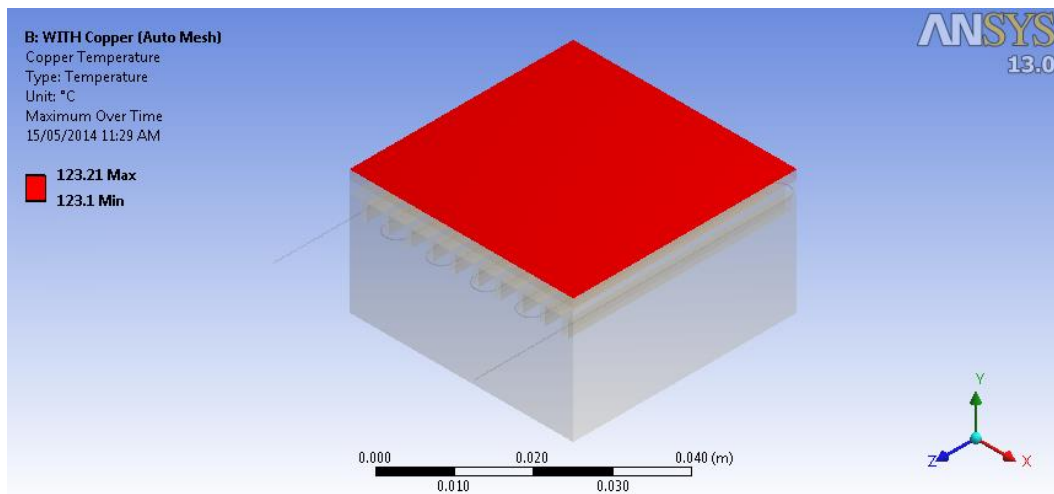
The heater was modelled in ANSYS Workbench using the steady state Thermal-Electric simulation environment. Two simulations were run to validate the uniformity of the top surface temperature and heat flux profile. One was performed with the copper plate and one without. This helped to emphasize the necessity of the copper for uniform heat distribution and delivery to the TEG so that all of the elements could receive the same thermal input conditions. The material properties needed for these simulations were the thermal conductivities at numerous temperatures of each of the constituent parts of the heater. The electrical resistivity of the NiChrome wire as a function of temperature was needed

as well. The aforementioned thermal conductivities can be found in Appendix E, along with the electrical resistivity of the NiChrome wire.

The heater geometry from Figure 30(a) was created in SolidWorks and imported into ANSYS Workbench where the thermal and electrical properties mentioned previously were input. The boundary conditions applied during the simulation are summarized in Appendix F. These consist of the radiative and convective components encountered in an ambient environment.



(a)



(b)

Figure 33: Heater surface temperature (a) without copper surface and (b) with copper surface.

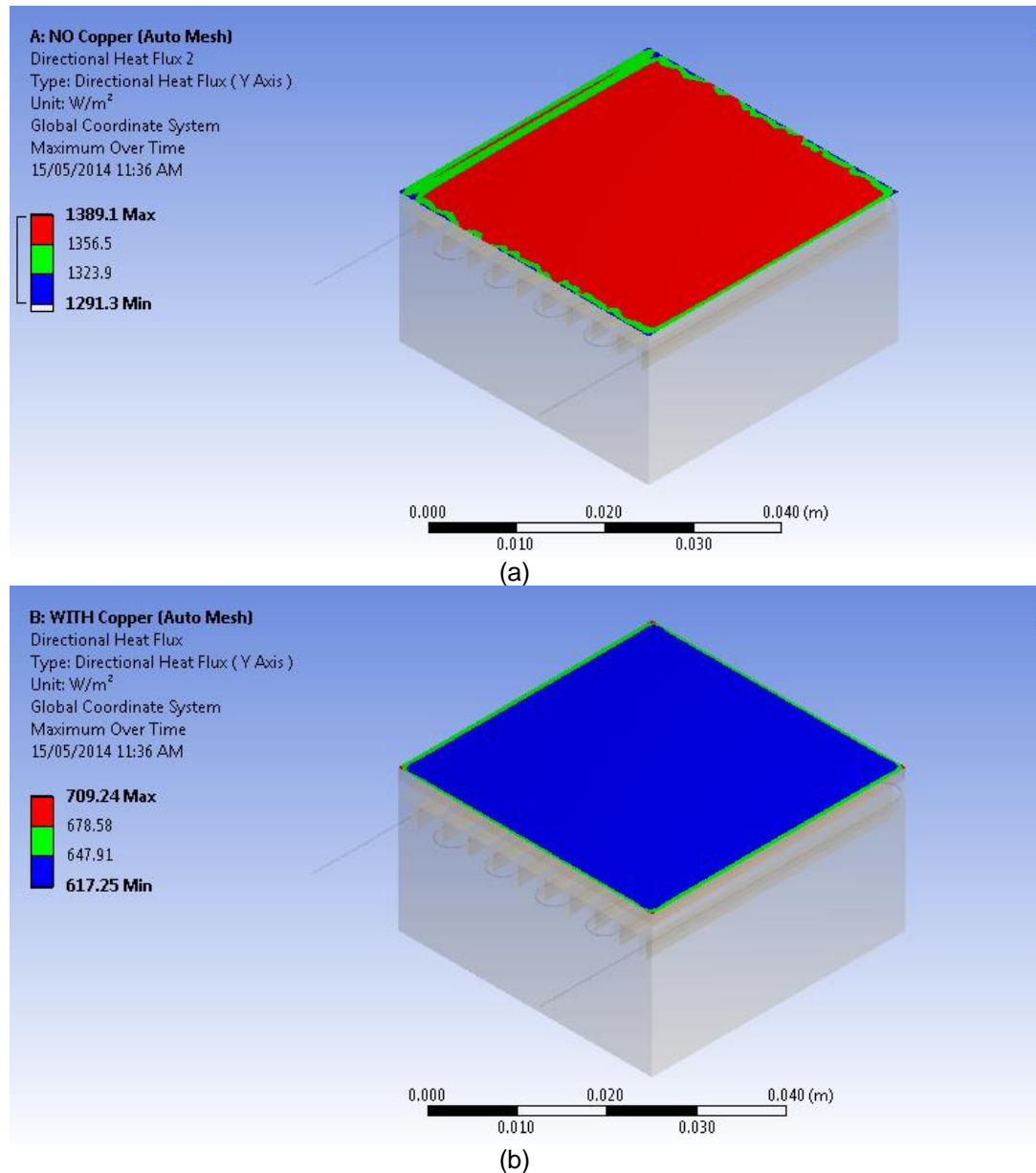


Figure 34: Heater surface heat flux (a) without copper surface and (b) with copper surface.

The simulation results in Figure 33 show that there is a deviation of up to 3°C in the temperature profile of the heater without copper, whereas the copper strip limits this deviation to 0.2°C. Similarly, the heat flux

results in Figure 34 show significant edge effects before the addition of the copper plate.

3.4.2.2.3 Proof of Operation

The temperature distribution of the heater was experimentally tested using an unreferenced type T thermocouple junction attached to a micrometer stage. The thermocouple tip was dragged across the top surface of the heater while it was applied a constant current and operated at a steady state. Measurements of the thermal voltage were taken at 1.33mm increments until the entire cross-sectional length of 40mm was traversed. The thermocouple remained at a given location until its output voltage settled at a constant value. A repeatable thermal voltage at all test points indicated uniform heating across the surface, whereas a varying voltage with position indicated the formation of hot spots and thus, uneven heat flow to the sample. A uniform temperature distribution was observed as seen in Figure 35 but only occurred after the copper surface was bonded to the heater. This was due to the high thermal conductivity of the copper. This same characterization process was performed for the heater used in the PTC test system as well.

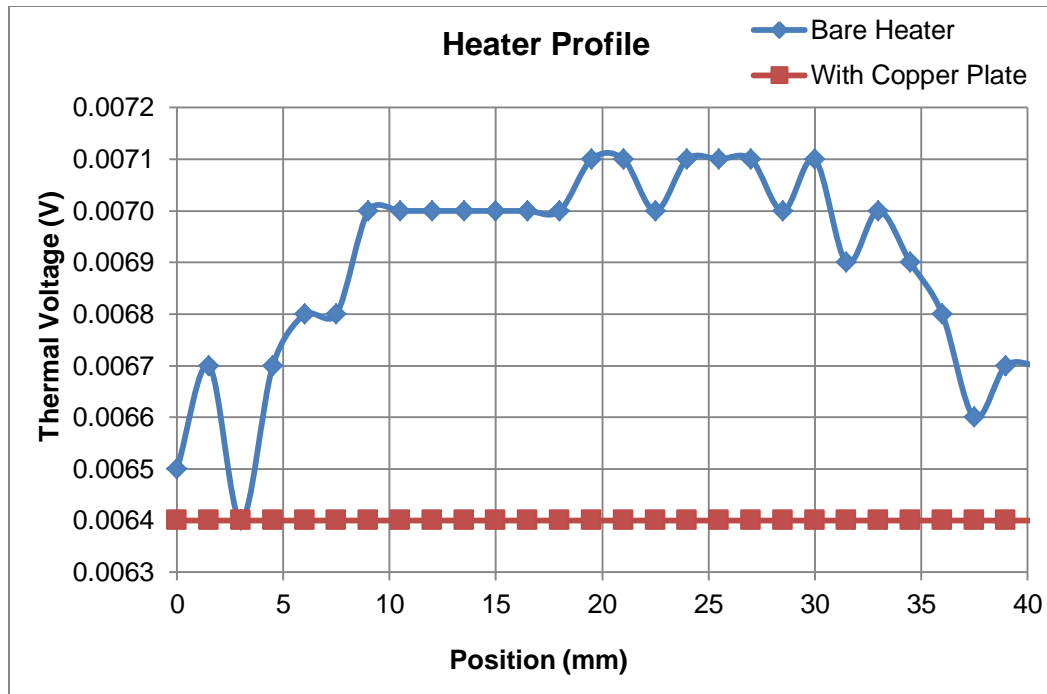


Figure 35: Top surface heat distribution of heater with and without copper plate.

3.5 Loss Minimization

Efforts were made to quantify all of the associated losses within both measurement systems, and reduce them where possible. All measurements and simulations were performed within an evacuated environment so that convection and air conduction could be automatically neglected. The remaining thermal and electrical losses are derived in the following sections. These losses and their uncertainties are tabulated in Appendix G.

3.5.1 Harman Technique

3.5.1.1 Thermal Losses

It was necessary to create stable thermal contacts between the sample and its respective heater during testing to obtain repeatable

results and minimize test time. This ensured that as the sample was maintained at a desired test temperature that it was receiving a uniform flux from the heater along its entire surface of contact. In order to achieve this, a minimal amount of thermal paste was applied to the contact area on the sample. The sample was applied a slight pressure in all lateral directions to ensure that it could not move from its position after it had been set in place. The thermal paste used was Silicone 860 from MG Chemicals which had a thermal conductivity of 0.657 W/m·K and a maximum operating temperature of 300°C [23]. Although the use of thermal paste provided a good thermal bond between the heater and the TEG, it would be beneficial in the future to add a clamping mechanism to this test system that can apply different contact pressures to the TEG so that the effects of thermal resistance can be further quantified. At this point, the final loss to be considered is radiation.

The heat balance equation for the Harman technique is given in the following equation and is reminiscent of equation (3.1) but with an additional term accounting for heat loss from radiation.

$$\dot{Q}_k + \dot{Q}_{Rad} = \dot{Q}_\Pi \quad (3.20)$$

Due to the bipolar nature of the Harman technique, heat is conducted through the sample twice during a test. The hot and cold sides effectively switch since the Peltier effect is ultimately being utilized in two directions.

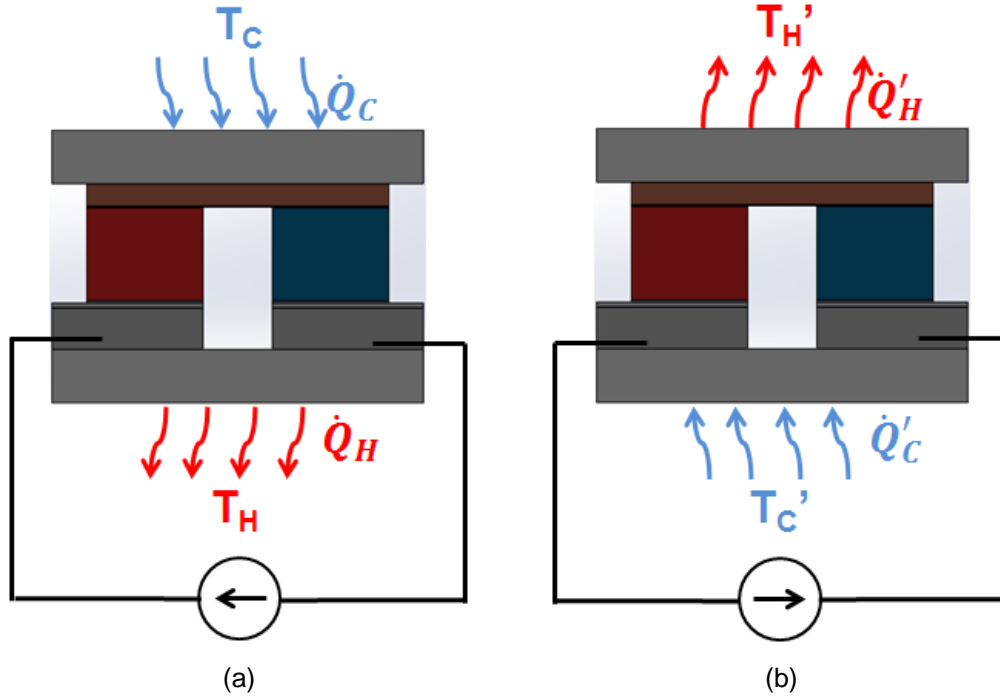


Figure 36: Example of the current applied during the Harman technique in (a) forward bias and (b) reverse bias. The associated temperatures that form at the outer surfaces are a result of the direction of the current.

This necessitates the inclusion of D_a which is the sum of the temperature differences observed in each polarization.

$$D_a = (T_H - T_C + T_H' - T_C') \quad (3.21)$$

The Peltier heat term can be written in terms of previously mentioned measurable quantities as well, with an updated equation for the Seebeck coefficient of the TEG elements.

$$\dot{Q}_\Pi = N\alpha I(T_a + T_a') \quad (3.22)$$

$$T_a = \frac{T_H + T_C}{2} \quad (3.23)$$

$$T'_a = \frac{T'_H + T'_C}{2} \quad (3.24)$$

$$\alpha = \frac{2V_{oa}}{ND_a} \quad (3.25)$$

For the fully characterized TEG, model TEG1B-12610-5.1, that was also used for simulation purposes in section 4.1, the sum of the radiative losses due to all of its constituent materials is provided in equation (3.26)

$$\begin{aligned} \Sigma \dot{Q}_{Rad} = & \dot{Q}_{Al_2O_3T} + \dot{Q}_{Cu} + \dot{Q}_{Sn} + \dot{Q}_{NiT} + \dot{Q}_p + \dot{Q}_n + \dot{Q}_{NiB} + \dot{Q}_{Al} \\ & + \dot{Q}_{Zn} + \dot{Q}_{Al_2O_3B} \end{aligned} \quad (3.26)$$

The terms listed above can vary depending on the materials present in a given module. The general equation for radiation loss between two surfaces is adapted from [24] below for the materials in a TEG .

$$\dot{Q}_{ij} = A_i F_{ij} \sigma_B (\varepsilon_i T_i^4 - \varepsilon_j T_j^4) \quad (3.27)$$

This equation describes the net radiation transfer from surface i with area A_i to surface j. The coefficient F_{ij} is the calculated view factor between the surfaces and is a percentage of how much of the total emitted radiation from surface i that strikes surface j and vice versa. All of the view factors between the faces of the materials listed in (3.26) and each exposed face of the Bi_2Te_3 TEG elements were calculated using the perpendicular and parallel rectangular face view factor equations from [25]. A sample calculation of each of these view factors is given in Appendix H. Equation (3.27) is repeated for *every exposed face* of the TEG elements and summed to create each of the terms present in (3.26), substituting coefficients with the subscript j with the respective emissivity, exposed

surface area and local temperature of the desired material. The coefficients ϵ_i and T_i are the emissivity and average temperature of the TEG elements, respectively. The dimensional information for each contact layer used to calculate the exposed surface area was taken from an SEM image of a single TEG thermocouple. This process is described in detail in Chapter 4.

The local temperature of a layer was approximated depending on its location in the TEG. The layers above the p-type and n-type legs were assumed to be at T_C on the forward pulse and T_H' on the reverse pulse. Similarly, the layers below the legs were at T_H during the forward pulse and at T_C' during the reverse pulse. The legs themselves were assumed to have an average between the two extreme temperatures observed during each pulse. The total conducted heat through the TEG elements after both pulses were applied is given below as well [15].

$$\dot{Q}_k = \frac{N\kappa AD_a}{L} \quad (3.28)$$

By combining equations (3.23) through (3.28), the thermal conductivity can be solved for algebraically and is given in equation (3.29) with the newly formed thermal loss correction factor, C_L in equation (3.30).

$$\kappa = \frac{2V_{oa}IL(T_a + T_a')C_L}{NAD_a^2} \quad (3.29)$$

$$C_L = 1 - \frac{(\sum \dot{Q}_{Rad}) D_a}{2V_{oa}I(T_a + T_a')} \quad (3.30)$$

A lossless system would have $C_L = 1$. As temperature increases, the amount of radiation increases proportionally to T^4 therefore this factor can greatly affect the value of thermal conductivity and also ZT if not

considered. To minimize radiation loss, an active radiation guard was placed over the sample and the heater. The surface of this shield was maintained at the same operating temperature as that of the outermost top surface of the TEG. This is the top Al_2O_3 layer. During each of the steady-state operation portions of the test, the temperatures T_C and T_H' are measured and the guard heater has power applied until its surface temperature reaches the same observed temperature. This practice was first implemented by McCarty in [16] and is called *Top Temperature Matching* (TTM). Since both of these surfaces are radiating at the same temperature the net radiation loss from the top layer is equal to zero. The elements themselves are operating under a temperature gradient and therefore are not radiating at a single fixed temperature. Their average temperature is approximated to that of T_a or T_a' depending on the direction of the applied pulse and their net radiation loss to the guard is lowered but not negated.

The calculated values for C_L in this thesis take into account the effects of the TTM procedure by including the radiative heat transfer between the TEG elements and the radiation guard. Only the faces of the outermost elements have a reduced radiation output since they have a direct line-of-sight with the guard. The view factors between the faces of the interior legs and the guard were calculated to be less than 0.01 and their radiative contributions were therefore neglected. The values of C_L are plotted below with respect to the total average sample temperature.

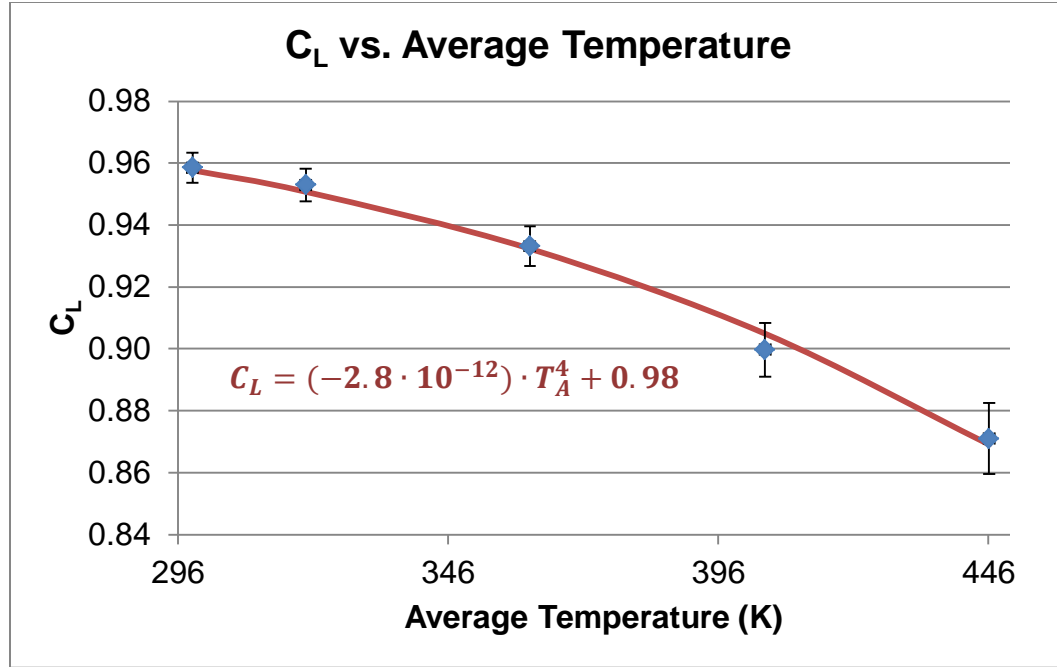


Figure 37: Calculated values for C_L vs. Heater Temperature.

The correction factor has a maximum uncertainty of 2.6% at the average temperature 446K which corresponds to the 200°C heater temperature data point. Remarkably, this factor can simply be approximated for any TEG as strictly a function of average temperature in the form of equation (3.31), with the values for μ and γ given in Figure 37.

$$C_L = \mu T_A^4 + \gamma \quad (3.31)$$

$$T_A = \frac{T_H + T_C + T'_H + T'_C}{4} \quad (3.32)$$

The average temperature mentioned above is the average of all four test temperatures encountered during a Harman test. The implementation of equation (3.31) allows for a significantly reduced calculation time of C_L and only adds a maximum of 0.2% uncertainty to the final ZT results that use this factor.

The introduction of a loss correction factor was originally proposed Buist in [15] and applied by Fujimoto *et al* in [26]. However both of these sources used a cyclical set of equations involving C_L and κ . This presented a problem since in order to calculate C_L the thermal conductivity needed to be known and vice versa, until both values converged through an iterative computing process. This calculation was simplified in this thesis by starting with the heat balance equation given in (3.20) and working towards the set of equations in (3.29) and (3.30). Here, both C_L and κ are independently defined and are composed of directly measureable quantities. The consequences of excluding C_L from the measurements will be discussed in Chapter 5.

3.5.1.2 Electrical Losses

The p-type and n-type elements in a TEG are bonded to intermediate metal layers which provide a channel for heat conduction as well as for current propagation. The existence of these layers adds contact resistance which produces an offset in the resistive voltage defined by equation (3.3). The resistive voltage is directly proportional to the resistivity of the TEG elements as seen below.

$$V_r = \frac{I\rho L}{A} \quad (3.33)$$

Although the procedure outlined in this thesis does not measure V_r directly, it is still calculated with the help of equation (3.2). This equation will be rewritten taking into account the contact voltage, V_c .

$$V_i = V_o + V_r + V_c \quad (3.34)$$

$$V_c = IR_c \quad (3.35)$$

V_c is simply the product of the input current and the total resistance created by all of the contacts within the TEG, R_c . The voltage drop across the bottom and top contacts was determined in ANSYS where the current density flow profile through the contacts could be explicitly evaluated. This was done with the help of the dimensional and compositional analysis of an SEM image of a single TEG thermocouple. This process provided a theoretical maximum for the contact voltage, and subsequently, the contact resistance based on equation (3.35). The resulting V_c and R_c values were then multiplied by the number of thermocouples in a TEG to yield the entire TEG contact resistance.

Equations (3.33), (3.34) and (3.35) are combined to calculate the contact resistance and subsequently the contact voltage and yield a more accurate value of the TEG resistivity. The averaged versions of the voltages in equation (3.34) are used instead so that the effects from the bipolar measurement can be considered. The contact voltage was found to be equal in both of the applied current directions. A factor of N is also included to account for the number of elements in a TEG module.

$$\rho = \frac{(V_{ia} - V_{oa} - V_c)A}{NIL} \quad (3.36)$$

The values for V_c and R_c versus average temperature are given below in

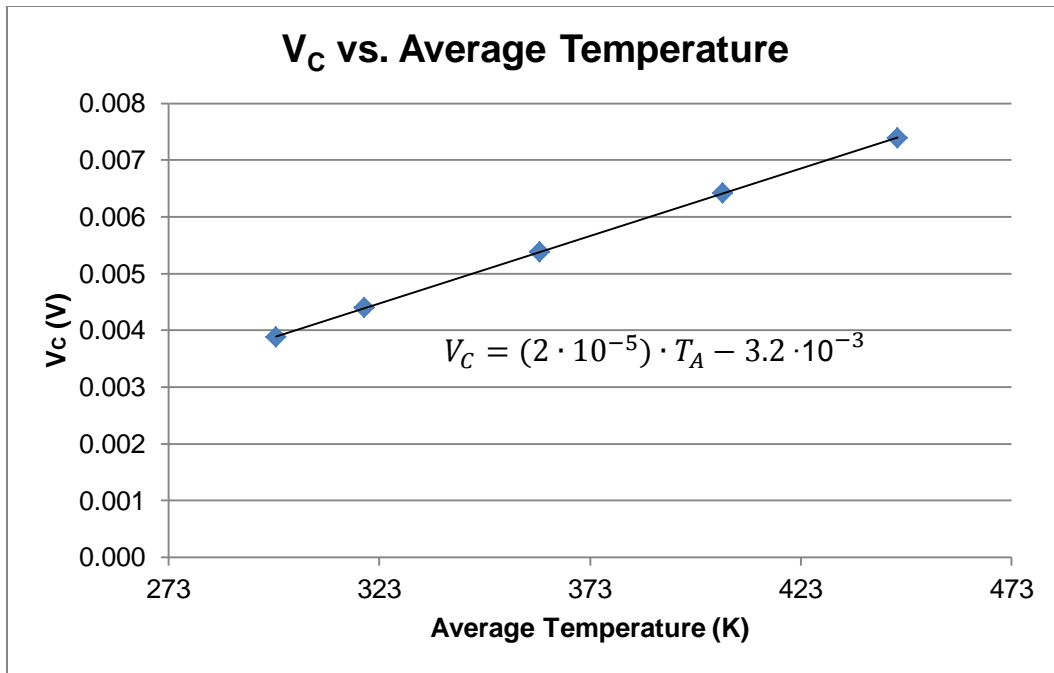


Figure 38: V_C vs. average temperature.

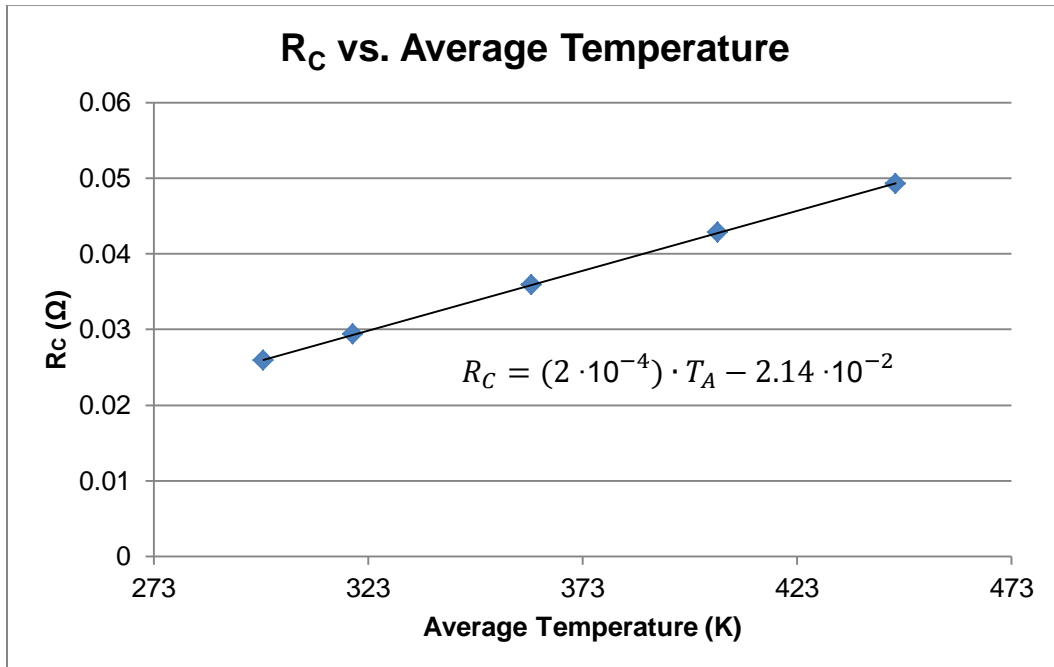


Figure 39: R_C vs. average temperature

It is observed above that the contact voltage follows a linear trend with increasing temperature for a given TEG. This also applies to the contact resistance since it is linearly proportional to V_c . The expressions provided in Figure 38 and Figure 39 are valid for the model TEG1B-12610-5.1 and would differ in other models with different contact geometries and compositions.

With both the thermal and electrical losses quantified, the equation for ZT must now change to account for both of these phenomena, as observed in equation.

$$ZT = \frac{V_{oa}}{C_L(V_{ia} - V_{oa} - V_c)} \quad (3.37)$$

As with the thermal losses, the effects of including V_c in the calculation of ZT will be observed in the results in Chapter 5.

3.5.2 Parallel Thermal Conductance

3.5.2.1 Thermal Losses

The heat balance equations for the PTC apparatus are given in the equations below for each test configuration.

$$\dot{Q}_{in} - K_H \Delta T_1 - \dot{Q}_{rad_H} = 0 \quad (3.38)$$

$$\dot{Q}_{in} - K_{H+S} \Delta T_2 - \dot{Q}_{rad_{H+S}} = 0 \quad (3.39)$$

Solving for the thermal conductance in each of (3.38) and (3.39) and applying equation (3.13), the thermal conductance of the sample is determined.

$$K_S = \frac{(\dot{Q}_{in} - \dot{Q}_{rad_{H+S}})\Delta T_1 - (\dot{Q}_{in} - \dot{Q}_{rad_H})\Delta T_2}{\Delta T_1 \Delta T_2} \quad (3.40)$$

Finally, applying the values for the sample geometry yields the sample thermal conductivity, given below:

$$\kappa_S = \frac{L}{A} \frac{((\dot{Q}_{in} - \dot{Q}_{rad_{H+S}})\Delta T_1 - (\dot{Q}_{in} - \dot{Q}_{rad_H})\Delta T_2)}{\Delta T_1 \Delta T_2} \quad (3.41)$$

It is evident that the only losses associated with this system are radiative, since the test would be performed in vacuum as previously mentioned. Each of the sample holder components would radiate with a different emissivity, however the heater reaches the highest temperature so it would most likely dominate. It would therefore be necessary to temperature match a radiation shield to the heater temperature in order to minimize the effects of the greatest loss in the system. The κ measured during this procedure is assumed to be constant between the two thermal configurations since the heater temperatures are within a few degrees from each other.

4. ANSYS Modelling

Both characterization techniques explored in this thesis were modelled using ANSYS Workbench finite element software. A tutorial found in [27] acted as a guide for evaluating thermoelectric phenomena within the ANSYS user interface. Like the simulations for the heater output in section 3.4.2.2, the Thermal-Electric environment was used which focused specifically on providing results based on the three key thermoelectric parameters; the Seebeck coefficient and the electrical and thermal conductivities.

4.1 Harman Technique Model

A preliminary literature review focused on the work of McCarty *et al* who modelled the Harman Technique from -55°C to 250°C using a temperature-normalized set of thermoelectric parameters [16]. The Thermal-Electric modelling environment was used to determine the steady-state thermoelectric and resistive voltages. This environment can only model steady-state operation, so the Seebeck voltage which diminishes over time could not be explicitly modelled. Nevertheless, the equation for ZT given previously by equation (3.11) was modified with the help of (3.10) to now include the average resistive voltage, V_{Ra} . This equivalent representation of ZT is given as:

$$ZT = \frac{V_{ia} - V_{Ra}}{V_{Ra}} \quad (4.1)$$

Here, V_{Ra} is used because it contains both the TEG element resistive voltage V_{ra} as well as the undesired contact voltage, V_C . V_r is a reliable voltage output because its detection is not affected by any potential noise that would be associated with physical measurement equipment as

discussed in section 3.1.1. The simulation of the contact voltages during a Harman test allows for the addition V_C to equation (4.1) to improve its accuracy. Unlike the thermal losses which are simply boundary conditions that are applied or removed, this electrical loss is intrinsic to the TEG geometry and must be accounted for in the calculation of the theoretical ZT.

$$ZT = \frac{V_{ia} - V_{Ra}}{V_{Ra} - V_C} \quad (4.2)$$

where, in this simulation environment,

$$V_{Ra} = V_{ra} + V_C \quad (4.3)$$

$$V_{ia} = V_{oa} + V_{Ra} \quad (4.4)$$

The model developed in this thesis uses the same principles as above and was created to verify Harman test results for TEG modules observed in the laboratory. First, a module was dismantled and a single thermocouple was removed with all of its layers intact. The sample was placed in an SEM and underwent EDS to obtain dimensional and compositional information of each layer.

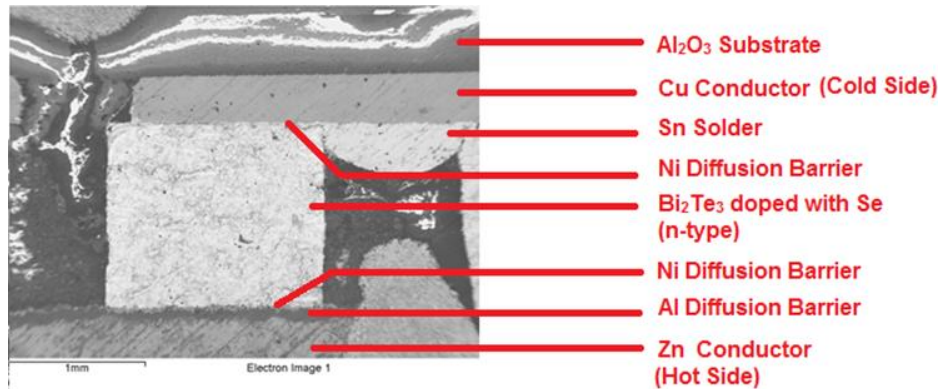
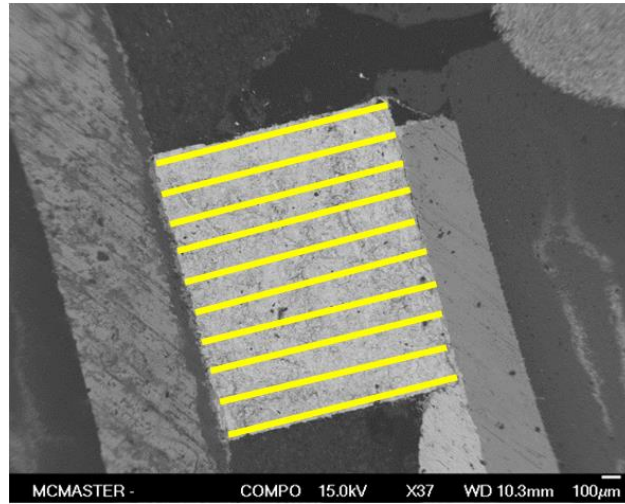
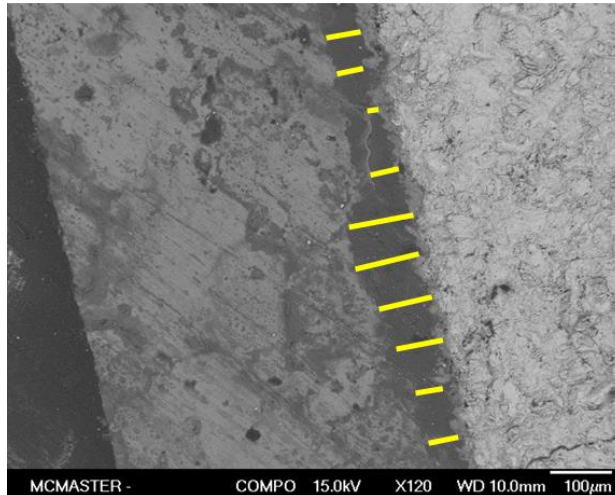


Figure 40: SEM image of a TEG thermocouple. Compositional information determined by EDS.

The dimensions of each structure were taken from an average of 10 measurements on the SEM image using *ImageJ* digitization software. Examples of this analysis are shown in Figure 40.



(a)



(b)

Figure 41: Recreation of dimensional measurement process using *ImageJ*. Each yellow line is manually drawn by the user and its length is compared to the scale given in the image. Sample photographs are of a (a) p-type leg and (b) the Al contact layer.

These measurements were accompanied by some assumptions. First, the final length of the p-type and n-type elements was calculated from the

average value obtained between both components. The same practice was implemented for the lateral width of each element. These dimensions are labelled in Figure 42 and their relationships are described by equations (4.5) to (4.6).

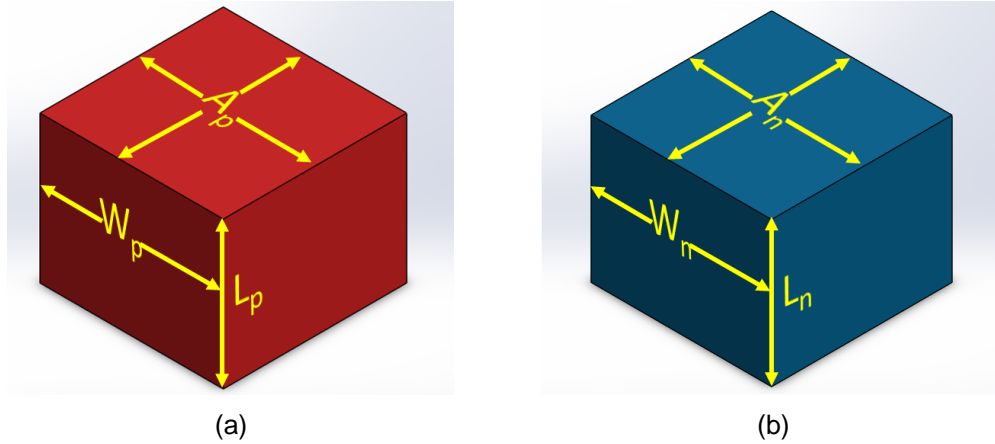


Figure 42: Length, width and cross-sectional area designations for (a) p-type element and (b) n-type element.

$$L = \frac{L_p + L_n}{2} \quad (4.5)$$

$$W = \frac{W_p + W_n}{2} \quad (4.6)$$

The cross-sectional area perpendicular to heat flow was also averaged between the p and n-type legs, and was estimated as the square of the average lateral width, W . This is shown in equation (4.7).

$$A = A_p = A_n = W^2 \quad (4.7)$$

This averaging process between both legs of the thermocouple continued for each of their constituent layers shown originally in Figure 40. All of the measurements can be found in Appendix I. After the dimensions were finalized, the thermocouple geometry was recreated in SolidWorks and

imported into ANSYS for analysis. Figure 43 shows the CAD assembly of the thermocouple. The dimensions of the top and bottom Al_2O_3 layers as well as the bottom electrical contacts were adjusted to allow the thermocouple to act as a unit cell belonging to the TEG module. This implies that the contents of the unit cell are scalable by the number of thermocouples present in the module, allowing the effects of all thermal and electrical losses to be proportionally represented. The idea to model a single thermocouple rather than the entire TEG was suggested by Ziolkowski *et al.* in [28] due to the increased simulation time required to evaluate a TEG module. The theoretical representation of a TEG assembled entirely out of unit cells is shown in Figure 44.

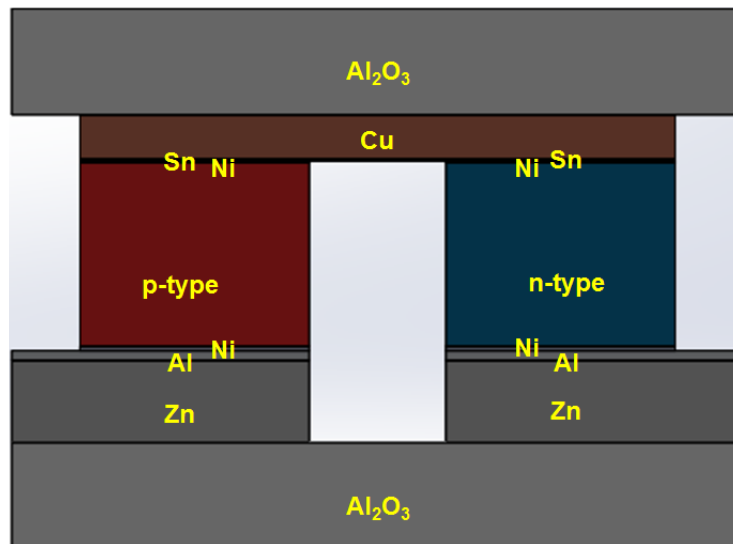


Figure 43: SolidWorks assembly of TEG Unit Cell with material designations for each layer.

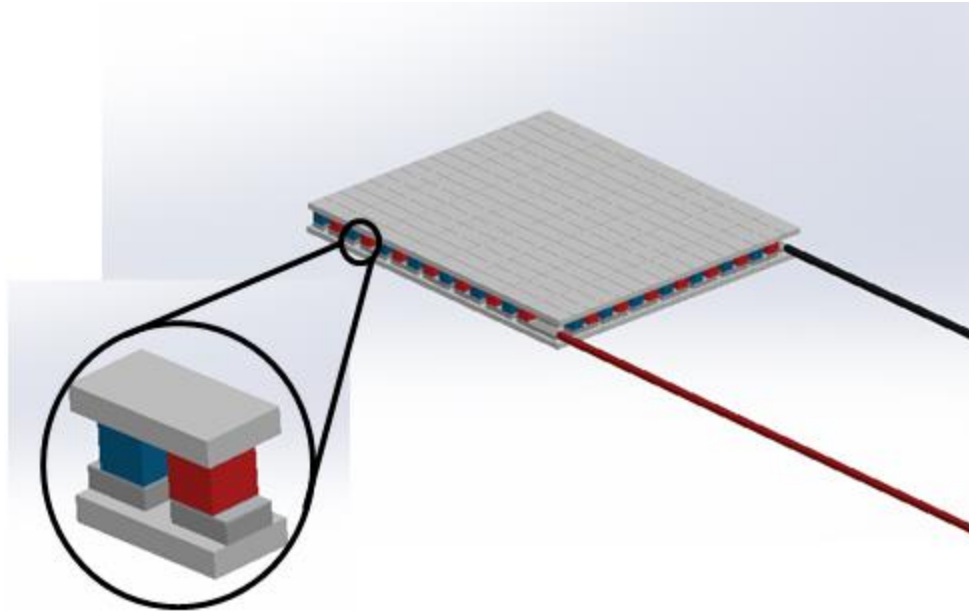
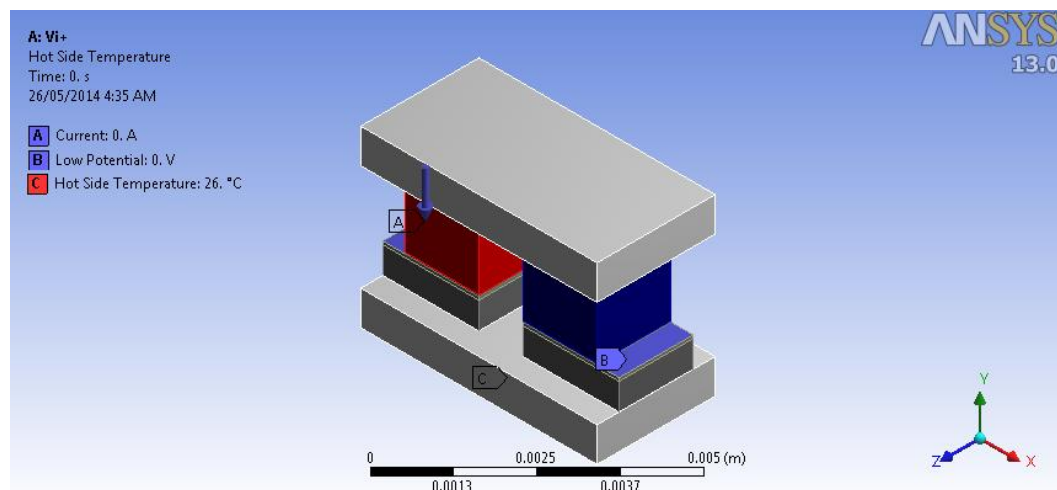


Figure 44: Theoretical depiction of TEG module comprised of unit cells.

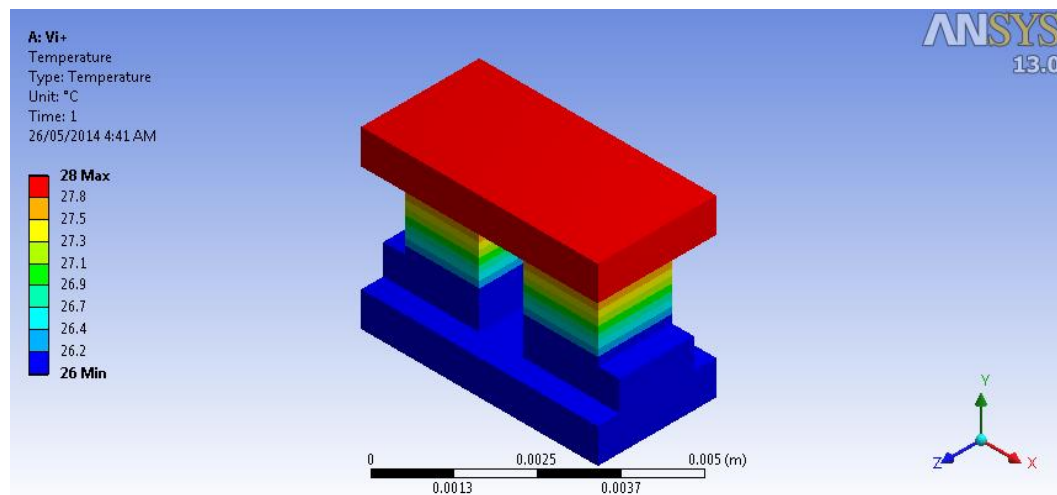
Thermal and electrical properties of the metallic and ceramic layers were taken from literature and are given in Appendix J. Through an iterative process, these properties were particularly useful in determining the amount of voltage dropped across the contacts during the test. This voltage was first calculated analytically, then after an iteration of the model with the known resistivities for the contacts in place, a more accurate value for this voltage drop was determined. This value was then reused in the calculation of the corrected experimental TEG material properties as per equation (3.37) until a convergence in the model was observed. After V_C was explicitly understood, the properties for the n-type and p-type materials were applied from experimental results of a TEG module and averaged for the couple. These are given in section 5.1.1. These averages represent the pairing of p-type and n-type materials with similar thermoelectric properties that are necessary to maintain a uniform

temperature difference and linearized electrical output from a given module.

With the material information and geometry in place, the final step in the simulation process was to apply electrical and thermal boundary conditions to the thermocouple surfaces. Images of these conditions are shown in the following two figures for the forward and reverse bias cases.

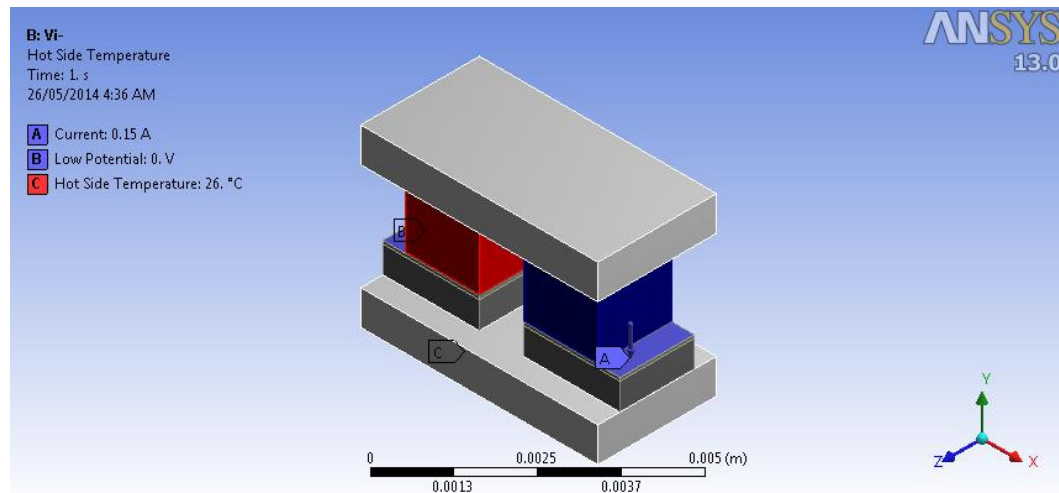


(a)

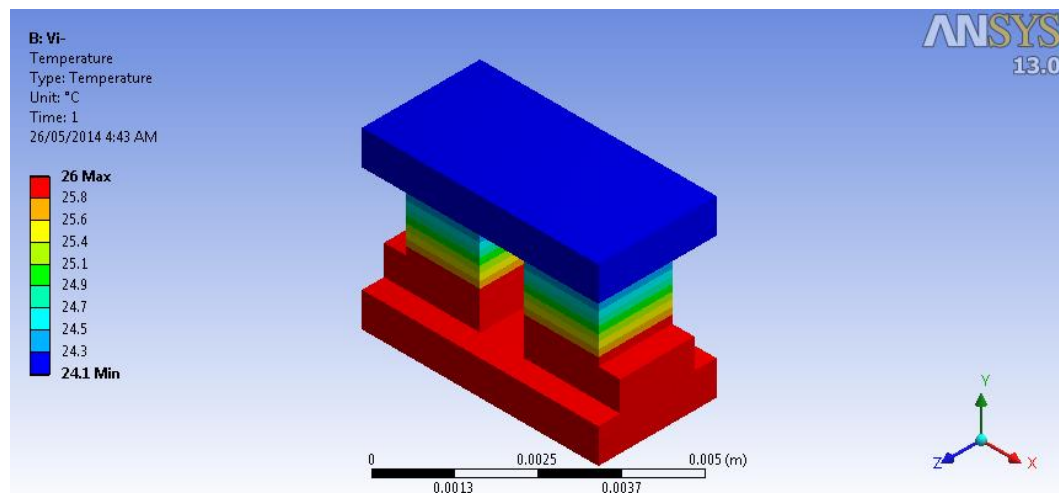


(b)

Figure 45: (a) Forward bias electrical and thermal boundary conditions. (b) Thermal response to applied current.



(a)



(b)

Figure 46: (a) Reverse bias electrical and thermal boundary conditions. (b) Thermal response to applied current.

Figure 45 and Figure 46 depict the steady-state thermoelectric voltage simulation, V_i for both current polarizations at room temperature. The location of the hot side temperature is fixed in both simulations while the electrical input conditions are switched between the two. The temperature profile is subsequently reversed due to the change in the current direction. All surfaces also contain radiation boundary conditions

which were not shown in the above figures due to space restrictions. These, along with the resistive voltage simulations, were repeated at different hot side temperatures up to 200°C to correspond with the measured data in section 5.1.2.

The V_{r+} and V_{r-} setups are physically identical to those in Figure 45(a) and Figure 46(a) as well. However the Seebeck coefficient of the thermoelectric materials suppressed to give a completely resistive voltage output without a changing temperature profile.

4.2 Parallel Thermal Conductance Model

The Thermal-Electric modelling environment was again used to simulate the PTC testing and develop a proof of principle. As with the Harman simulations, a SolidWorks assembly of the test system was imported into ANSYS and each component was given material parameters from Appendix E. Two simulations were run in accordance with the description of the technique given in section 3.1.2; one without the sample and one with the sample. The assembly is shown in Figure 47.

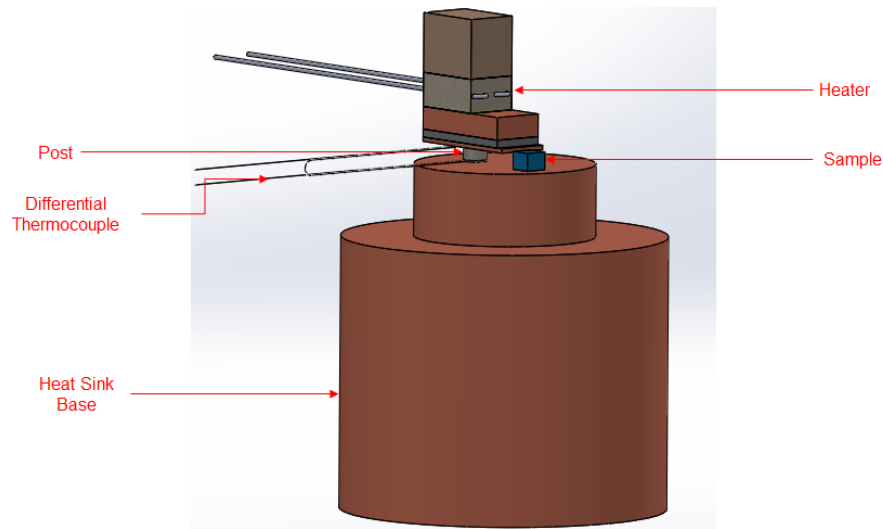
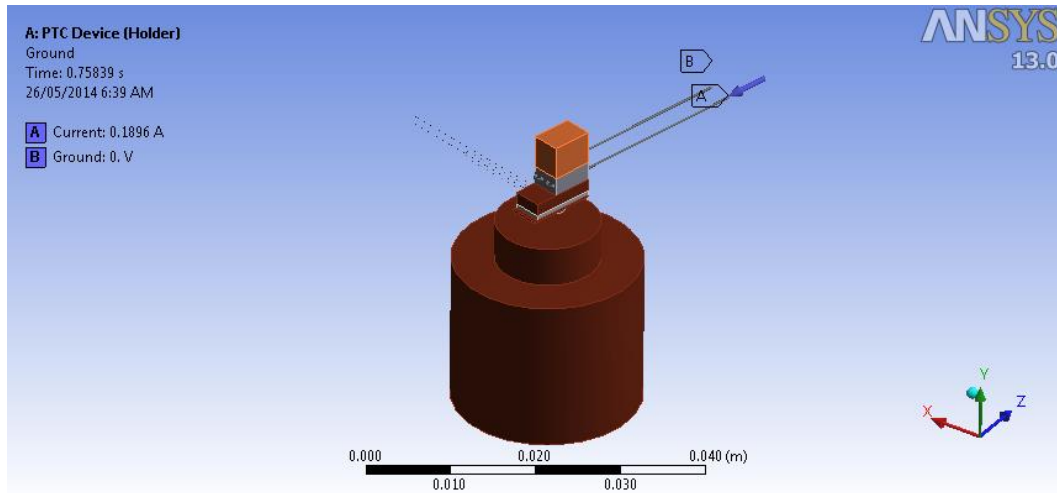
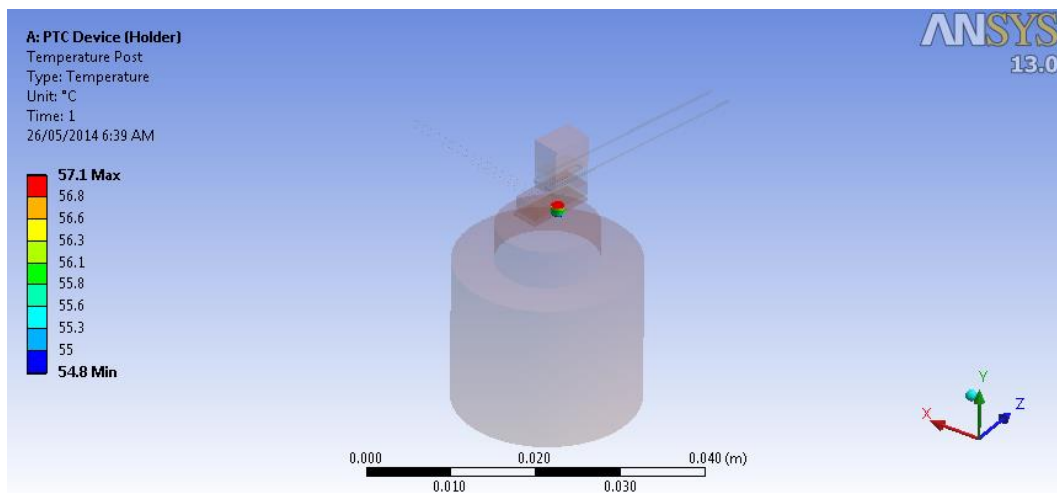


Figure 47: SolidWorks assembly of PTC system with sample attached.

As discussed previously in equation (3.41), the terms of interest are \dot{Q}_{in} , \dot{Q}_{rad_H} , and $\dot{Q}_{rad_{H+S}}$. These are the heater input power and the radiated powers of the holder alone and of the holder with the sample attached, respectively. The radiative heat terms are the only losses associated with the system and can be circumvented using the same radiation shield used in the Harman test apparatus. The simulation setup and resultant temperature difference in each scenario is shown in the following two figures as well. Radiation boundary conditions were again applied to all surfaces but are not shown.



(a)



(b)

Figure 48: (a) Heater input for PTC holder simulation. (b) Generated temperature difference across the post from heater to heat sink.

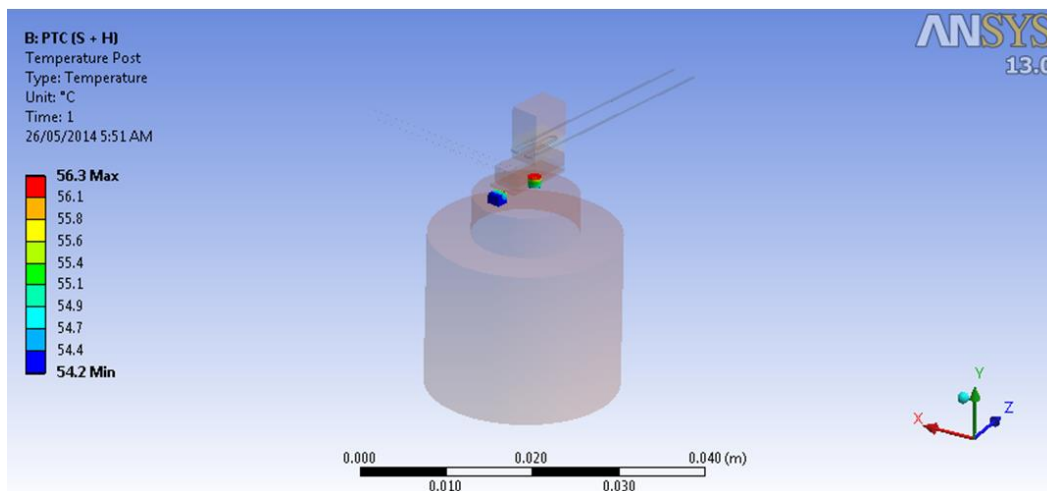
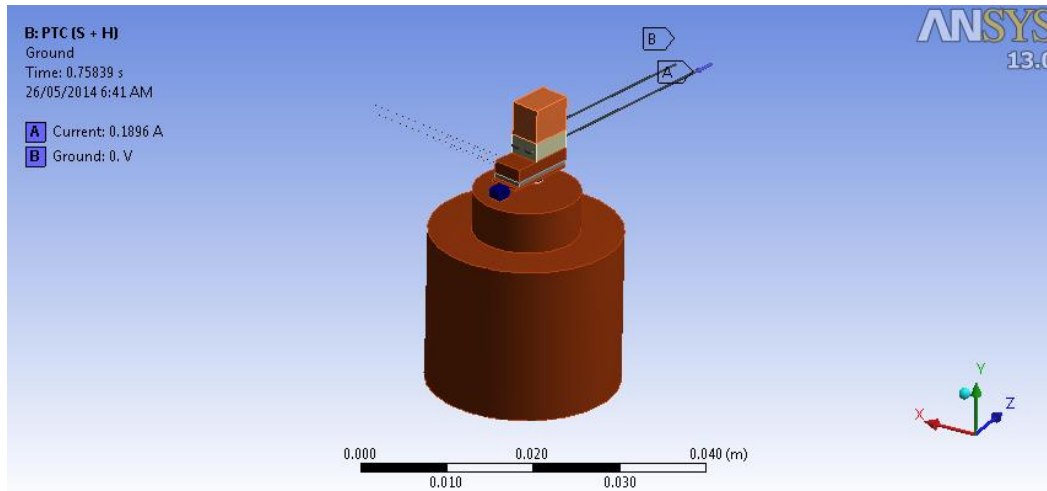


Figure 49: (a) Heater input for PTC holder + sample simulation. (b) Generated temperature difference across the post and the sample.

The PTC simulation is meant to act as a proof-of-principle to verify that the test can be adapted to temperatures significantly above room temperature.

5. Test Results

5.1 Harman Technique

The following are results for a TEG module that was applied a hot side temperature of up to 200°C.

5.1.1 Module Testing

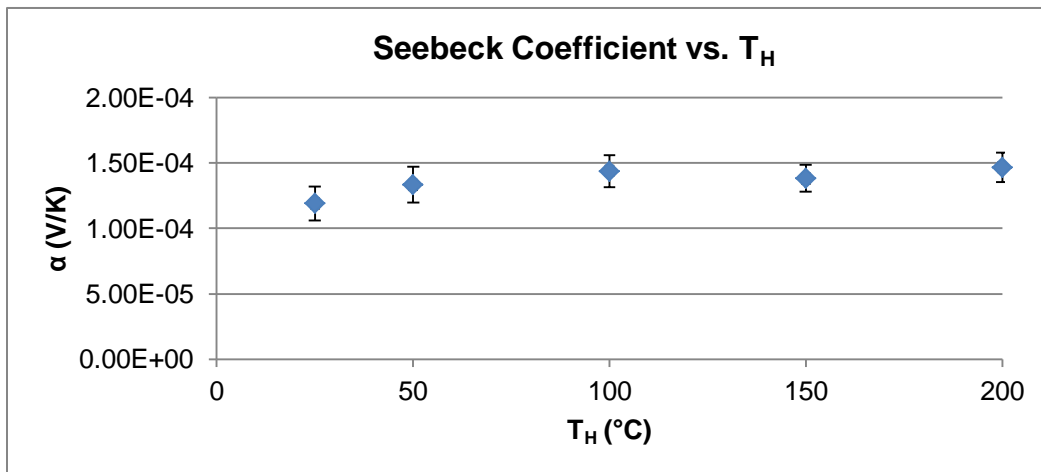


Figure 50: Seebeck coefficient as a function of temperature.

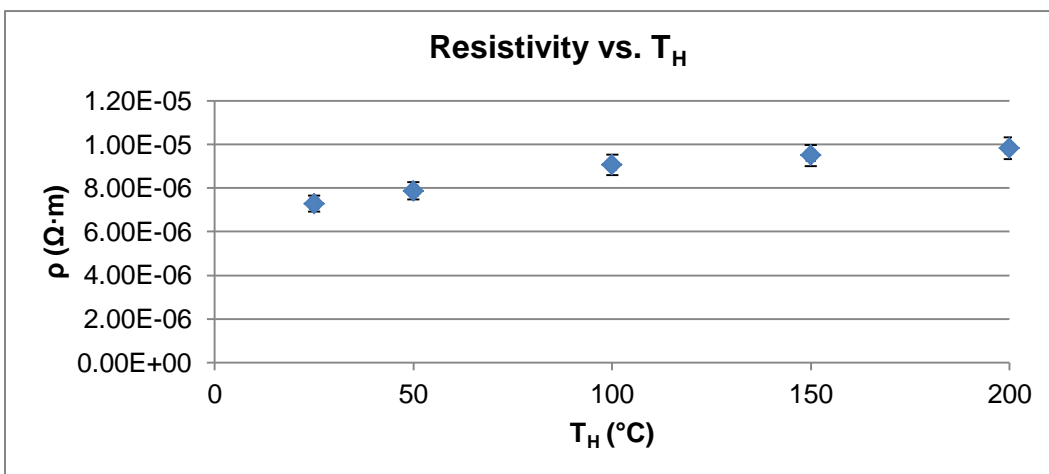


Figure 51: Electrical resistivity as a function of temperature.

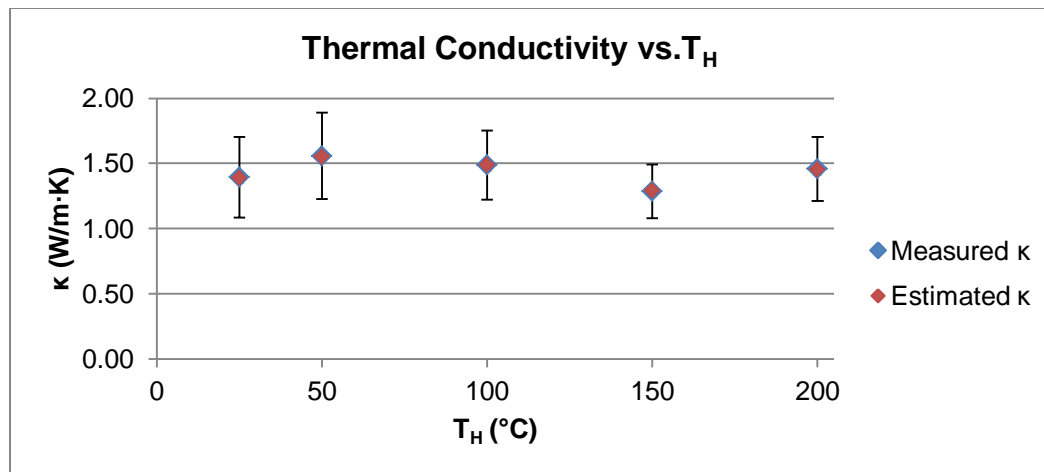


Figure 52: Measured thermal conductivity and estimated thermal conductivity using C_L as a function of temperature.

The values given for α , ρ and κ given above are given within the calculated uncertainty of the test system. The uncertainty in the thermal conductivity was the greatest because it was heavily influenced by the T^4 component of the radiation calculations.

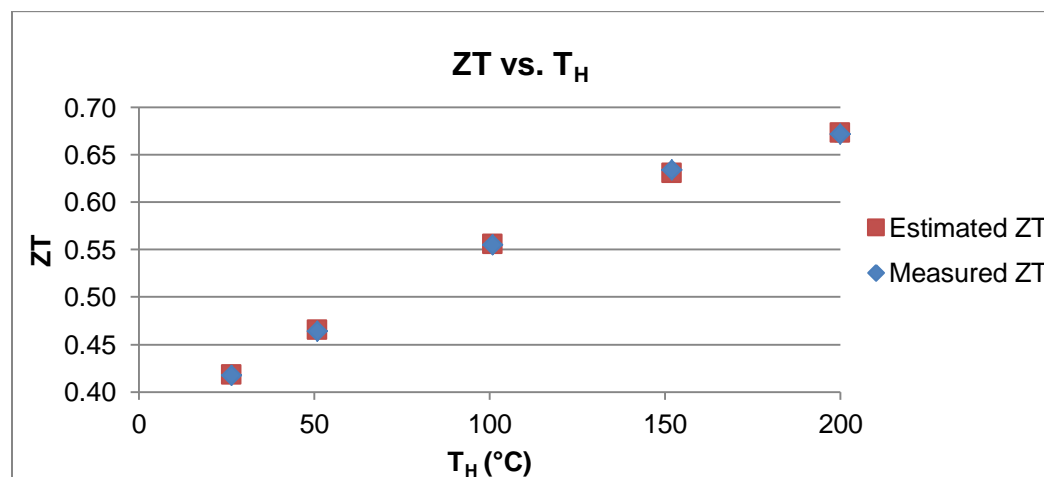


Figure 53: Measured ZT and Estimated ZT using C_L as a function of temperature.

The measured κ and ZT values given in the previous two figures are also contained within the uncertainty of the system, and are compared

with their estimated values using the C_L function approximation from equation (3.31). The difference between the measured and estimated values at each data point is less than one percent.

5.1.2 Comparison to Model

Modelling allowed for the analysis of the effects of the thermal and electrical losses defined in section 3.5.1. A graph of the measured ZT as a function of temperature is presented below, overlaid with results that consider no losses, only thermal losses, only electrical losses, and finally both electrical and thermal losses combined.

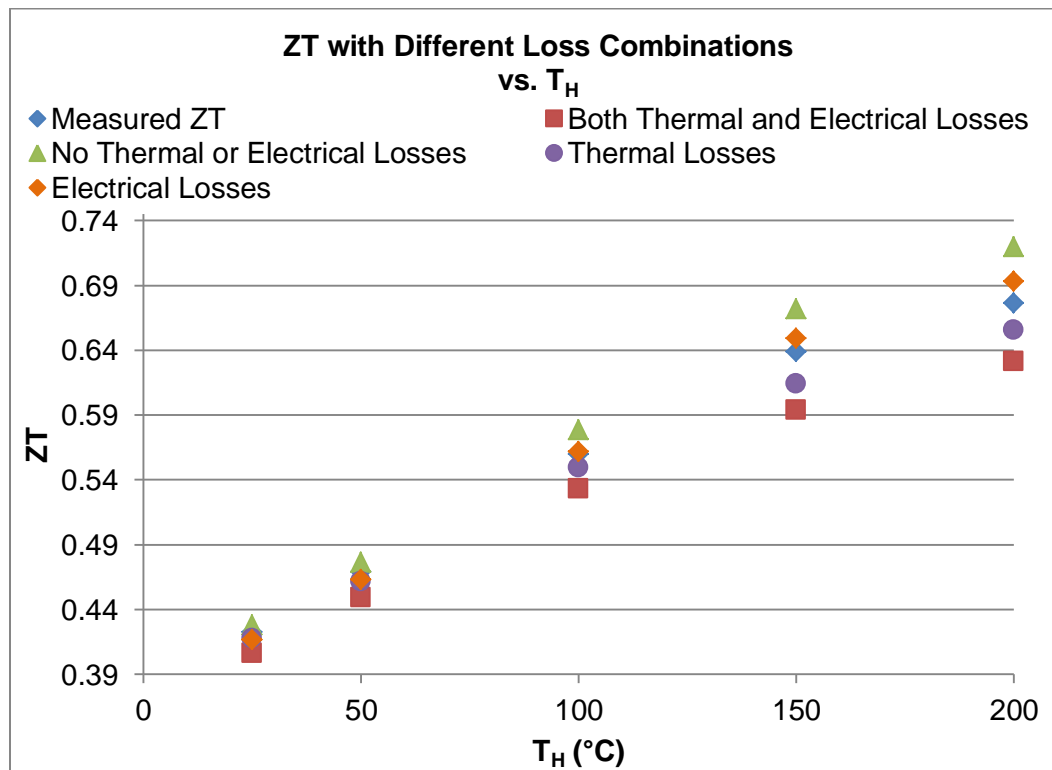


Figure 54: The effects of ignoring thermal and electrical losses in ZT measurements.

The completely lossless data represented by the green markers in Figure 54 were obtained by suppressing all radiative boundary conditions

in the simulation as well as measuring the voltage drop across the metal contact layers. This voltage was then used in equation (4.2) and thus, both thermal and electrical losses were completely subtracted from the calculation of ZT. The data set labelled “Electrical Losses” also had suppressed thermal boundary conditions but did not consider the contact voltage loss. Conversely, the “Thermal Losses” data had these boundary conditions enabled but included the subtraction of V_c . Finally, the ZT data for the “Both Thermal and Electrical Losses” was obtained by ignoring the effects of both types of losses.

It is clear from Figure 54 that the thermal losses are dominant since the data points begin to spread as temperature increases. Both of the data sets that ignored the effects of radiation were lower than the measured values. Accounting for thermal but ignoring electrical losses due to the contact voltage improved the measured values by as much as 3%. However it was observed that up to a 6% deviation can occur in measured values if the combined effects from both losses are not considered. The difference between the compounded loss data and the lossless data yielded a maximum percentage difference of 12% at 200°C and is expected to only increase past this point.

5.2 PTC Simulation Results

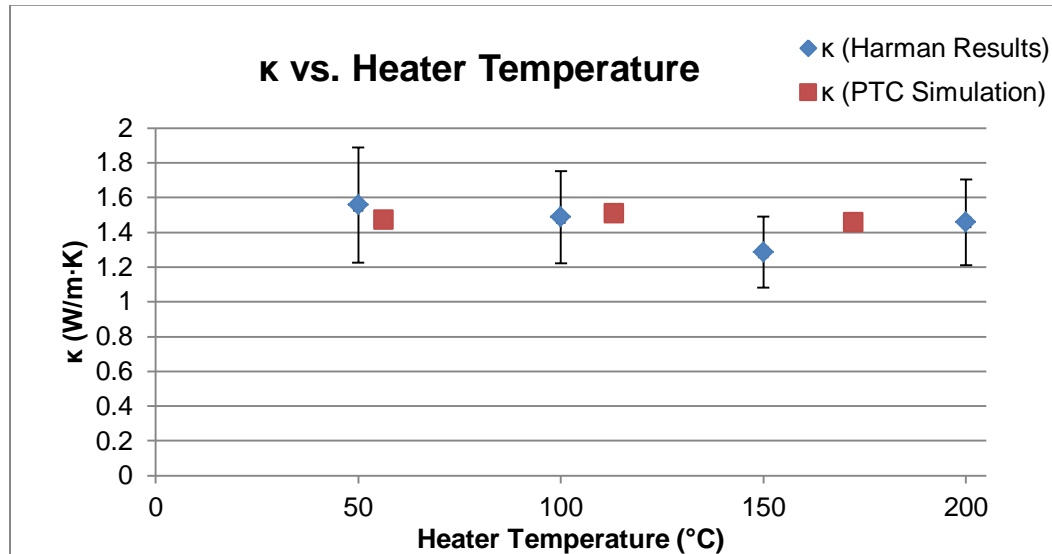


Figure 55: Thermal conductivity vs. heater temperature. The results simulated from the PTC technique are compared with the actual values obtained from the Harman Technique.

The sample used in the simulation had the dimensions of one of the elements from the thermocouple used in the Harman Technique simulation. These dimensions can again be found in Appendix I. The obtained values were compared to the measured values from Figure 52 and were observed to lay in between the data points. This is due to the different heater temperatures between the tests that are a function of input current.

Some additional considerations must be made in order to obtain the most accurate values for thermal conductivity. As previously mentioned, the samples to be used with this system will be extracted elements from commercial TEG modules with dimensions of roughly 1 mm^3 . The samples tested by Tritt *et al* had dimensions of $0.1 \times 0.05 \text{ mm}^2$ cross-sectional area and a height of 2.0 mm. Although these two samples have similar height

magnitudes, the ones tested in the literature have a larger height to area ratio that is more appropriate for the one dimensional heat flow assumption of the PTC system. Since the TEG elements are roughly as long as they are wide, the 1D approximation for their geometry needs to be augmented in one of two ways. The first method can be applied in the laboratory where the elements can be mechanically grinded down until they have an increased height to area ratio, thus mimicking the geometry used in the literature. The second method would be to reconstruct the ANSYS model such that the sample is placed directly under the heater as opposed to bonding it to the heater side surface with a small contact area. This model would simulate one dimensional heat flow through the entire sample at different test temperatures. The results from this simulation can be used to develop a relational coefficient for the experimental values that can compensate for the deviation in heat flow between the two systems.

6. Case Study: Binning Technique for Waste Heat Recovery System

The testing processes investigated in this thesis were commissioned for the research of materials and devices utilized in the Pizza Oven Waste Energy Recovery (POWER) System. This is a partnership project between McMaster University and Pizza Pizza. The system implements four rows of 10 to 12 TEGs each, which receive a T_H ranging from 200°C to 300°C and a T_C of 16°C to 20°C. These TEGs are mass-produced and vary significantly in performance within a given batch. This is due to poor quality control of the material growth and manufacturing techniques of the modules by the manufacturer. Therefore, the groups of TEGs purchased for use in the POWER System needed to be classified according to their overall performance, which led to the reinvestigation of the Harman Technique for binning purposes.

6.1 Description of Technique

A batch of TEGs was purchased and 40 of them were distributed among the four rows in the POWER System. During steady state operation, a constant hot side temperature of 260°C was maintained, with a cold side temperature of 16°C. The I-V curve of each TEG was measured in-situ using a BK Precision 8500 DC Load. The V_{OC} , I_{SC} and the maximum power point of the device were recorded. After acquiring these curves, the TEGs were removed from the oven and tested individually using the Harman technique at room temperature. This test was performed at 25°C and not at 260°C due to the amount of time taken for the system to reach thermal equilibrium. Room temperature testing

increased the throughput of this binning process and allowed for a batch of 60 TEGs to be tested in the span of about 20 hours.

When evaluating TEG performance for devices of the same model number, room temperature performance is sufficient to develop a relative rating scale since all of the TEGs are made with the same thermoelectric and contact materials. With this fact, deviations in quality between modules will arise in one of two ways:

- 1) Manufacturing defects due to poor contact surfaces and varying thermocouple geometry for both elements and electrical contacts.
- 2) Material growth inconsistencies due to varying dopant concentrations in the p and n-type materials used.

The first of these issues can be addressed by looking again at the equation for ZT which is given again below.

$$ZT = \frac{\alpha^2 T}{RK} \quad (6.1)$$

This represents the figure of merit for the module in terms of its bulk properties; the module Seebeck coefficient, resistance, and thermal conductance. The module resistance is equal to the sum of contributions from both the thermoelectric materials and the electrical contacts. Since the contacts are made of metals, their resistivity, and therefore resistance, increases linearly with temperature as per below [29]:

$$\rho_T = \rho_0[1 + \lambda(T - T_0)] \quad (6.2)$$

$$R_T = \frac{\rho_T L}{A} \quad (6.3)$$

The voltage drop across each contact reduces the total amount of available output from the module. When these contacts are made of variable size their contributions to the overall resistance will also vary from module to module at different temperatures based on their change in resistivity from equation (6.2). Also, poor contact formation may result in the creation of additional surfaces for radiation which will facilitate an increased radiation loss at higher temperatures. In regards to discrepancies in module performance due to different dopant concentrations, the effects of doping are given in Figure 13. The electrical power factor is maximized for a carrier concentration of about 10^{19} cm^{-3} . Material Seebeck coefficient and electrical conductivity will rise and fall, respectively, as the number of carriers increase. The electronic component of thermal conductivity, which accounts for up to 30% of the material thermal conductivity, will also rise in this case [30]. The electronic thermal conductivity and the electrical conductivity for thermoelectric materials are related via the Wiedemann-Franz law. This law is given below, where L is a coefficient known as the Lorenz number that varies with dopant concentration [11].

$$\kappa_e = \sigma LT \quad (6.4)$$

$$\kappa_e \rho = LT \quad (6.5)$$

The law given in equation (6.4) was rewritten in terms of electrical resistivity in (6.5). This relationship shows that with increasing temperature, the electrical resistivity and electronic thermal conductivity will increase linearly with temperature, also indicating that a room temperature binning method will suffice. Therefore TEGs that contain heavily doped materials should always underperform against those that

are lightly doped, due to the increase in resistivity and thermal conductivity, and their effects on ZT.

The entire batch of TEGs were ranked in descending order of ZT and rearranged back into the POWER system heat exchanger in a specific orientation. The thermal output to the hot side of the TEGs is parabolic with maximum heat flux occurring at the centre of a row. Therefore the TEGs with the highest ZTs were placed at opposite ends of a row in areas of reduced heat flow, and subsequently lower ranked units were placed in adjacent positions until the poorest performing TEG was placed directly in the centre. The lower the quality of the module, the greater the amount of heat it was to receive and vice-versa. This practice monopolized on the trade-off between available heat and performance of an individual TEG in an effort to linearize the maximum power output of each of the TEGs in a given row. As new groups of TEGs were purchased, they were instantly characterized using this technique and then placed accordingly into the POWER system.

6.2 Sample Results

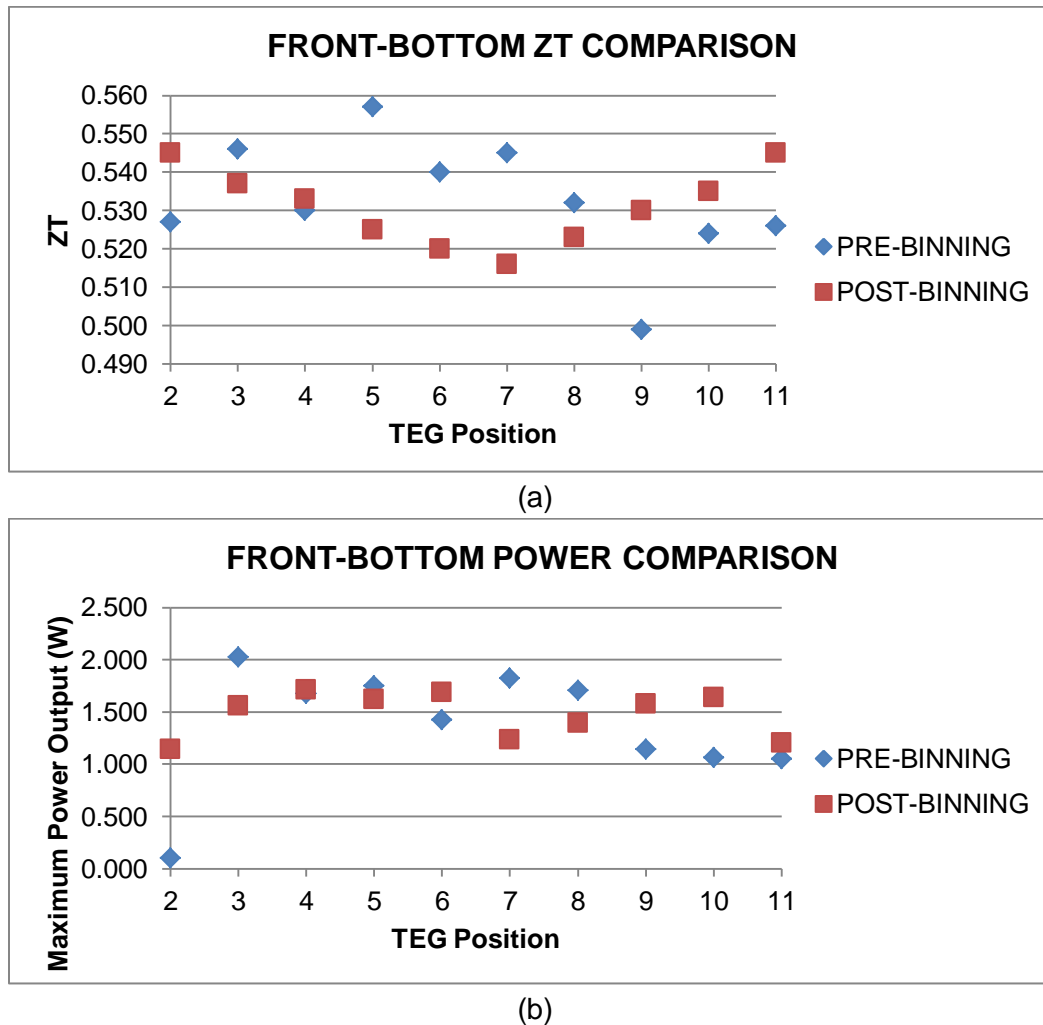


Figure 56: Comparison of (a) ZTs and (b) maximum power output measured for a row of TEGs before and after binning.

The POWER System has two heat rows on the front side of the exchanger, and two rows on the back. The results in Figure 56 correspond to the front-bottom row. The pre-binning results were due to the random placement of TEGs into the system without any selection criteria. The modules used post-binning were hand selected based on results from the Harman technique testing and were completely different units than those

used pre-binning. Figure 56(a) depicts the systematic positioning of TEGs based on their ZTs, and their associated power output after the binning process. Also, a more uniform maximum power output is observed in Figure 56(b)

6.3 System Efficiency Improvement

The V_{OC} , I_{SC} and maximum power point of each TEG were algebraically combined for use in series operation. The total I-V curve of the 40 TEG configuration is given in Figure 57.

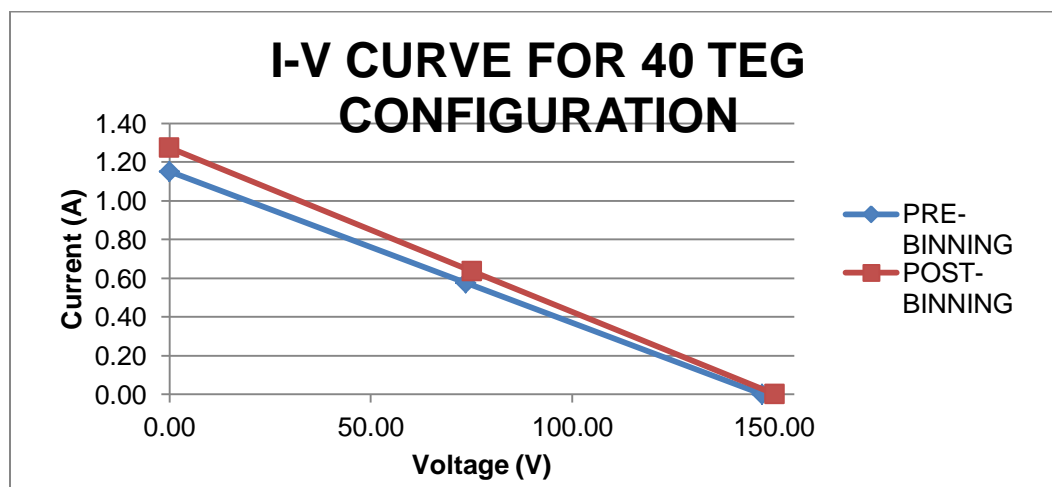


Figure 57: Pre-binning and Post-binning I-V curves for the total output of 40 TEGs.

The maximum power output before implementing the binning process was 42.3W and after binning it was 47.9W. Therefore using the same thermal inputs to the TEGs, an efficiency increase of 13.2% was observed in the electrical output.

7. Conclusion

The research conducted within this thesis was an integral part of the POWER project from Pizza Pizza and assisted in the foundation of a commercial TEG characterization system at McMaster University. The presented test system has been proven to extract the Seebeck coefficient, electrical resistivity and thermal conductivity from thermoelectric materials contained in TEG modules. The combination of these three parameters as per equation (2.18) yields the normalized figure of merit at a given operating temperature which indicates how well the material can convert heat into electricity.

The Harman technique was the primary test method used to obtain ZT and its associated quantities for commercially available TEGs from 25 to 200°C. It was selected for its short test time and its ability to yield ZT directly with only a few simple voltage measurements. This technique was also used as a means of quality assurance to effectively bin groups of TEGs in a minimal time frame for use within the POWER system. This rapid procedure increased the efficiency of the energy recovery by 13.2% and can be used on a larger scale to maximize the output of future installations of the system.

The generalized quantification of losses for a given model of TEG was a vital component of this thesis. This practice was applied to the TEG1B-12610-5.1. The ability to determine these losses for a single TEG model can be replicated for other models by following the two phase test methodology outlined here. This test system allows TEG manufacturers as well as design engineers to gather model-specific loss information quickly.

The thermal losses were evidently more detrimental than the electrical losses. The loss factor C_L , which is composed of all of the

radiative losses as well as other measurable quantities, is tedious to calculate depending on the geometry of the sample. For single TEG elements under test the radiation calculation would be much more simplified than for an entire TEG that requires an abundance of view factors between all possible surfaces within the module. After its initial calculation, the estimation of C_L as a function in the form of (3.31) yielded a faster and simpler way to determine the effects of thermal losses. The difference between the measured and estimated values of κ and ZT at each data point is less than one percent indicating that the thermal loss factor can be approximated to an acceptable level without explicitly calculating it each time. The determination of the electrical losses as linear functions of contact voltage or resistance also contributed to the complete loss profile of the TEG.

The simulation of a TEG unit cell in ANSYS proved to be useful in evaluating the independent and combined effects of the aforementioned losses. The experimental values obtained using the Harman technique for α , ρ and κ for the TEG elements were combined with the intermediate materials in the thermocouple using values from literature for their ρ and κ . The creation of the model necessitated the use of the following assumptions:

- i. The averaging process of the TEG geometry dimensions.
- ii. The neglecting of anisotropic effects in the thermal and electrical properties of the TEG material during the extrapolation of the thermocouple output to module output.
- iii. The p-type Seebeck coefficient, electrical resistivity and thermal conductivity were assumed to be equal to those of the n-type.
- iv. Emissivities were selected as single values over the entire operating temperature range.

Regardless of these assumptions, the model performed as expected yielding V_{ia} and V_{ra} voltage outputs for the thermocouple that were directly proportionate to those experimentally obtained from the module.

The end result of this testing proved that there were significant inconsistencies in the entire commercial TEG production process, from the growth of the thermoelectric materials to the manufacturing of the modules. At the operating temperature of 200°C the ZT was measured to be 0.67 ± 0.01 , a number less than the industrial standard for a “good thermoelectric” which, as previously mentioned, is unity. Now that the current status of commercial module quality can be evaluated, a claim can be made for new growth methods and TEG geometries to be investigated in the future that can outperform those presently in production.

7.1 Future Work

With an infrastructure for thermoelectric materials characterization fully established, a move towards next generation TEG development will be pursued. Investigation of new growth and manufacturing methods will produce materials that need to be classified according to their ZT and associated parameters. These methods will include pressing and sintering as well as 3D printing. The materials produced will be assembled into thermocouples of varying sizes and shapes that use different bonding materials to hold them together depending on their operating temperature requirements.

The Phase 1 testing process can diagnose crystalline quality of the thermoelectric materials as well verify the layer thicknesses of the intermediate metals used to create the ohmic junctions within thermocouples. The dimensional data can be obtained and used in Phase 2 for the finite element modelling and quantification of thermal and

electrical losses. At this point the Harman and PTC test systems will be used to gather α , ρ and κ from these new materials.

The Harman technique system has so far only been used to test TEG modules but will be adapted to test individual materials by changing the method of heat delivery to the sample. A thermoelectric material sample can be soldered to a sacrificial copper base and thermally bonded to an existing heater. Also heaters of any size can be created with an accompanying radiation guard to match as per the procedure outlined in section 3.4.2.2. The PTC apparatus has been constructed and modelled and will be used to assist in the verification of the results of the Harman technique system for small samples.

Finally, the binning procedure enabled by the use of the Harman technique can be used on a larger scale to test all potential TEG modules that will be used in every POWER system and rank them accordingly before their installation at a work site.

8. References

- [1] “Estimated U.S. Energy Use in 2011.” Lawrence Livermore National Laboratory., Oct-2012.
- [2] T. J. Seebeck, *Ueber die Magnetische Polarisation der Metalle und Erze durch Temperatur-Differenz*. Königlichten Akademie der Wissenschaften, 1825.
- [3] D. M. Rowe, *Thermoelectrics Handbook: Macro to Nano*. CRC Press, 2010.
- [4] M. F. Silva, J. F. Ribeiro, J. P. Carmo, L. M. Gonçalves, and J. H. Correia, “Thin Films for Thermoelectric Applications,” in *Scanning Probe Microscopy in Nanoscience and Nanotechnology 3*, B. Bhushan, Ed. Springer Berlin Heidelberg, 2013, pp. 485–528.
- [5] Callister, *Materials Science And Engineering: An Introduction, 6Th Ed (W/Cd)*. Wiley India Pvt. Limited, 2009.
- [6] B. G. Streetman and S. K. Banerjee, *Solid State Electronic Devices*. Pearson/Prentice Hall, 2010.
- [7] C. Kittel, *Introduction to solid state physics /*, 8th ed. J. Wiley, 2005.
- [8] S. Kasap, *Principles of Electronic Materials and Devices*. McGraw-Hill Education, 2005.
- [9] L. M. Gonçalves, “Microsistema termoelectrico baseado em teluretos de bismuto e antimônio,” Jul. 2008.
- [10] M. Lundstrom, “Thermoelectric Transport Parameters: Lectures 2.1 - 2.5,” in *Thermoelectrics: From Atoms to Systems*, Purdue University: nanoHUB-U, 2013.
- [11] G. J. Snyder and E. S. Toberer, “Complex thermoelectric materials,” *Nat. Mater.*, vol. 7, no. 2, pp. 105–114, Feb. 2008.
- [12] H. J. Goldsmid, *Introduction to Thermoelectricity*. Springer, 2009.

- [13] D. Finnerty, “The Development of Methodologies and a Novel Test Facility for the Characterisation of Thermoelectric Generators,” *McMaster Univ.*, May 2013.
- [14] T. C. Harman, “Special Techniques for Measurement of Thermoelectric Properties,” *J. Appl. Phys.*, vol. 29, no. 9, pp. 1373–1374, Jun. 2004.
- [15] R. J. Buist, “A New Method for Testing Thermoelectric Materials and Devices,” presented at the 11th International Conference on Thermoelectrics, Arlington, Texas, USA, 1992.
- [16] R. McCarty, J. Thompson, J. Sharp, A. Thompson, and J. Bierschenk, “Methodology for Minimizing Losses for the Harman Technique at High Temperatures,” *J. Electron. Mater.*, vol. 41, no. 6, pp. 1274–1279, Jun. 2012.
- [17] B. M. Zawilski, R. T. L. Iv, and T. M. Tritt, “Description of the parallel thermal conductance technique for the measurement of the thermal conductivity of small diameter samples,” *Rev. Sci. Instrum.*, vol. 72, no. 3, pp. 1770–1774, Mar. 2001.
- [18] National Instruments, “NI USB-621x User Manual.” Apr-2009.
- [19] Thor Labs Inc., “TH100PT - 100 Ohm Resistive Temperature Sensor.” .
- [20] W. Bacharowski, “A Precision Interface for a Resistance Temperature Sensor (RTD).” Texas Instruments, 2011.
- [21] W. Boyes, *Instrumentation Reference Book*. Butterworth-Heinemann, 2002.
- [22] “ITS-90 Table for Type T Thermocouple.” National Institute of Standards and Technology, 29-Dec-1999.
- [23] MG Chemicals, “Silicone Heat Transfer Compound 860.” .
- [24] G. Nellis and S. Klein, *Heat Transfer*. Cambridge University Press, 2009.

- [25] U. Gross, K. Spindler, and E. Hahne, "Shapefactor-equations for radiation heat transfer between plane rectangular surfaces of arbitrary position and size with parallel boundaries," *Lett. Heat Mass Transf.*, vol. 8, no. 3, pp. 219–227, May 1981.
- [26] S. Fujimoto, H. Kaibe, S. Sano, and T. Kajitani, "Development of Transient Measurement Method for investigating Thermoelectric Properties in High Temperature Region," *Jpn. J. Appl. Phys.*, vol. 45, no. 11R, p. 8805, Nov. 2006.
- [27] H. S. Lee, "ANSYS Thermoelectric Generator (TEG) Tutorial." ME 5390 Course Notes. Department of Mechanical Engineering, West Michigan University, 2010.
- [28] P. Ziolkowski, P. Poinas, J. Leszczynski, G. Karpinski, and E. Müller, "Estimation of Thermoelectric Generator Performance by Finite Element Modeling," *J. Electron. Mater.*, vol. 39, no. 9, pp. 1934–1943, Sep. 2010.
- [29] D. C. Giancoli, *Physics for Scientists and Engineers with Modern Physics*. Pearson Education, 2008.
- [30] I. Terasaki, "1.09 - Thermal Conductivity and Thermoelectric Power of Semiconductors," in *Comprehensive Semiconductor Science and Technology*, P. B. F. Kamimura, Ed. Amsterdam: Elsevier, 2011, pp. 326–358.
- [31] J. R. Taylor, *An Introduction to Error Analysis: The Study of Uncertainties in Physical Measurements*. University Science Books, 1997.
- [32] T. Hayden and J. Roop, "RTD Instrumentation Requirements." Keithley Instruments Inc.
- [33] H. S. Lee, *Thermal Design: Heat Sinks, Thermoelectrics, Heat Pipes, Compact Heat Exchangers, and Solar Cells*. Wiley, 2010.
- [34] "Ceramics, Refractories, and Glasses," in *Materials Handbook*, Springer London, 2008, pp. 593–689.

- [35] A. J. Slifka, B. J. Filla, and J. M. Phelps, "Thermal conductivity of magnesium oxide from absolute, steady-state measurements," *J. Res. Natl. Inst. Stand. Technol.*, vol. 103, no. 4, p. 357, Jul. 1998.
- [36] Omega, "OMEGABOND High Temperature Chemical Set Cements." 2013.
- [37] Y. S. Touloukian and D. P. DeWitt, "Thermophysical Properties of Matter - the Tprc Data Series. Volume 7. Thermal Radiative Properties - Metallic Elements and Alloys. (reannouncement). Data Book," Purdue Univ., Lafayette, IN (United States). Thermophysical and Electronic Properties Information Center, AD-A-951941/4/XAB, Jan. 1970.
- [38] Y. A. Çengel and J. M. Cimbala, *Fundamentals of Thermal-fluid Sciences*. McGraw-Hill Higher Education, 2012.
- [39] D. R. Lide, *CRC Handbook of Chemistry and Physics, 85th Edition*. CRC Press, 2004.
- [40] MatWeb, "Physical Properties of Sn." MatWeb Material Property Data.(<http://www.matweb.com/search/datasheet.aspx?matguid=64d7cf04332e428dbca9f755f4624a6c&ckck=1>).

APPENDIX A: Measurement Uncertainty

Sample calculations for the uncertainty of all measured quantities at the 200°C data point from the Harman technique results will be provided below. Error propagation was used to calculate the uncertainty in α , ρ , κ , ZT once the error in each of the associated values was determined.

The general formula for error propagation is given below for a function $f(x_1, x_2, \dots x_n)$ consisting of two or more variables [31].

$$\delta f = \sqrt{\sum_{i=1}^n \left(\frac{df}{dx_i} \right)^2 \delta x_i^2} \quad (\text{A.1})$$

The uncertainty in the function f is denoted by δf and the uncertainty of each variable x_i that exists within that function is given by δx_i .

Voltage Uncertainty

All voltage measurements were done using the National Instruments USB-6211 DAQ. Harman technique test voltages were measured using the 1V range and the voltages read from the RTD and differential thermocouple were under the 0.2V range. The number of samples taken within a single loop iteration of the code is 8333. The Absolute Accuracy Table in the DAQ manual found in [18] was reproduced below to determine the error of measured values within these ranges. The calculation of accuracy as defined in the manual is also recreated and follows the table as well.

Range	Residual Gain Error (ppm of Reading)	Gain Tempco (ppm/°C)	Reference Tempco	Residual Offset Error (ppm of Range)	Offset Tempco (ppm of Range/°C)	INLError (ppm of Range)	Random Noise, σ (μ Vrms)	Sensitivity (μ V)
± 0.2 V	135	7.3	5	40	116	76	12	4.8
± 1 V	95	7.3	5	25	49	76	26	10.4

Analog Input Accuracy Table for USB DAQ 6211

AbsoluteAccuracy=Reading(GainError) + Range(OffsetError) + NoiseUncertainty

GainError=ResidualGainError + GainTempco(TempChangeFromLastInternalCal)
+ ReferenceTempco(TempChangeFromLastExternalCal)

OffsetError=ResidualOffsetError + OffsetTempco ·
(TempChangeFromLastInternalCal) + INL_Error

$$\text{NoiseUncertainty}^* = \frac{\text{RandomNoise} \cdot 2}{\sqrt{8333}}$$

**For a coverage factor of 2σ and averaged over 8333 data points*

Suggested Assumptions:

TempChangeFromLastExternalCal = 10 °C

TempChangeFromLastInternalCal = 1°C

Number_of_Readings = 8333 (from current use in Harman and PTC code only)

Sample Calculation:

Reading: $V_{o+} = 0.144$ V

This is a data point for the forward bias Seebeck voltage @ 200°C from Harman Technique. It is read in the ± 0.2 V range.

GainError = 135ppm + 7.3ppm(1) + 5ppm(10) = 192ppm

OffsetError = 40ppm + 116ppm(1) + 76ppm = 232ppm

$$\text{NoiseUncertainty} = \frac{12\mu V \cdot 2}{\sqrt{8333}} = 0.26\mu V$$

$$\text{AbsoluteAccuracy} = 0.14V(\text{GainError}) + 0.2(\text{OffsetError}) + \text{NoiseUncertainty} = 75\mu V = 7.5 \cdot 10^{-5} V$$

$$\therefore V_{o+} = 0.144V \pm 7.44 \cdot 10^{-5}V$$

The remaining voltages at this data point and their uncertainties are provided in the table below.

Voltage	Reading (V)	δV (V)
V_{o+}	0.144	$\pm 7.44 \cdot 10^{-5}$
V_{o-}	0.078	$\pm 6.16 \cdot 10^{-5}$
V_{i+}	0.322	$\pm 2.00 \cdot 10^{-4}$
V_{i-}	0.294	$\pm 1.95 \cdot 10^{-4}$

Sample Harman test voltages @ 200°C with uncertainty.

The uncertainty in the average measurements is then calculated using the error propagation formula as exemplified below.

$$V_{oa} = \frac{V_{o+} + V_{o-}}{2} = \frac{0.144 + 0.078}{2} = 0.111 V$$

$$\begin{aligned} \delta V_{oa} &= \sqrt{\left(\frac{dV_{oa}}{dV_{o+}}\right)^2 \cdot \delta V_{o+}^2 + \left(\frac{dV_{oa}}{dV_{o-}}\right)^2 \cdot \delta V_{o-}^2} = \sqrt{\left(\frac{\delta V_{o+}^2}{4}\right) + \left(\frac{\delta V_{o-}^2}{4}\right)} \\ &= \sqrt{\frac{(7.44E-5)^2}{4} + \frac{(6.16E-5)^2}{4}} = \pm 4.83 \cdot 10^{-5} V \end{aligned}$$

Both V_{oa} and V_{ia} values at this test point with their uncertainties are tabulated in the table below.

Voltage	Reading (V)	δV (V)
V_{oa}	0.111	$\pm 4.83 \cdot 10^{-5}$
V_{ia}	0.308	$\pm 1.40 \cdot 10^{-4}$

Averaged sample Harman test voltages @ 200°C with uncertainty.

Current Uncertainty

The source of error for the applied test current was the BK Precision 9130 power supply. Its manual states a programming accuracy of $\leq 0.1\% + 5\text{mA}$ for current. The test current used was 0.150A with an uncertainty of $\pm 0.005\text{A}$

Temperature Uncertainty

The two temperature sensors used were an RTD and a differential thermocouple. The temperature measured by the RTD was governed by equation (3.15). The resistance in that equation was obtained from a series of voltage measurements using equations (3.15) and (3.16). These provided the voltage and current applied to the RTD and through Ohm's law, yielded the resistance. The principle for calculating the uncertainty in the RTD measurement apparatus due to the reading of these voltages is outlined in [32]. The RTDs were used to measure the top side temperatures during the Harman technique. These were T_C and T_H' . A sample calculation for the measurement of T_C at 146°C is given below. Voltages were measured with the DAQ using the 0.2V range measurement setting and its uncertainty was calculated as per the *Voltage Uncertainty* procedure described above.

$$\Delta V_{RTD} = 0.156 \pm 6.8 \cdot 10^{-5} \text{ V}$$

$$R_T = \frac{\Delta V_{RTD}}{0.001} = \frac{0.156}{0.001} = 156 \, \Omega$$

$$\delta R_T = \sqrt{\left(\frac{dR_T}{d\Delta V_{RTD}}\right)^2 \delta \Delta V_{RTD}^2} = \sqrt{\left(\frac{1}{0.001^2}\right) (6.85 \cdot 10^{-5})^2} = \pm 0.1 \, \Omega$$

$$\begin{aligned} T_C &= 3383.8095 - 0.0866 \cdot \sqrt{1.7585 \cdot 10^9 - 2.31 \cdot 10^6 \cdot R_T} \\ &= 3383.8095 - 0.0866 \cdot \sqrt{1.7585 \cdot 10^9 - 2.31 \cdot 10^6 \cdot (156)} \\ &= 146 \, ^\circ C \end{aligned}$$

$$\begin{aligned} \delta T_{C_{DAQ}} &= \sqrt{\left(\frac{dT_C}{dR_T}\right)^2 \delta R_T^2} = 1 \cdot 10^5 \sqrt{\frac{\delta R_T^2}{1.76E9 - 2.31E6 \cdot R_T}} \\ &= 1E5 \sqrt{\frac{(0.1)^2}{1.76 \cdot 10^9 - 2.31 \cdot 10^6 \cdot (156)}} = \pm 0.2 \, ^\circ C \end{aligned}$$

The RTD itself has an uncertainty of $\pm 0.1^\circ C$ that must be taken into account as well as the uncertainty caused by the DAQ measurement calculated above.

$$\therefore \delta T_C = \sqrt{\delta T_{C_{DAQ}}^2 + \delta T_{C_{RTD}}^2} = \sqrt{(0.2)^2 + (0.1)^2} = \pm 0.2 \, ^\circ C$$

The bottom temperatures, T_H and T_C' were measured using the differential thermal couple and were dependent on the measurement of T_C and T_H' in the following equations:

$$T_H = T_C + \Delta T$$

$$T_C' = T_H - \Delta T$$

ΔT is measured with the differential thermocouple according to equation (3.17) which is rewritten below.

$$\Delta T = \sum_{i=0}^6 c_i V^i$$

Coefficient	Value
C_0	0.000000
C_1	$2.592800 \cdot 10^{-2}$
C_2	$-7.602961 \cdot 10^{-7}$
C_3	$4.637791 \cdot 10^{-11}$
C_4	$-2.165394 \cdot 10^{-15}$
C_5	$6.048144 \cdot 10^{-20}$
C_6	$-7.293422 \cdot 10^{-25}$

Type T thermocouple polynomial coefficients valid for $T = 0$ to 400°C [22].

The voltage in the equation above read by the DAQ was equal to:

$$V = 2.208 \cdot 10^{-3} \pm (4.7 \cdot 10^{-5}) \text{ V}$$

The corresponding ΔT between T_H and T_C using equation (3.17) is:

$$\Delta T = \sum_{i=0}^6 c_i (2.208 \cdot 10^{-3})^i = 54^\circ\text{C}$$

$$\begin{aligned}
 \delta \Delta T_{DAQ} &= \sqrt{\left(\frac{d\Delta T}{dV}\right)^2 \delta V^2} \\
 &= ((0.025928 - 0.0000015205922 \cdot (2.208 \cdot 10^{-3}) \\
 &\quad + 1.3913373 \cdot 10^{-10} \cdot (2.208 \cdot 10^{-3})^2 - 8.661576 \cdot 10^{-15} \\
 &\quad \cdot (2.208 \cdot 10^{-3})^3 + 3.024072 \cdot 10^{-19} \cdot (2.208 \cdot 10^{-3})^4 \\
 &\quad - 4.3760532 \cdot 10^{-24} \cdot (2.208 \cdot 10^{-3})^5)^2 \cdot \delta V^2)^{\frac{1}{2}} \\
 &= ((0.025928 - 0.0000015205922 \cdot V + 1.3913373 \cdot 10^{-10} \cdot V^2 \\
 &\quad - 8.661576 \cdot 10^{-15} \cdot V^3 + 3.024072 \cdot 10^{-19} \cdot V^4 \\
 &\quad - 4.3760532 \cdot 10^{-24} \cdot V^5)^2 \cdot (4.7 \cdot 10^{-5})^2)^{\frac{1}{2}} \\
 &= \pm 1.2 \cdot 10^{-6} \text{ } ^\circ\text{C}
 \end{aligned}$$

The thermocouple also has an associated error which is $\pm 0.03^\circ\text{C}$.

$$\delta\Delta T = \sqrt{\delta\Delta T_{DAQ}^2 + \delta\Delta T_{TC}^2} = \sqrt{(1.2 \cdot 10^{-6})^2 + (0.03)^2} = \pm 0.03^\circ\text{C}$$

With T_C and ΔT determined, T_H and its uncertainty can now be calculated.

$$T_H = 146 + 54 = 200^\circ\text{C}$$

$$\delta T_H = \sqrt{\left(\frac{dT_H}{dT_C}\right)^2 \delta T_C^2 + \left(\frac{dT_H}{d\Delta T}\right)^2 \delta \Delta T^2} = \sqrt{(0.2)^2 + (0.03)^2} = \pm 0.2^\circ\text{C}$$

All temperatures measured at the 200°C data point are summarized below with their associated uncertainties as per the procedure outlined above.

Temperature	Reading ($^\circ\text{C}$)	Reading (K)	δT ($^\circ\text{C}$)/(K)
T_H	200.0	473.15	± 0.2
T_C	146.0	419.15	± 0.2
T_H'	150.0	423.15	± 0.2
T_C'	198.0	471.15	± 0.2

Sample temperatures measured during the Harman technique.

The average temperatures and the bipolar temperature difference were calculated in units of K, along with their uncertainties. The uncertainties in $^\circ\text{C}$ are equal to those in K due to the relationship of the unit magnitudes for each temperature scale.

$$T_a = \frac{T_H + T_C}{2} = \frac{(273.15 + 200) + (273.15 + 146)}{2} = 446.15 \text{ K}$$

$$\delta T_a = \sqrt{\frac{\delta T_H^2}{4} + \frac{\delta T_C^2}{4}} = \sqrt{\frac{0.2^2}{4} + \frac{0.2^2}{4}} = \pm 0.16 \text{ K}$$

$$\begin{aligned}
D_a &= (T_H - T_C) + (T'_H - T'_C) \\
&= ((273.15 + 200) - (273.15 + 146)) \\
&\quad + ((273.15 + 150) - (273.15 + 198)) = 6 \text{ K}
\end{aligned}$$

$$\delta D_a = \sqrt{\delta T_H^2 + \delta T_C^2 + \delta T_H'^2 + \delta T_C'^2} = \sqrt{0.2^2 + 0.2^2 + 0.2^2 + 0.2^2} = \pm 0.46 \text{ K}$$

Temperature	Value (K)	δT (°C)/(K)
T_a	446.15	± 0.16
T_a'	447.15	± 0.16
D_a	6.0	± 0.46

Dimensional Uncertainty

The dimensional data obtained by the SEM in Appendix I was taken in measurements of 10 and averaged. The uncertainty was calculated in Microsoft Excel using the sample standard deviation function. All of these uncertainties are tabulated in the aforementioned appendix.

The following is a sample calculation of the cross-sectional area of the TEG element.

$$W = 1.569E - 3 \text{ m}$$

$$\delta W = \pm 2.8E - 5 \text{ m}$$

$$A = W^2 = (1.569E - 3)^2 = 2.462E - 6 \text{ m}^2 = 2.462 \text{ mm}^2$$

$$\begin{aligned}
\delta A &= \sqrt{\left(\frac{dA}{dW}\right)^2 \delta W^2} = \sqrt{(2W)^2 \delta W^2} = \sqrt{(2 \cdot 1.569 \cdot 10^{-3})^2 (2.8 \cdot 10^{-5})^2} \\
&= \pm 8.786 \cdot 10^{-8} \text{ m}^2 = \pm 0.088 \text{ mm}^2
\end{aligned}$$

Radiative Loss Uncertainty

Recall equation (3.27):

$$\dot{Q}_{ij} = A_i F_{ij} \sigma_B (\epsilon_i T_i^4 - \epsilon_j T_j^4)$$

The net radiation loss corresponding to view factor (1) in Appendix H will be calculated. This is the radiation between a strip of Al_2O_3 and one face of the Bi_2Te_3 TEG element during the forward bias pulse of the Harman technique. The dimensions of W and W_{space} are found in Appendix I and the emissivities of Al_2O_3 (ϵ_1) and Bi_2Te_3 (ϵ_2) are found in Appendix J.

$$\begin{aligned} A_1 &= \text{Portional Area of } \text{Al}_2\text{O}_3 \\ &= (\text{element spacing}) \\ &\quad \cdot (0.5(\text{element spacing}) + 15(n - \text{type horizontal width}) \\ &\quad + 15(\text{element spacing})) \\ &= W_{\text{space}}(0.5W_{\text{space}} + 15W + 15W_{\text{space}}) \\ &= W_{\text{space}}(15.5W_{\text{space}} + 15W) \\ &= (9.35 \cdot 10^{-4})(15.5(9.35 \cdot 10^{-4}) + 15(1.569 \cdot 10^{-3})) \\ &= 3.56 \cdot 10^{-5} \text{ m}^2 \end{aligned}$$

$$\begin{aligned} \delta A_1 &= \sqrt{\left(\frac{dA_1}{dW}\right)^2 \delta W^2 + \left(\frac{dA_1}{dW_{\text{space}}}\right)^2 \delta W_{\text{space}}^2} \\ &= \sqrt{(15W_{\text{space}})^2 \delta W^2 + (31W_{\text{space}} + 15W)^2 \delta W_{\text{space}}^2} \\ &= \sqrt{(15(9.35 \cdot 10^{-4}))^2 (2.8 \cdot 10^{-5})^2 + (31(9.35 \cdot 10^{-4}) + 15(1.569 \cdot 10^{-3}))^2 (3.4 \cdot 10^{-5})^2} \end{aligned}$$

$$= \pm 1.79 \cdot 10^{-6} \text{ m}^2$$

$$T_1 = T_H = 473.15 \pm 0.2 \text{ K}$$

$$T_2 = T_C = 419.15 \pm 0.2 \text{ K}$$

$$\varepsilon_1 = 0.6 = \varepsilon_2$$

$$F_{12} = 0.01$$

$$\sigma_B = 5.6704 \cdot 10^{-8} \text{ W} \cdot \text{m}^2 \cdot \text{K}^{-4}$$

$$\begin{aligned} \dot{Q}_{12} &= A_1 F_{12} \sigma_B (\varepsilon_1 T_1^4 - \varepsilon_2 T_2^4) \\ &= (3.56 \cdot 10^{-5})(0.01)(5.6704 \cdot 10^{-8})(0.6(473.15)^4 - 0.6(419.15)^4) \\ &= 2.33 \cdot 10^{-4} \text{ W} \end{aligned}$$

$$\begin{aligned} \delta \dot{Q}_{12} &= \sqrt{\left(\frac{d\dot{Q}_{12}}{dA_1}\right)^2 \delta A_1^2 + \left(\frac{d\dot{Q}_{12}}{dT_1}\right)^2 \delta T_1^2 + \left(\frac{d\dot{Q}_{12}}{dT_2}\right)^2 \delta T_2^2} \\ &= \sqrt{(F_{12} \sigma_B (\varepsilon_1 T_1^4 - \varepsilon_2 T_2^4))^2 \delta A_1^2 + (4\varepsilon_1 A_1 F_{12} \sigma_B T_1^3)^2 \delta T_1^2 + (-4\varepsilon_2 A_1 F_{12} \sigma_B T_2^3)^2 \delta T_2^2} \\ &= \left((0.01(5.6704 \cdot 10^{-8})(0.6(473.15^4) - 0.6(419.15^4)))^2 (1.79 \cdot 10^{-6})^2 \right. \\ &\quad + (4(0.6)(3.56 \cdot 10^{-5})(0.01)(5.6704 \cdot 10^{-8})(473.15^3))^2 (0.2)^2 \\ &\quad \left. + (-4(0.6)(3.56 \cdot 10^{-5})(0.01)(5.6704 \cdot 10^{-8})(419.15^3))^2 (0.2)^2 \right)^{\frac{1}{2}} \\ &= \pm 1.18 \cdot 10^{-5} \text{ W} \end{aligned}$$

This quantity represents a small fraction of the radiation loss within the TEG module and needs to be recalculated for both types of view factors and all remaining areas of the Al_2O_3 and the electrical contact surfaces. The summation of these losses are displayed in Appendix G.

Thermoelectric Property Uncertainty

The following is a collection of sample calculations for all of the thermoelectric properties mentioned in this thesis at the 200 °C data point.

Recall equation (3.25):

$$\alpha = \frac{2V_{oa}}{N \cdot D_a} = \frac{2 \cdot 0.111}{252 \cdot 6} = 1.47 \cdot 10^{-4} \text{ V/K}$$

$$\begin{aligned} \delta\alpha &= \sqrt{\left(\frac{d\alpha}{dV_{oa}}\right)^2 \delta V_{oa}^2 + \left(\frac{d\alpha}{dD_a}\right)^2 \delta D_a^2} = \sqrt{\left(\frac{2}{N \cdot D_a}\right)^2 \delta V_{oa}^2 + \left(\frac{-2 \cdot V_{oa}}{N \cdot D_a^2}\right)^2 \delta D_a^2} \\ &= \sqrt{\left(\frac{2}{252 \cdot 6}\right)^2 (4.83 \cdot 10^{-5})^2 + \left(\frac{-2 \cdot 0.111}{252 \cdot 6^2}\right)^2 (0.46)^2} \\ &= \pm 1.11 \cdot 10^{-5} \text{ V/K} \end{aligned}$$

Recall equation (3.36):

$$\begin{aligned} \rho &= \frac{(V_{ia} - V_{oa} - V_c)A}{NIL} = \frac{(0.308 - 0.111 - 0.007) \cdot (1.569 \cdot 10^{-3})^2}{252 \cdot 0.150 \cdot 1.257 \cdot 10^{-3}} \\ &= 9.828 \cdot 10^{-6} \Omega \cdot m \end{aligned}$$

The quantity V_c is a theoretical value calculated in ANSYS and therefore does not have an associated error. At this data point $V_c = 0.007 \text{ V}$.

$$\begin{aligned} \delta\rho &= \sqrt{\left(\frac{d\rho}{dV_{oa}}\right)^2 \delta V_{oa}^2 + \left(\frac{d\rho}{dV_{ia}}\right)^2 \delta V_{ia}^2 + \left(\frac{d\rho}{dA}\right)^2 \delta A^2 + \left(\frac{d\rho}{dI}\right)^2 \delta I^2 + \left(\frac{d\rho}{dL}\right)^2 \delta L^2} \\ &= \end{aligned}$$

$$\begin{aligned}
& \left(\frac{A^2 \delta_{V_{ia}}^2}{N^2 I^2 L^2} + \frac{A^2 \delta_{V_{oa}}^2}{N^2 I^2 L^2} + \frac{(V_{ia} - V_{oa} - V_c)^2 A^2 \delta_I^2}{N^2 I^4 L^2} \right. \\
& \quad \left. + \frac{(V_{ia} - V_{oa} - V_c)^2 A^2 \delta_L^2}{N^2 I^2 L^4} + \frac{(V_{ia} - V_{oa} - V_c)^2 \delta_A^2}{N^2 I^2 L^2} \right)^{1/2} \\
& = \pm 4.96 \cdot 10^{-7} \Omega \cdot m
\end{aligned}$$

For the thermal loss factor, C_L the sum of the radiative losses ΣQ_{rad} is equal to $6.39 \cdot 10^{-1} \pm 2.02 \cdot 10^{-2}$ W at the 200°C data point.

Recall equation (3.30):

$$C_L = 1 - \frac{(\Sigma \dot{Q}_{Rad}) D_a}{2V_{oa}I(T_a + T_a')} = 1 - \frac{(6.39 \cdot 10^{-1})(6)}{2(0.111)(0.150)(446.15 + 447.15)} = 0.871$$

$$\delta C_L = \sqrt{\left(\frac{dC_L}{d\Sigma \dot{Q}_{Rad}} \right)^2 \delta \Sigma \dot{Q}_{Rad}^2 + \left(\frac{dC_L}{dD_a} \right)^2 \delta D_a^2 + \left(\frac{dC_L}{dV_{oa}} \right)^2 \delta V_{oa}^2 + \left(\frac{dC_L}{dI} \right)^2 \delta I^2 + \left(\frac{dC_L}{dT_a} \right)^2 \delta T_a^2 + \left(\frac{dC_L}{dT_a'} \right)^2 \delta T_a'^2}$$

=

$$\begin{aligned}
& \left(\frac{1}{4} \frac{Da^2 \delta_{\Sigma Q_{rad}}^2}{V_{oa}^2 I^2 (T_a + T_a')^2} + \frac{1}{4} \frac{\Sigma Q_{rad}^2 \delta_{Da}^2}{V_{oa}^2 I^2 (T_a + T_a')^2} \right. \\
& \quad + \frac{1}{4} \frac{\Sigma Q_{rad}^2 Da^2 \delta_{V_{oa}}^2}{V_{oa}^4 I^2 (T_a + T_a')^2} + \frac{1}{4} \frac{\Sigma Q_{rad}^2 Da^2 \delta_I^2}{V_{oa}^2 I^4 (T_a + T_a')^2} \\
& \quad \left. + \frac{1}{4} \frac{\Sigma Q_{rad}^2 Da^2 \delta_{T_a}^2}{V_{oa}^2 I^2 (T_a + T_a')^4} + \frac{1}{4} \frac{\Sigma Q_{rad}^2 Da^2 \delta_{T_a'}^2}{V_{oa}^2 I^2 (T_a + T_a')^4} \right)^{1/2}
\end{aligned}$$

$$= \pm 0.011$$

C_L affects both the thermal conductivity and ZT as shown in the sample calculations below.

Equation (3.29):

$$\kappa = \frac{2V_{oa}IL(T_a + T_a')C_L}{NAD_a^2} = \frac{2(0.111)(0.150)(446.15 + 447.15)(0.871)}{252(2.462 \cdot 10^{-6})(6^2)}$$

$$= 1.46 \text{ W/m} \cdot \text{K}$$

$$\delta\kappa = \sqrt{\left(\frac{d\kappa}{dV_{oa}}\right)^2 \delta V_{oa}^2 + \left(\frac{d\kappa}{dI}\right)^2 \delta I^2 + \left(\frac{d\kappa}{dL}\right)^2 \delta L^2 + \left(\frac{d\kappa}{dT_a}\right)^2 \delta T_a^2 + \left(\frac{d\kappa}{dT_a'}\right)^2 \delta T_a'^2 + \left(\frac{d\kappa}{dC_L}\right)^2 \delta C_L^2 + \left(\frac{d\kappa}{dA}\right)^2 \delta A^2 + \left(\frac{d\kappa}{dD_a}\right)^2 \delta D_a^2}$$

=

$$\left(\frac{4J^2L^2(T_a + T_a')^2C_L^2\delta_{V_{oa}}^2}{N^2A^2Da^4} + \frac{4V_{oa}^2L^2(T_a + T_a')^2C_L^2\delta_J^2}{N^2A^2Da^4} + \frac{4V_{oa}^2J^2(T_a + T_a')^2C_L^2\delta_L^2}{N^2A^2Da^4} + \frac{4V_{oa}^2J^2L^2C_L^2\delta_{T_a}^2}{N^2A^2Da^4} + \frac{4V_{oa}^2J^2L^2C_L^2\delta_{T_a'}^2}{N^2A^2Da^4} + \frac{4V_{oa}^2J^2L^2(T_a + T_a')^2\delta_{C_L}^2}{N^2A^2Da^4} + \frac{4V_{oa}^2J^2L^2(T_a + T_a')^2C_L^2\delta_A^2}{N^2A^4Da^4} + \frac{16V_{oa}^2J^2L^2(T_a + T_a')^2C_L^2\delta_{Da}^2}{N^2A^2Da^6} \right)^{\frac{1}{2}}$$

$$= \pm 0.25 \text{ W/m} \cdot \text{K}$$

Equation (3.37):

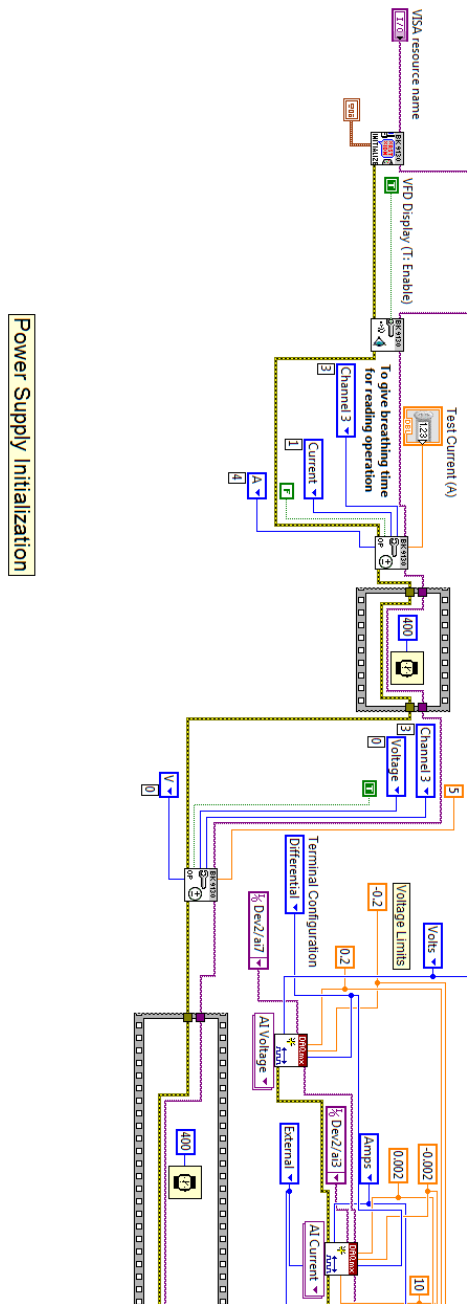
$$ZT = \frac{V_{oa}}{C_L(V_{ia} - V_{oa} - V_c)} = \frac{0.111}{0.871(0.308 - 0.111 - 0.007)} = 0.67$$

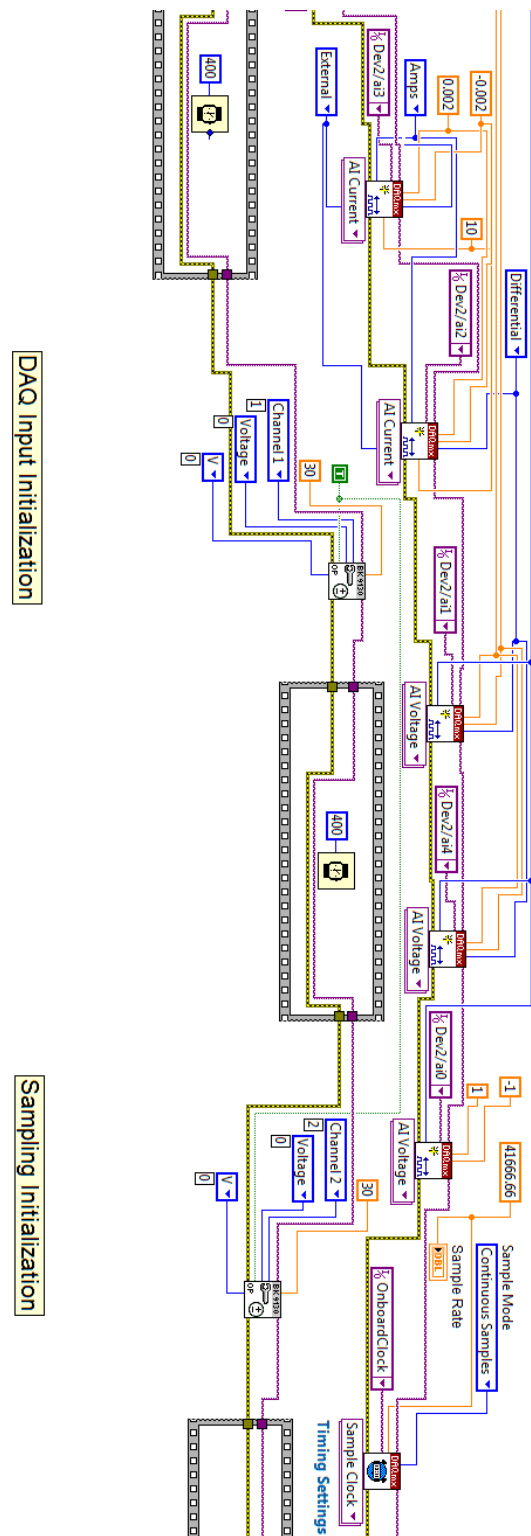
$$\delta ZT = \sqrt{\left(\frac{dZT}{dV_{oa}}\right)^2 \delta V_{oa}^2 + \left(\frac{dZT}{dV_{ia}}\right)^2 \delta V_{ia}^2 + \left(\frac{dZT}{dC_L}\right)^2 \delta C_L^2}$$

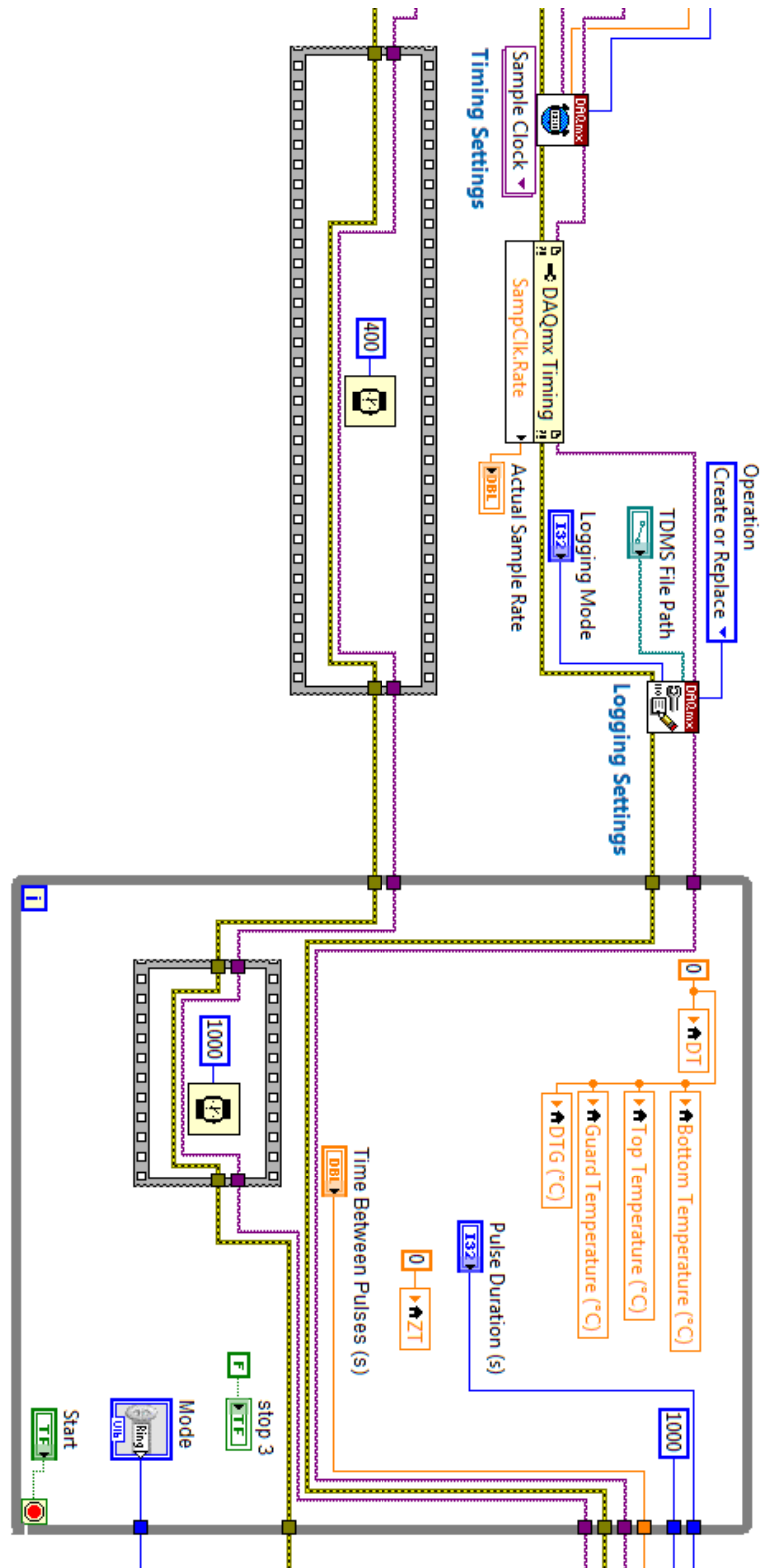
$$= \left(\left(\frac{1}{C_L(V_{ia} - V_{oa} - V_c)} + \frac{V_{oa}}{C_L(V_{ia} - V_{oa} - V_c)^2} \right)^2 \delta_{V_{oa}}^2 + \frac{V_{oa}^2 \delta_{V_{ia}}^2}{C_L^2(V_{ia} - V_{oa} - V_c)^4} + \frac{V_{oa}^2 \delta_{C_L}^2}{C_L^4(V_{ia} - V_{oa} - V_c)^2} \right)^{1/2}$$

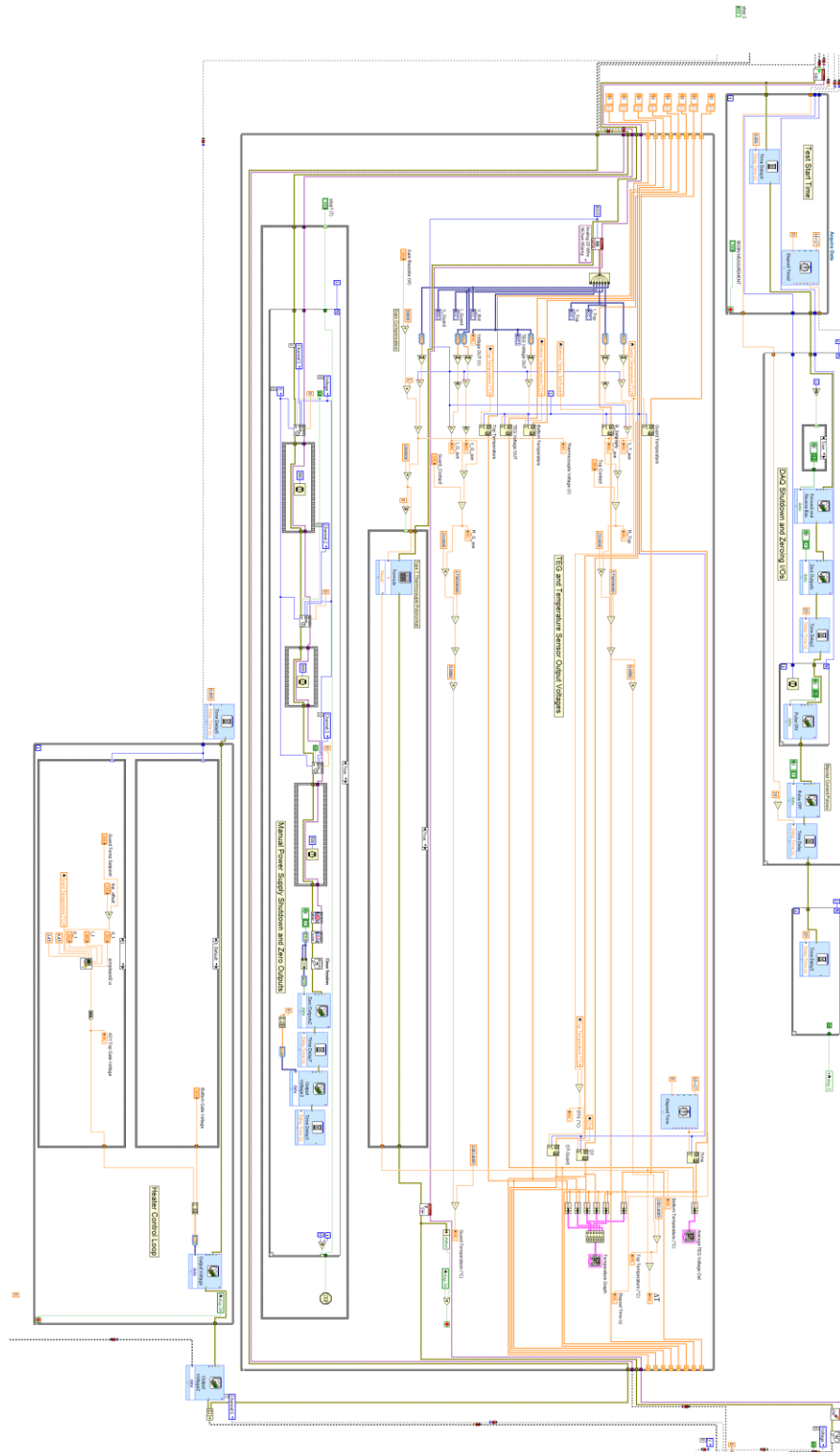
$$= \pm 0.01$$

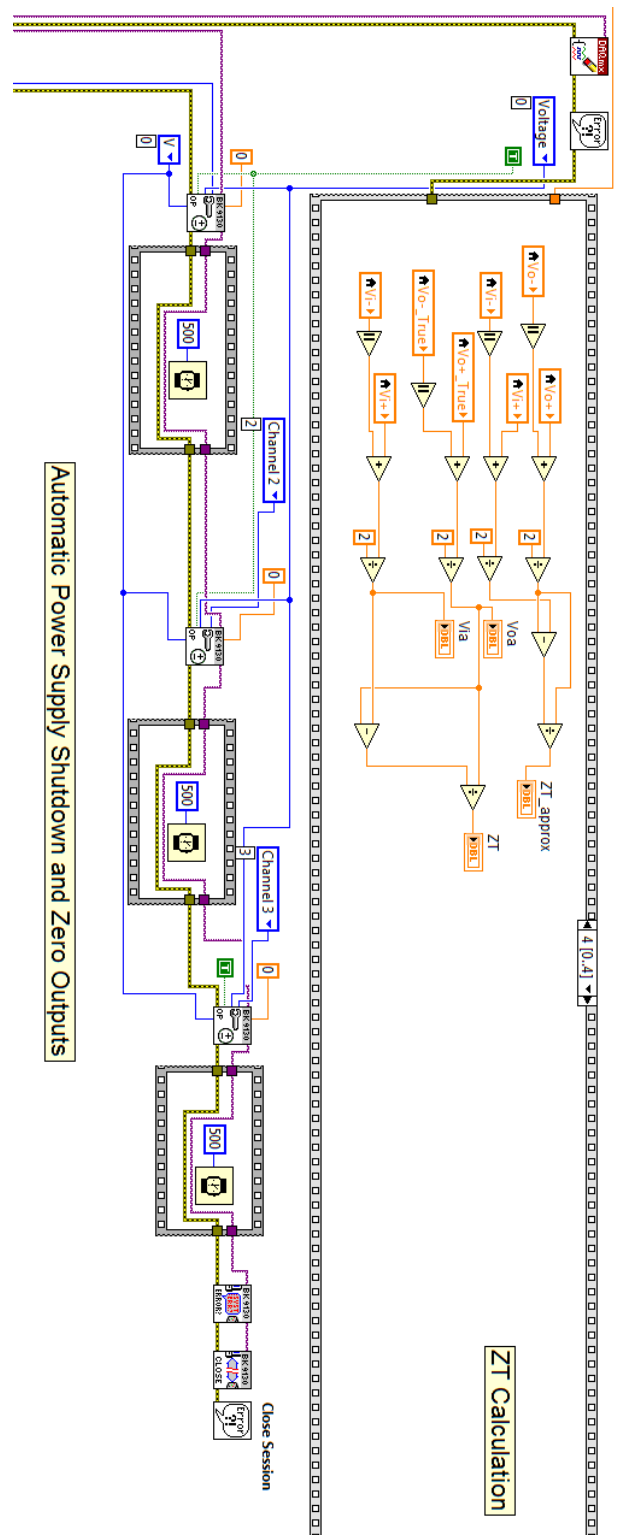
APPENDIX B: Harman Technique LabView Code

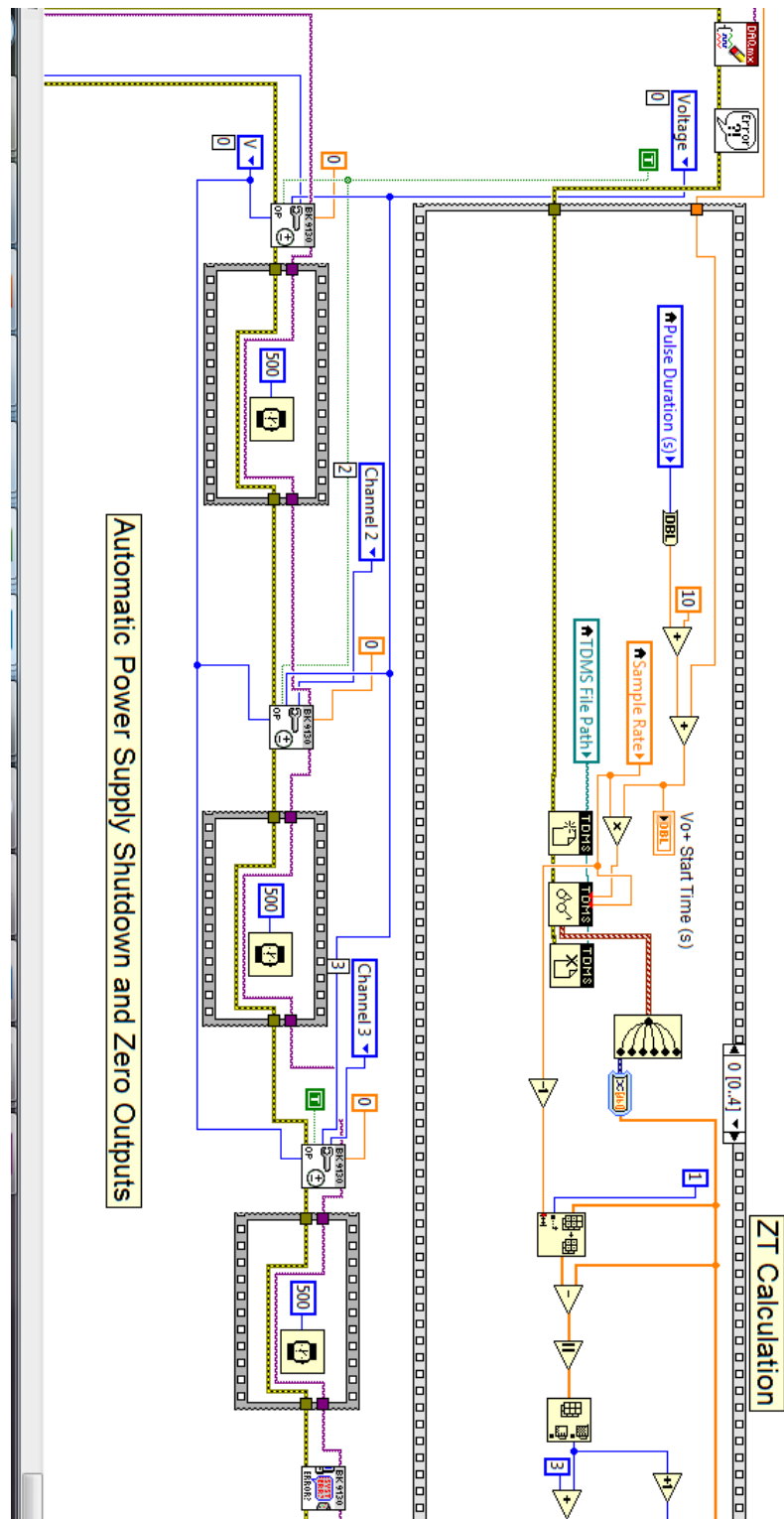


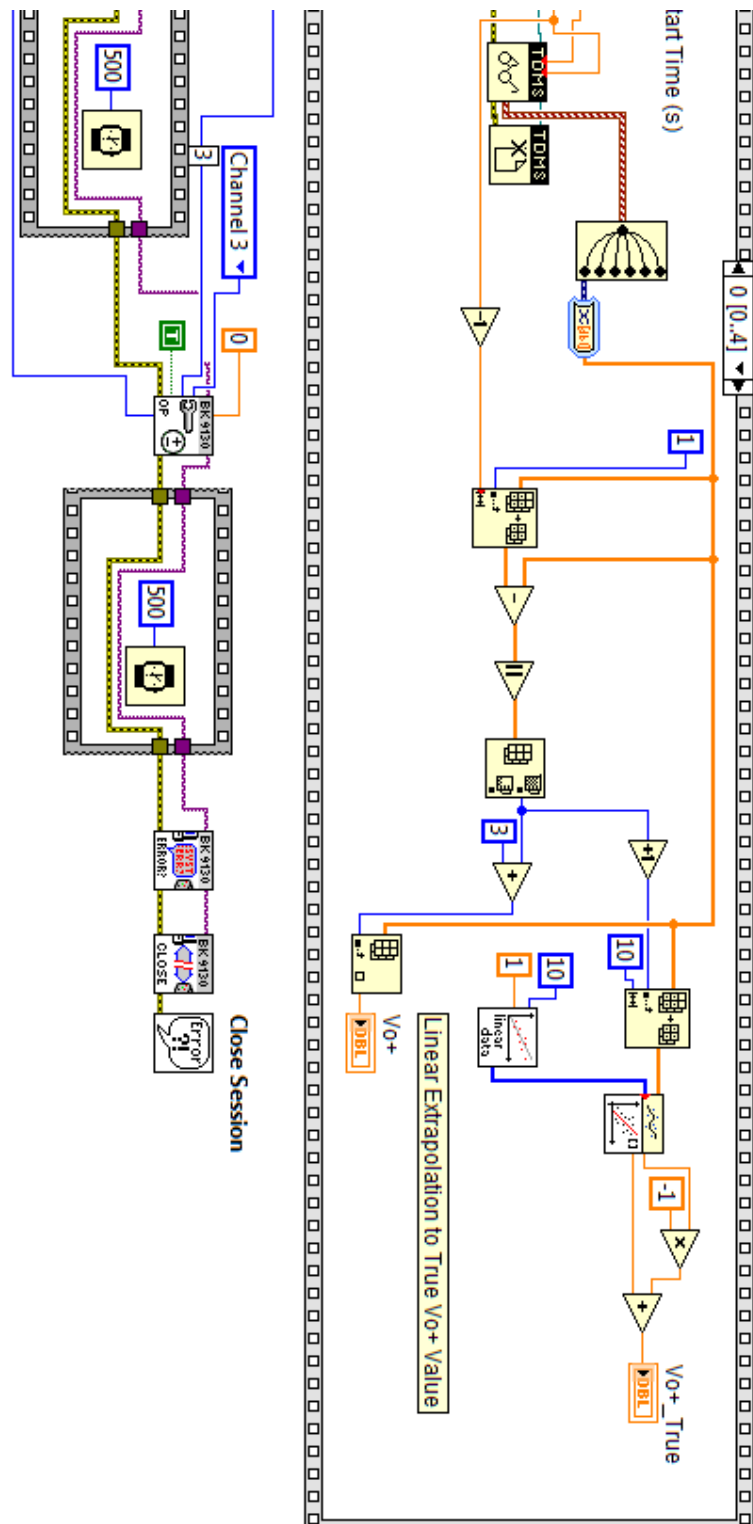




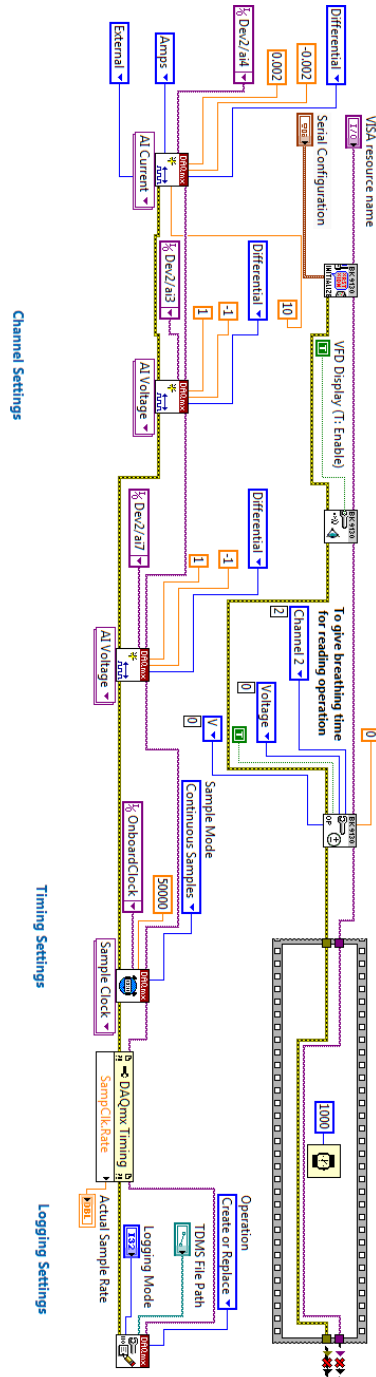


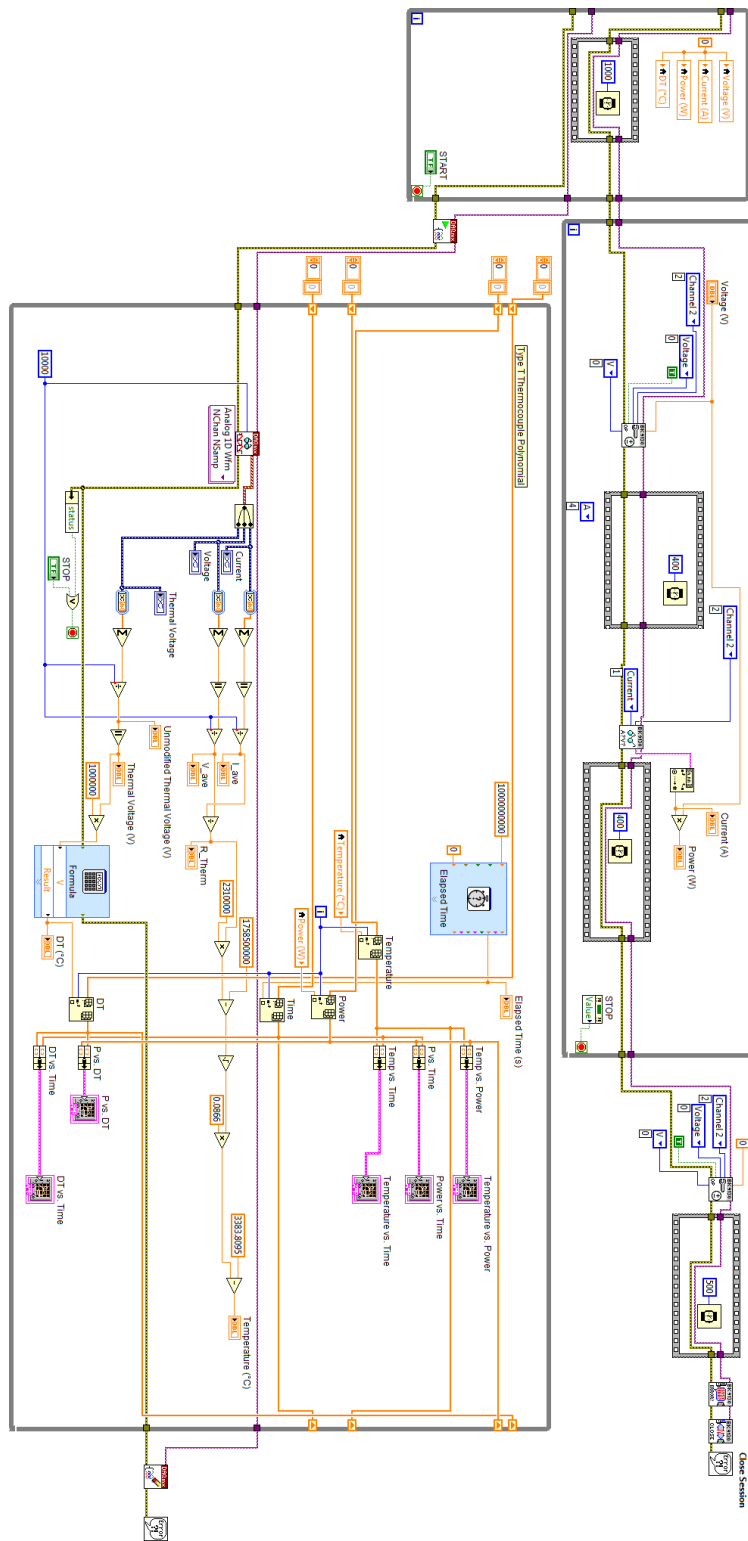






APPENDIX C: PTC Technique LabView Code





APPENDIX E: Heater Material Data

<i>Thermal Conductivity at Various Temperatures [W/m·K]</i>				
Component	300K	400K	600K	800K
NiChrome Wire [33]	12	14	16	21
Copper Plate [33]	401	393	379	366
MgO Substrate [34], [35]	62.5*	33.0	19.2	12.5
OMEGABond 600 Cement [36]	1.59	1.59	1.59	1.59

*Reference [34] provided a range of 50-75 W/m·K for the thermal conductivity of MgO at 300K, so the average value between these two limits was used.

<i>Electrical Resistivity of NiChrome at Various Temperatures [$\Omega\cdot m$]</i>				
Component	300K	400K	600K	800K
NiChrome Wire	$1.00\cdot 10^{-6}$	$1.04\cdot 10^{-6}$	$1.12\cdot 10^{-6}$	$1.20\cdot 10^{-6}$
$\rho_0 = 100\cdot 10^{-8}\Omega\cdot m$ $T_0 = 293.15K$ $\lambda = 4\cdot 10^{-4}K^{-1}$ [29]				

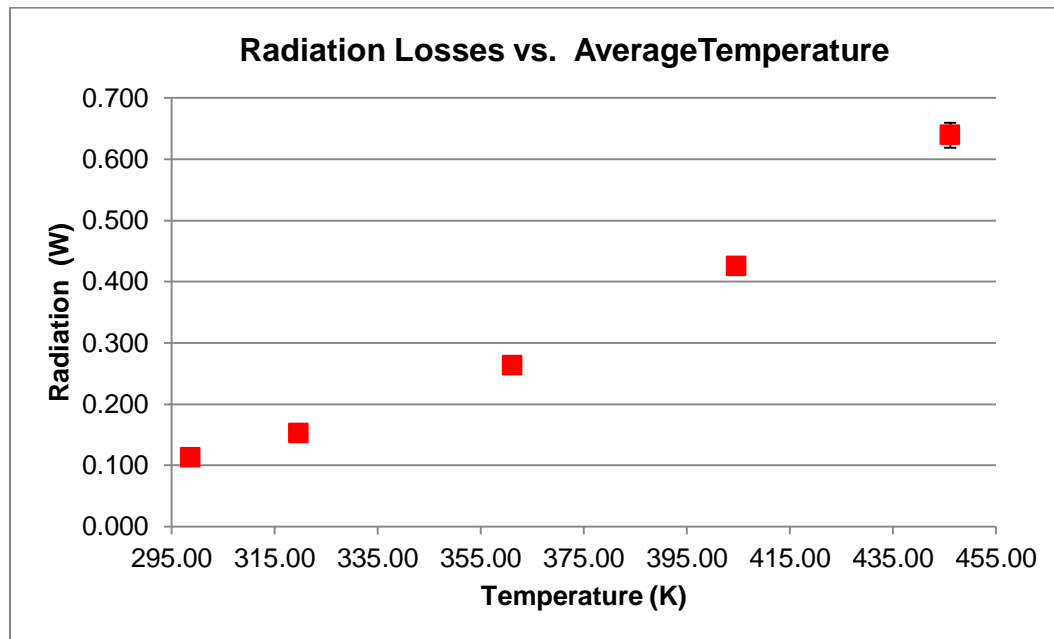
APPENDIX F: Heater Boundary Conditions for ANSYS Simulation

Boundary Condition	Affected Body	Value
<i>Input Current</i>		0.45 A
<i>Ground</i>	NiChrome Wire	0 V
<i>Radiation</i>		$\varepsilon = 0.88$ [37]
<i>Radiation</i>	Copper	$\varepsilon = 0.05$ [38]
<i>Radiation</i>	MgO	$\varepsilon = 0.69$ [38]
<i>Radiation</i>	OMEGABond Cement	$\varepsilon = 0.88$ (Concrete) [38]
<i>Convection</i>	All Bodies	$h = 25 \text{ W/m}^2\cdot^\circ\text{C}$ [38]

*Heat flux calculated by dividing power dissipated through the wire by the surface area of the wire. This surface area was calculated in ANSYS to be 311.63mm^2 .

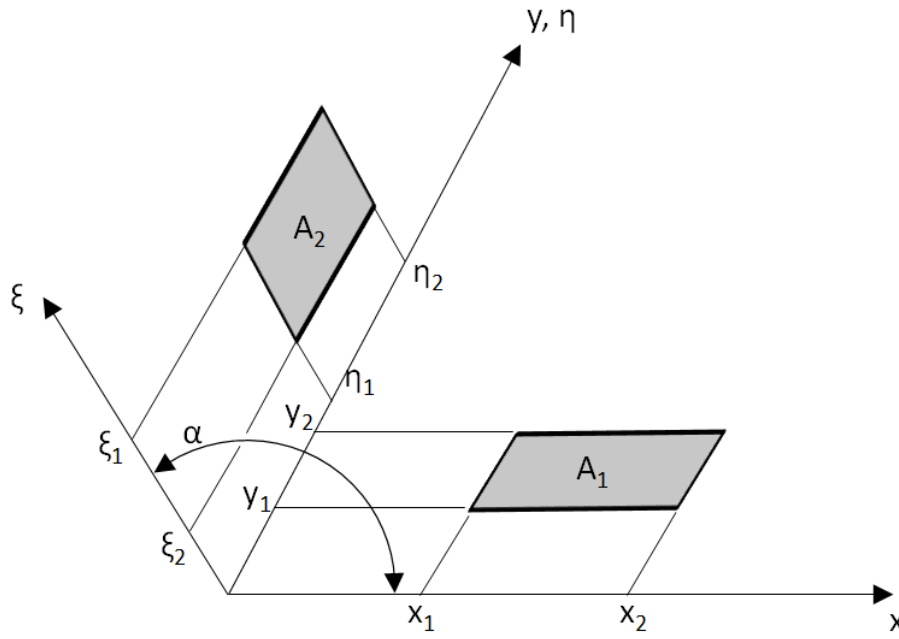
APPENDIX G: Thermal Loss Quantities

The contributions from the radiation losses in each layer of the TEG1B-12610-5.1 are summed at each test point and provided below as a function of average temperature.



APPENDIX H: Sample View Factor Calculations

The two view factors used for the TEG radiation calculations are given below. The dimensions in Appendix I are used to define the coordinates in each of the view factor systems presented, and are used in a sample calculation for two faces.



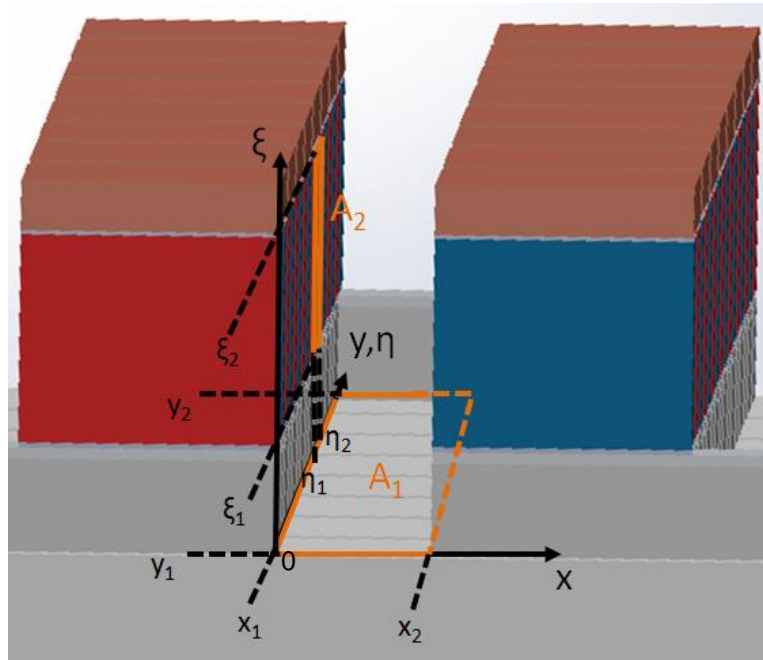
View factor (1) for rectangles in perpendicular planes [25].

Governing Equation for (1):

$$F_{1-2} = \frac{1}{A_1} \sum_{i=1}^2 \sum_{j=1}^2 \sum_{k=1}^2 \left[(-1)^{(i+j+k+l)} G(x_i, y_j, \eta_k, \xi_l) \right]$$

where

$$G = -\frac{(\eta - y) \sin^2 \alpha}{2\pi} \int_{\xi} \left(\frac{(x - \xi \cos \alpha) \cos \alpha - \xi \sin^2 \alpha}{(x^2 - 2x\xi \cos \alpha + \xi^2)^{1/2} \sin^2 \alpha} \tan^{-1} \left[\frac{\eta - y}{(x^2 - 2x\xi \cos \alpha + \xi^2)^{1/2}} \right] \right. \\ \left. + \frac{\cos \alpha}{(\eta - y) \sin^2 \alpha} \left\{ \left[\xi^2 \sin^2 \alpha + (\eta - y)^2 \right]^{1/2} \tan^{-1} \frac{x - \xi \cos \alpha}{\left[\xi^2 \sin^2 \alpha + (\eta - y)^2 \right]^{1/2}} - \xi \sin \alpha \tan^{-1} \left(\frac{x - \xi \cos \alpha}{\sin \alpha} \right) \right\} \right. \\ \left. + \frac{\xi}{2(\eta - y)} \ln \left[\frac{x^2 - 2x\xi \cos \alpha + \xi^2 + (\eta - y)^2}{x^2 - 2x\xi \cos \alpha + \xi^2} \right] \right) d\xi$$



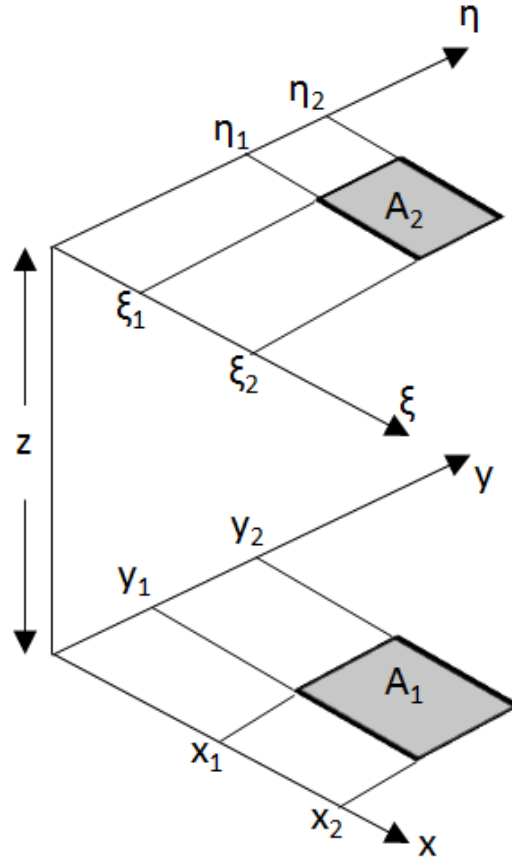
View factor (1) for Al_2O_3 portion to single Bi_2Te_3 face within TEG module.

Coordinate	Related Dimensions	Value (mm)
x_1	0	0
x_2	(element spacing)	0.935
y_1	0	0
y_2^*	$0.5(\text{element spacing}) + 15 * (\text{n-type horizontal width}) + 15 * (\text{element spacing})$	38.028
ξ_1	$(\text{Zn vertical length}) + (\text{Al vertical length}) + (\text{Ni}_b \text{ vertical length})$	0.66

ξ_2	(Zn vertical length) + (Al vertical length) + (Ni _p vertical length) + (n-type vertical length)	1.917
η_1^*	0.5*(element spacing) + 9*(n-type horizontal width) + 9*(element spacing)	22.069
η_2^*	0.5*(element spacing) + 9*(n-type horizontal width) + 9*(element spacing) + (n-type horizontal width)	23.6375
$F_{12} = 0.01$		

**The Al₂O₃ substrate layer began a distance of 0.5*(element spacing) before the beginning of the contacts and TEG elements and this distance is accounted for in the above calculations.*

View factor (1) sample calculation for two rectangles in perpendicular planes.

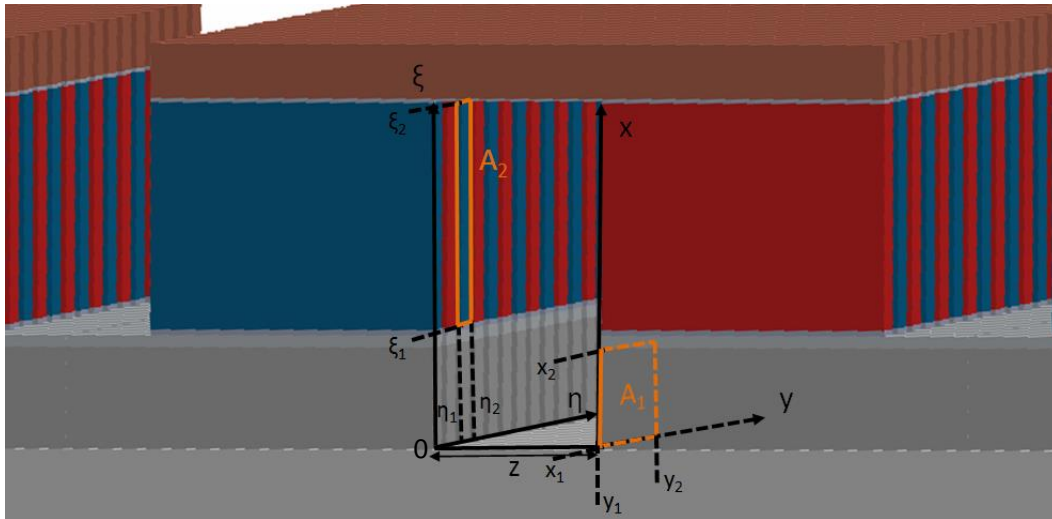


View factor (2) for two surfaces in parallel planes [25]

Governing Equation for (2)

$$F_{1-2} = \frac{1}{(x_2 - x_1)(y_2 - y_1)} \sum_{l=1}^2 \sum_{k=1}^2 \sum_{j=1}^2 \sum_{i=1}^2 (-1)^{(i+j+k+l)} G(x_i, y_j, \eta_k, \xi_l)$$

$$G = \frac{1}{2\pi} \left(\begin{aligned} & (y - \eta) \left[(x - \xi)^2 + z^2 \right]^{1/2} \tan^{-1} \left\{ \frac{y - \eta}{\left[(x - \xi)^2 + z^2 \right]^{1/2}} \right\} \\ & + (x - \xi) \left[(y - \eta)^2 + z^2 \right]^{1/2} \tan^{-1} \left\{ \frac{x - \xi}{\left[(y - \eta)^2 + z^2 \right]^{1/2}} \right\} \\ & - \frac{z^2}{2} \ln \left[(x - \xi)^2 + (y - \eta)^2 + z^2 \right] \end{aligned} \right)$$



View factor (2) for Zn face to single Bi_2Te_3 face within TEG module.

Coordinate	Related Dimensions	Value (mm)
x_1	0	0
x_2	(Zn vertical length)	0.563
y_1	0	0
y_2	(n-type horizontal width)	1.569
ξ_1	(Zn vertical length) + (Al vertical length) + (Ni_b vertical length)	0.66
ξ_2	(Zn vertical length) + (Al vertical length) + (Ni_b vertical length) + (n-type vertical length)	1.917

η_1	2*(n-type horizontal width) + 2*(element spacing)	5.008
η_2	2*(n-type horizontal width) + 2*(element spacing) + (n-type horizontal width)	6.577
z	(element spacing)	0.935
$F_{12} = 0.00$		

View factor (2) sample calculation for two rectangles in parallel planes.

The calculations above were cycled through each of the Bi_2Te_3 faces within the row of the module and then summed. This process was repeated over the entire TEG geometry and used to determine the view factor contributions for the remaining elemental layers.

APPENDIX I: TEG Unit Cell Dimensions

Vertical Dimensions (mm)									
Measurement #	n-type	p-type	Ni_B	Al	Zn	Al₂O₃	Cu	Sn	Ni_T
1	1.239	1.251	0.032	0.067	0.566	0.733	0.314	0.015	0.010
2	1.245	1.288	0.031	0.060	0.571	0.737	0.310	0.017	0.011
3	1.248	1.294	0.036	0.055	0.555	0.723	0.303	0.014	0.010
4	1.253	1.276	0.023	0.071	0.609	0.720	0.296	0.006	0.009
5	1.243	1.274	0.035	0.081	0.565	0.715	0.302	0.015	0.012
6	1.239	1.250	0.033	0.070	0.523	0.712	0.296	0.014	0.010
7	1.248	1.257	0.028	0.067	0.536	0.705	0.291	0.011	0.011
8	1.247	1.266	0.025	0.076	0.557	0.719	0.299	0.014	0.007
9	1.241	1.257	0.034	0.080	0.553	0.739	0.298	0.011	0.008
10	1.255	1.274	0.022	0.047	0.592	0.745	0.305	0.010	0.007
Average Value:	1.257		0.030	0.067	0.563	0.725	0.301	0.013	0.010
Uncertainty	± 0.016		±0.005	±0.011	±0.025	±0.013	±0.007	±0.003	±0.002

Horizontal Dimensions (mm)			
Measurement #	p-type	n-type	Element Spacing
1	1.582	1.566	0.893
2	1.575	1.548	0.911
3	1.569	1.541	0.888
4	1.573	1.524	0.915
5	1.586	1.545	0.929
6	1.590	1.551	0.930
7	1.590	1.556	0.953
8	1.589	1.540	0.965
9	1.618	1.538	0.980
10	1.633	1.567	0.983
Average Value:	1.569		0.935
Uncertainty	±0.028		±0.034

APPENDIX J: TEG Unit Cell Material Data

Thermal Conductivity and Electrical Resistivity of TEG Layer Materials

Temperature (K)	Copper		Aluminum		Aluminum Oxide	Nickel	
	ρ ($\Omega \cdot m$)	κ (W/m·K)	ρ ($\Omega \cdot m$)	κ (W/m·K)	κ (W/m·K)	ρ ($\Omega \cdot m$)	κ (W/m·K)
250	-	406	-	235	-	-	97.5
293.15	$1.68 \cdot 10^{-08}$	-	$2.65 \cdot 10^{-08}$	-	39	$6.93 \cdot 10^{-08}$	-
300	$1.76 \cdot 10^{-08}$	401	$2.73 \cdot 10^{-08}$	237	36	$7.20 \cdot 10^{-08}$	90.7
400	$2.90 \cdot 10^{-08}$	393	$3.86 \cdot 10^{-08}$	240	26.4	$1.18 \cdot 10^{-07}$	80.2
600	$5.19 \cdot 10^{-08}$	379	$6.14 \cdot 10^{-08}$	231	15.8	$2.55 \cdot 10^{-07}$	65.6
800	$7.47 \cdot 10^{-08}$	366	$8.41 \cdot 10^{-08}$	218	10.4	$3.55 \cdot 10^{-07}$	67.6
Reference:	[29]	[5], [38]	[29]	[5], [38]	[5], [38]	[39]	[5], [38]

Temperature (K)	Tin	
	ρ ($\Omega \cdot m$)	κ (W/m·K)
250	-	69.6
273.15	$1.15 \cdot 10^{-07}$	-
373.15	$1.55 \cdot 10^{-07}$	60.7
473.15	$2.00 \cdot 10^{-07}$	56.5
Reference:	[40]	[39]

Temperature (K)	Zinc	
	ρ ($\Omega \cdot m$)	κ (W/m·K)
200	$3.83 \cdot 10^{-08}$	118
300	$6.06 \cdot 10^{-08}$	116
400	$8.37 \cdot 10^{-08}$	111
600	$1.35 \cdot 10^{-07}$	103
Reference:	[39]	[38]

Emissivity of TEG Layer Materials

ϵ -Cu	ϵ -Al	ϵ -Ni	ϵ -Sn	ϵ -Zn	ϵ -Al ₂ O ₃	ϵ -Bi ₂ Te ₃
0.6	0.25	0.45	0.05	0.25	0.7	0.6
Reference:				[38]		